



Superconducting correlations in single and multilayer graphene

Supergeleidende correlaties in enkel-en meerlaagse grafeen

Proefschrift ingediend tot het behalen van de graad van
Doctor in de Wetenschappen
aan de Universiteit Antwerpen, te verdedigen door

William Armando MUÑOZ

Promotor

Prof. dr. François M. Peeters

Co-promoter

Dr. Lucian Covaci

Antwerpen, 2014

Members of the Jury:

Chairman

Prof. dr. Nick Schryves, University of Antwerp, Belgium

Promotors

Prof. dr. François. M. Peeters, Universiteit Antwerpen, Belgium

Dr. Lucian Covaci, Universiteit Antwerpen, Belgium

Members

Prof. dr. Dirk Lamoen, Universiteit Antwerpen, Belgium

Prof. dr. Michael Wouters, Universiteit Antwerpen, Belgium

Prof. dr. Joseph Indekeu, Katholieke Universiteit Leuven, Belgium

Prof. dr. Tatiana Rappoport , Universidade Federal do Rio de Janeiro, Brazil

Contact Information

William Armando Muñoz
G.U. 209
Groenenborgerlaan 171
2020 Antwerpen
België
wallaz85@gmail.com

*Dedicated to the loving memory of my
grandma Adela*

Acknowledgement

First and foremost I wish to express my sincere gratitude to Prof. dr. François Peeters for giving me the great opportunity of being part of his group. I am thankful for your encouragement, constructive criticism and corrections, but particularly for your patience and continues support along these years.

My deep thanks go to Dr. Lucian Covaci for the uncountable and fruitful advises during the whole process, and for the patient and detailed review in the preparation of the manuscripts and the thesis. I am extremely grateful for your thoughtful guidance, the insightful discussions, and particularly for your friendly support even during the hard times.

I would like to thank the members of the jury for all their valuable suggestions and helpful comments to improve the quality of the final version of the thesis. I must thank also to Ben and Mario for translating the summary of my thesis in Flemish.

I am very grateful to Hilde, our secretary, for handling the paperwork with such an incredible efficiency. I also thank Nikolas for helping me every time that something went wrong with the GPU nodes.

I also would like to thank to my colleagues at the CMT and EMAT group for their friendship. Particularly to my office mates: Hamilton, Lucia, Ben, Maluco and Hasan whom during all this time made our workplace a very friendly environment. Thanks also to all the guys of the midday Tuesday's football. Surely, I will miss that pretty much, despite of all the defeats in the university championship.

I am indebted to all my friends who have supported me over the last years: Hamilton, Ricardo, Eduardo, Evelyn, Victor, Maluco, Silvia, Sebastian, Paulo, Diego, Adorno, Belisa (...). Thank you guys for the fun that we had and all the nice moments that we shared together. To my dear flatmates and close friends Hamilton, Ricardo and Victor, thanks for all the good memories of our time at the G199.

I warmly thank my family in Colombia whom in spite of the distance kept supporting me along these years that I have been away from home.

Last, but by not means least, I own a very special thank to my lovely wife

Evelyn. Your support, encouragement and kindness have been invaluable on both academic and personal level, for which I am extremely grateful. These last lines, and the rest of my life as well, are reserved for you my dear.

This work was supported by the Flemish Science Foundation (FWO-VI) and the Methusalem funding of the Flemish Government.

Table of Contents

1	Introduction	1
1.1	The marvelous graphene flatland	1
1.2	Superconductivity in carbon structures	2
1.3	Graphene becomes a superconductor: Proximity effect	6
1.4	Motivation of this thesis	9
1.5	Outline of this thesis	10
2	Theoretical framework and numerical methods	11
2.1	Graphene basics	11
2.1.1	Crystal lattice structure	11
2.1.2	From tight-binding to Dirac equation	14
2.1.3	Bilayer graphene	14
2.1.4	Multilayer graphene	17
2.2	Superconductivity basics	19
2.2.1	BCS theory	19
2.2.2	Inhomogenous superconductivity: The Bogoliubov de Gennes equations	22
2.3	The Chebyshev-Bogoliubov-de Gennes method	24
2.3.1	Basic properties of Chebyshev polynomials	26
2.3.2	Expansion of the Gor'kov-Green functions	27
2.3.3	Implementation details	29
2.3.4	Complex absorbing potential	31
2.4	GPU computing	35
3	Tight-binding study of bilayer graphene Josephson junctions	37
3.1	Introduction	37
3.2	Model System	38
3.3	Numerical Method: Chebyshev expansion of the Green's function	40
3.4	Results	42

3.4.1	Proximity effect	43
3.4.2	LDOS	43
3.4.3	Josephson current	45
3.4.3.1	Unbiased case	45
3.4.3.2	Biased case	48
3.5	Conclusions	50
4	Tight-binding description of intrinsic superconducting correlations in multilayer graphene	51
4.1	Introduction	52
4.2	Model and calculation approach	53
4.3	Numerical results	54
4.4	Conclusions	63
5	Superconducting current and proximity effect in ABA and ABC multilayer graphene Josephson junctions	65
5.1	Introduction	66
5.2	Model System	69
5.3	Conclusions	74
6	Disordered graphene Josephson junctions	75
6.1	Introduction	75
6.2	Model	78
6.3	Results	80
6.3.1	Vacancies	80
6.3.2	Ripples: Gaussian bumps	82
6.3.3	Charged impurities	86
6.4	Conclusion	90
7	Summary	93
7.1	Concluding remarks of the thesis	93
7.2	Future prospects	95
8	Samenvatting	97
8.1	Overzicht van de thesis	97
	Bibliography	101

1

Introduction

1.1 The marvelous graphene flatland

In 2004 a new fascinating playground for condensed matter physics came up when Kostya Novoselov and Andre Geim from Manchester University reported the observation of an isolated two-dimensional structure of carbon atoms obtained in one of their “Friday experiments” [1]. Regarded as a virtual material for decades, this promising material was predicted more than fifty years ago to exhibit an unique electronic band structure with carriers at low energies obeying a linear dispersion instead of the conventional quadratic one found for Schrödinger particles [2]. In fact, the low-energy Hamiltonian for electrons in this structure was shown to map onto a relativistic Dirac equation for massless fermions [3]. In spite of this remarkable fact, earlier experiments of this carbon two-dimensional structure failed to observed traces of its unusual electronic properties and hence most of earlier experimental realizations fell into oblivion. Looking back in time, oldest observations of this single-atom thick structure date back to 1859 with the first oxide samples floating in a suspension obtained by Benjamin Brodie [4]. Unaware of the importance of his discovery, Brodie’s observation remained hidden for almost one century till Hans-Peter Boehm identified some not isolated monolayer graphite samples for the first time and called them *graphene* [5]. Other experimental studies of graphene grown on insulating substrates [6] and metals [7] appeared unnoticed before 2004 and further discoveries may also have passed unperceived unless distinguishing electronic properties of graphene were

unveiled in the samples obtained by Geim and co-workers [8]. Using the mechanical cleavage method to obtain samples by peeling graphite with a Scotch tape (see Fig. 1.1(a)), Geim and co-workers succeeded to reveal an anomalous quantum Hall effect from those samples identified to be one-atom thick in an optical microscope (see Fig. 1.1(b)). This unconventional Hall effect with half-integer plateaux (see Fig. 1.1(c)) was probably the most striking demonstration of the relativistic nature of carriers therein [8]. An avenue of active theoretical and experimental research followed Geim and co-workers novel discovery [9, 10]. Just to name some of them: unconventional properties of Dirac fermions in graphene, like the transparent transmission through high and wide potential barriers named Klein tunneling; a half-integer quantum Hall effect followed by an anomalous integer quantum Hall effect reported for bilayer graphene samples (see inset in Fig. 1.1(c)); the absence of weak localization or the appearance of large pseudo-magnetic fields owing to mesoscopic ripples among others has been experimentally verified [8, 11–15].

Graphene has also risen as a promising material for technological purposes since it is inert against oxidation in ambient environment and its carrier density is tunable under the electric field effect. In addition, graphene samples have shown to support a high mobility of carriers of $2.42 \times 10^4 \text{cm/Vs}$ [10], which is several orders of magnitude larger than the one measured in copper. Even if the lack of confinement due to Klein tunneling of carriers is an obstacle to develop graphene-based transistors, bilayer graphene offers an alternative for a field-effect transistor based on graphene. Hence, while single layer graphene is gapless, it is possible to induce a gap in bilayer graphene which is tunable by a bias voltage applied between both layers [16]. These peculiarities open a wide scenario for technological applications of graphene devices like transistors that operated at high-frequencies and more efficient quantum interferometers. Finally, Andre Geim and Kostya Novoselov were awarded in 2010 with the Nobel Prize in physics for their groundbreaking experiments.

1.2 Superconductivity in carbon structures

Although graphene exhibits many fascinating properties, intrinsic superconductivity has been not observed among them. Unfortunately not only graphene but most of the carbon allotropes in their pure form are found not to sustain superconductivity by themselves, with few exceptions like ropes of single-walled carbon nanotubes where hints of superconductivity have been reported [18, 19]. Nonetheless, a wide number of indications pointing to superconductivity in others compounds containing carbon as a fundamental component have been observed since 1965 [20]. In spite of the low critical temperature found for the

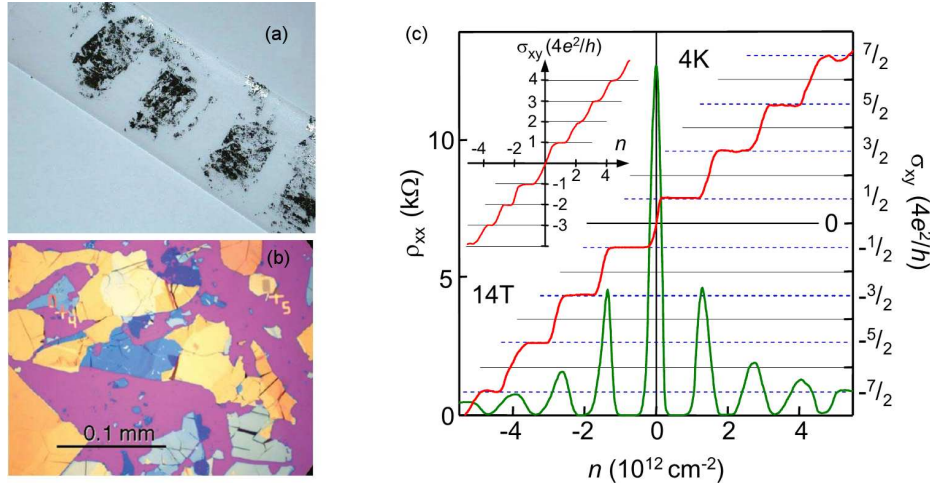


Figure 1.1: Mechanical exfoliation method as used by Geim and co-workers: (a) Remnants of graphite after peeling a sample of highly ordered pyrolytic graphite with Scotch tape. (b) Once some of peeled graphite samples are placed on top of silicon oxide wafer, different thickness can be distinguished by means of optical contrast where some optically transparent fragments were identified having one-atom thick. (c) The resistivity and the Hall conductivity as a function of charge-carrier concentration measured in single-layer graphene samples. Half-integer filling factors found in conductivity is an unambiguous evidence of the two-dimensional nature of the graphene samples and their linear energy spectrum. The inset shown the integer conductivity and with the anomalous step at the neutrality point measured in samples of bilayer graphene. Adapted from Ref. [17] and [8]

superconducting transition of these materials, usually lower than 1K, interest for superconducting phases in carbon-based structures has been renewed every time that a new form of carbon is discovered, without success in most of the cases, but with some remarkable progress like the discovery of relatively high T_c superconductivity for graphite intercalated compounds (GICs). In addition, the discovery of the superconductor magnesium diboride with $T_c=39\text{K}$ in 2001 [21], put in perspective the potential appearance of superconductivity for graphite layered structures due to the crystallographic and electronic analogy. In fact, intercalant atoms are claimed to induce superconductivity between graphite layers below a critical temperature, T_c , around 11K [22, 23]. Among GICs other carbon-based structures like Boron-doped diamond [24] and alkali-doped fullerenes [25] were also reported to superconduct. Different studies have suggested that electron-phonon mediated pairing is the most likely mechanism responsible for superconductivity in these structures [26, 27]. However, it is not clear whether the intercalant

atom vibrations [27] or the graphene-derived phonons [28] play the dominant role here. For instance, former case results in analogy with intercalated manganese diboride where high-frequency vibrations of boron atoms, which conform a hexagonal lattice similar to carbon in graphene, are believed to be the responsible for the electron-phonon coupling [29]. Despite of the many studies about superconductivity in graphite, this is still not fully understood.

In turn to graphene, the occurrence of phonon-mediated superconductivity was predicted to emerge by the same mechanism responsible for superconductivity in GICs when doped with lithium [30, 31]. While calcium is expected to induce phonon-mediated superconductivity in graphene, according to recent observations performed by angle-resolved photoemission spectroscopy [32], more progress has to be made in order to consider graphene as an inherent superconductor. In spite of that, theoretical descriptions concerning to superconductivity in graphene have been triggered by the experimental observations in graphite compounds. An example of this corresponds to the study of electronic correlations in graphene [33] as a way to elucidate the superconducting behaviour reported in graphite-sulfur composites [34, 35] even .

The experimental isolation of graphene sparked an increasing theoretical interest about the possibility of superconducting states in graphene. For instance, it is known now that superconductivity cannot appear by conventional mechanism in pristine graphene as the density of states (DOS) vanishes at the neutrality point [37, 38]. Furthermore, superconducting transitions are predicted to emerge above a quantum critical point where the pairing potential exceeds a minimum value. Other exotic mechanisms like plasmon-electron coupling, Kohn-Luttinger or electron-electron interactions have been predicted to lead to superconducting

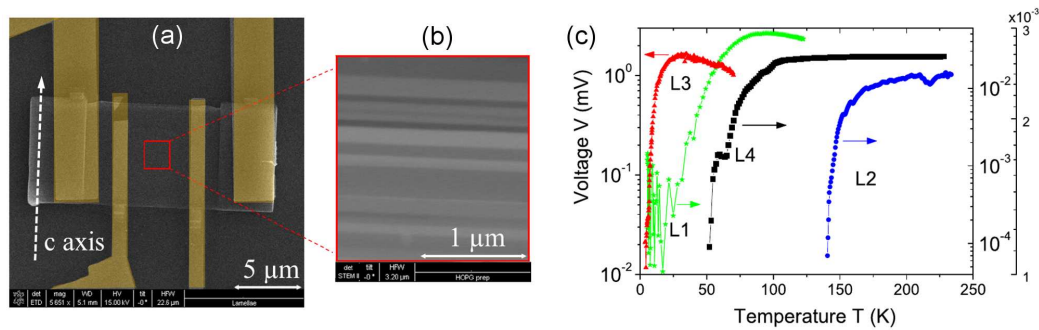


Figure 1.2: (a) Scanning electron microscopy of a HOPG sample on Si/SiN substrate. (b) Transmission electron microscopy image of the cross section of the HOPG sample where brightness corresponds to different orientations between adjacent graphene layers. (c) Drop of the voltage measured for different samples of HOPG. Adapted from Ref. [36]

instabilities in graphene at non-zero density carriers. In these cases, unconventional superconducting states with $p + ip$ [37], f [39, 40] and $d + id$ -wave symmetry [33, 40–45] are expected to emerge. Chiral $d + id$ superconductivity is of particular interest due to its robustness against disorder and dominance over other anisotropic states [46]. In addition, it has been demonstrated that Majorana modes appear in chiral $d + id$ superconducting states in graphene [47]. Despite of these encouraging theoretical predictions, no experimental evidence of chiral superconductivity have been reported yet and multiple challenges are expected to appear in these experiments. For instance, in a heavily doped regime, the dopants may introduce strong charge inhomogeneities or deform the band structure, and therefore conventional phonon-mediated mechanism is expected to induce s-wave superconducting states.

Beyond the lack of superconductivity in graphene, recent experimental reports claim the observation of possible traces of superconducting behavior in high-oriented pyrolytic graphite (HOPG) samples [48]. These graphite samples consist of free-impurities identical graphene layers stacked in a highly ordered configuration. However, the observed superconducting characteristics are likely not related to bulk properties of graphite as the Josephson tunneling effect was detected at some interfaces of the sample, evidencing the existence of granular superconductivity in graphite [36]. Misalignment between adjacent graphite layers was identified to occur at these interfaces (see Fig. 1.2(a)-(b)), and therefore appearance of superconductivity is related to these imperfections since the measured voltage between the electrodes is observed to fall at different temperatures for the samples with different concentrations of internal interfaces (see Fig. 1.2(c)). Since authors dismiss the presence of impurities it is important to realize that the mentioned experimental report pointed out the existence of superconductivity in pristine multilayer graphene structure.

Other signs of superconducting behavior in graphite have been reported so far. For instance, periodic oscillations of the magnetoresistance have been assigned to Andreev scattering between the Josephson-superconducting-grains in HOPG samples. The same authors claim that percolative superconductivity is the cause behind an anomalous hysteresis measured in the HOPG samples [49–51]. Even more intriguing is the indication of granular superconductivity occurring at room-temperature in graphite powder samples after being treated with water [52]. Most recent evidences have suggested the appearance of superconductivity in pure graphite under the application of gate voltages [53]. In spite of all these experimental evidence, among other older observations [54, 55] the existence of superconductivity remains under debate since magnetism could be also present in graphite samples.

1.3 Graphene becomes a superconductor: Proximity effect

Superconductivity can be induced in graphene by proximity effect of small samples in contact with another superconductors material. A similar procedure was previously implemented in carbon nanotubes where supercurrent was observed flowing through the nanotube between two superconductors contacts [56]. Few years after the discovery of graphene, a pioneering work by Morpugo and co-workers succeeded to build the first graphene-based superconducting device owing to the proximity effect. Having obtained single-layer graphene samples through mechanical exfoliation, a superconducting Josephson device was build by depositing through beam lithography techniques, two separate aluminum (Al) electrodes on top of graphene in the configuration shown in Fig. 1.3(a). Desirable electric contacts are ensured by means of a titanium layer placed at the interface between the superconductor and graphene. Ballistic regime can be assumed since the phase coherence length in these graphene samples ($L_\phi > 1\mu\text{m}$) is larger than the separation between Al electrodes, which is in the range of 100-500nm. Thus, when cooling down below the Al critical temperature T_c around 1.3K, superconducting-like properties occur by proximity effect in the graphene regions underneath the superconducting Al contacts. A direct evidence of the occurrence of these superconducting correlations is the observation of the Josephson effect, where electrons and holes are transported coherently through the non-superconducting graphene bridge between the Al electrodes. The mechanism behind this proximity-induced current is the Andreev reflection taking place at the interface between the superconductor and the normal graphene. This Andreev conversion scatter a Cooper pair from the superconductor into an electron-hole pair in the normal metal [57]. Since Cooper pairs are made of electrons with opposite spin and momentum, elastic Andreev scattering injects electrons and hole in opposite K-points (see Fig. 1.3(c)). By doping the graphene junction with electron or holes, Morpugo and co-workers succeeded to measure a bipolar supercurrent, observing no drop of voltage, as it can be seen Fig. 1.3(d), which is a remarkable sign of proximity-induced superconductivity in the graphene samples [58]. Among this observation, a finite supercurrent flowing at zero charge density puts in evidence some of the remarkable superconducting properties of graphene (see Fig. 1.3(b)).

Theoretical models predicting a minimum value for the supercurrent at the Dirac point show the unusual superconducting characteristics of graphene Josephson junctions. One of these characteristics is related to the dependence of the critical current and the universal constant defined by the product between the critical current and the normal resistance on the junction geometry [59]. These char-

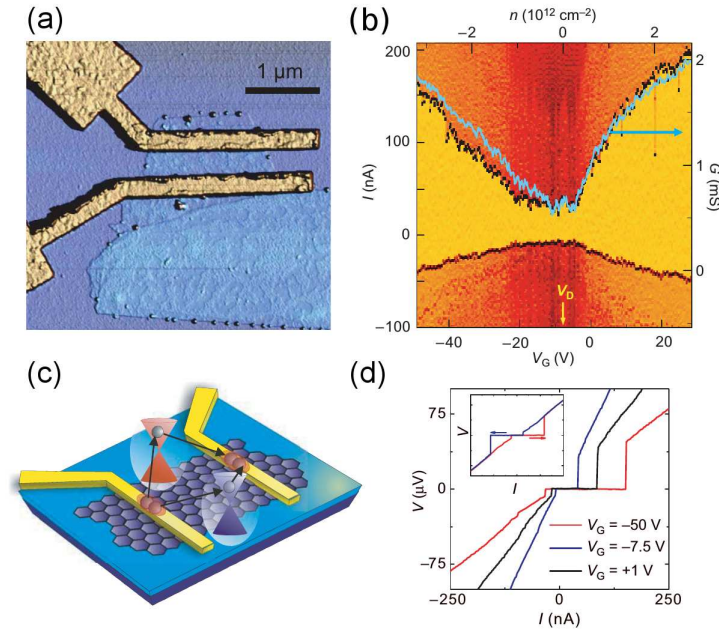


Figure 1.3: Atomic force microscope image of a graphene sample in contact with two superconducting electrodes. (b) Bipolar current measured in the superconducting graphene device of (a) showing a finite supercurrent at the Dirac point. The superconducting regime is shown in yellow in this color-scale plot where the differential resistance is zero. (c) Schematic layout of electron-hole pair transport through graphene in the different K and K' valleys. (d) Current-voltage I - V characteristics of graphene superconducting junction for different values of the gate voltage (V_G), which shift the Fermi energy level, showing the proximity-induced supercurrent flowing at zero voltage. Adapted from Ref. [58].

acteristics appear as a manifestation of the Dirac nature of carriers in graphene, where instead of the conventional Andreev retro-reflection with electron and hole retracing the same time-reversed path, Andreev scattering at superconductor-normal interface in graphene follow a specular scattering of the reflected particle. In this specular Andreev reflection, the component of the velocity parallel to the interface of the reflected hole is inverted, and therefore it does not retrace any longer the path of the incoming electron. Inspecting the band dispersion of graphene one can find the conditions needed to induce such specular Andreev conversion. In normal metals where usually the Fermi energy is pinned far away above the valence band, an intraband conversion is known to lead to a typical Andreev retro-reflection. In contrast, the linear energy band of graphene with the Fermi energy at Dirac point, where conduction and valence band touch each

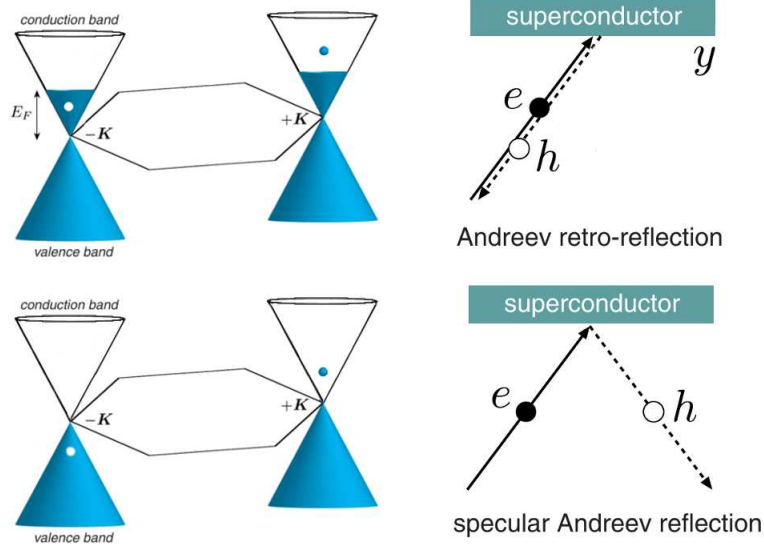


Figure 1.4: (Right) Andreev retro-reflection and specular Andreev reflection at the interface superconductor-normal in graphene. (Left) Intra-band and inter-band conversion mechanisms in the band excitation structure for retro and specular Andreev reflection respectively. Adapted from Ref. [61].

other, allow an interband conversion. Specular Andreev reflection can be derived from the analysis of the linear dispersion in this interband conversion [60, 61]. A similar analysis leads to a conventional retro-reflection in graphene once the Fermi energy is shifted away from Dirac point such that conversion occur in the same band (see Fig. 1.4).

After the experiment of Mospugno and co-workers, the Josephson effect for Dirac fermions was later verified in diffusive regime with $L \approx 1\mu m$ [62, 63]. It was just a matter of time before subsequent efforts were devoted to induce superconductivity in graphene in a more effective way. For instance, highly transparent interfaces were achieved by growing electrodes with critical temperature T_c higher than one found in Al electrodes. To cite some of them, Pt/Ta [64], Pb/In [65], Pb/Pd [66], Nb/Pd₂ [67] and NbN [68] electrodes with T_c lying between 2.5K and 12K, were successfully implemented in superconducting graphene-based junctions. Another challenge usually faced in graphene devices is the presence of spatial inhomogeneities. While in some cases, an annealing current is applied in order to remove residues [64], signatures of diffusive supercurrent under doping inhomogeneities have been also reported for long junction [67]. On the contrary, excellent ballistic transport has been observed in graphene junctions

suspended between superconducting electrodes [68]. Another advance aimed at the control of the supercurrent in graphene Josephson junctions, claims the possibility of switching off the current through a p-n potential barrier, thus, making a graphene Josephson junction suitable for quantum-state engineering [69]. Nonetheless, since the sole application of a p-n gate voltage does not ensure the presence of the observed supercurrent off state, the authors claim the presence of ripples as the dephasing mechanism responsible for the suppression of the Josephson current. The relevance of decoherence in the diffusion of the coherent pair electron-hole between the graphene-superconductor interfaces has been the subject of recent experimental investigation, where the microfabrication of a graphene-based Andreev interferometer designed to tune the amplitude of the dephasing, explored new features of the proximity effect in graphene [70].

1.4 Motivation of this thesis

The interplay between two-dimensional electronic aspects of graphene and superconductivity represents a poorly-explored scenario with potential new physics. Not only single layer, but multilayer graphene structures are also a very interesting area to study superconducting characteristics of massive fermions. In most of the cases, theoretical studies are complicated or require approximations providing a restricted description of the solution. For instance, the lack of translational invariance makes it difficult for any analytical procedures to solve these problems. On the other hand, numerical solutions demand a large amount of computational resources since the typical size of these systems involves hundreds of thousands of atoms. The aim of this thesis is the development of a highly-efficient numerical solution for the superconducting correlations in two-dimensional graphene and graphene-layered structures related to some state-of-art experimental advances. Within the Bogoliubov-de Gennes formalism, we implemented an efficient numerical method based on the expansion of the Gor'kov-Green functions in terms of Chebyshev polynomials. In addition, a large speed up is achieved by developing algorithms using parallel computation on graphic processing units (GPUs) which allowed us to solve efficiently systems involving hundreds of thousands atoms. In this way, we are allowed to deal with a wide variety of problems, like the possibility of switching-off the supercurrent in a biased bilayer graphene Josephson junction, or the influence of the stacking order in the intrinsic superconducting properties of multilayer graphene, among others.

1.5 Outline of this thesis

In **chapter 1** we have introduced briefly some historical facts about the discovery of graphene and its relevance in condensed matter physics and new technological applications. Next, we presented the most relevant experimental evidences of superconductivity traces in carbon-based compounds reported till now with particular focus on carbon layered structures. Finally, attention is payed to state-of-the-art fabrication of superconducting graphene devices based on proximity effect.

In **chapter 2** we give a brief introduction of electronic properties of single, bilayer and multilayer graphene. Attention is mainly focused on the tight-binding description of these layered structures. Then, we give a description of BCS theory arriving later to a general formulation of the Bogoliubov de-Gennes equations. Next, the numerical method used here is described in detail.

In **chapter 3** we present a self-consistent solution for the pair correlation in a bilayer graphene Josephson junction as an extension of the single-layer case, where both graphene layers are in contact with two superconducting leads. We study in this chapter the proximity effect and the behavior of the dc Josephson current in such junctions for different regimes. In addition, a bias potential difference between the layer is applied in order to create a gap. We address the question of the possibility to switch-off the supercurrent through this induced gap.

In **chapter 4**, inspired by recent experimental observations and other theoretical studies, we present a description of the intrinsic superconductivity in multilayer graphene. Solving self-consistently for the order parameter, we study the effect of different stacking configurations in the multilayer graphene. In addition, the effect of external factors like an electric field applied and a homogeneous doping are also investigated.

In **chapter 5**, motivated by the interesting results obtained in Chapter 4, we made a study of multilayer graphene Josephson junctions. Different from the methodology implemented in Chapter 2, we perform here a 3-dimensional description of the proximity effect in multilayer graphene considering different stacking orders.

In **chapter 6** we investigate the effect of disorder on a single-layer graphene Josephson junction. Inspired by different experimental advances, different types of disorder like vacancies, the presence of lattice deformations like ripples, and the presence of charged impurities are considered. The presence of these types of disorder shown to be important for the Andreev states and the critical Josephson current.

2

Theoretical framework and numerical methods

2.1 Graphene basics

2.1.1 Crystal lattice structure

Graphene is a two-dimensional arrangement of carbon atoms in a honeycomb-like lattice. Since a hexagonal lattice does not constitute a Bravais lattice, a triangular lattice with two atoms A and B in the basis, or equivalently, two triangular sublattices with different single atomic basis A and B , are considered instead. The unitary vectors for the triangular sublattice with atoms A for instance, are defined as $\vec{a}_{1,2} = (3, \pm\sqrt{3})a/2$ where $a \approx 0.142\text{nm}$ is the bond length between carbon atoms (see Fig 2.1(a)). The reciprocal vectors satisfying the relation $\vec{a}_i \cdot \vec{b}_j = 2\pi\delta_{ij}$ are given by: $\vec{b}_{1,2} = (1, \pm\sqrt{3})2\pi/3a$. Therefore the first Brillouin zone (1BZ) can be taken as the region delimited by the hexagon with vertices at the six points $K = (\pm 1, \sqrt{3})2\pi/3a, (0, \pm 4\pi/3\sqrt{3}a)$ and $K' = (1, -\sqrt{3})2\pi/3a, (0, \pm 4\pi/3\sqrt{3}a)$ (see Fig. 2.1(b)). These inequivalent high-symmetry points K and K' cannot be connected by reciprocal vectors \vec{b}_1 and \vec{b}_2 and are time-reversal partners of each other.

A minimal model for the electronic structure of graphene involves the hopping between sublattice A and the three atoms in the surrounding B sublattices along the nearest-neighbors vectors $\vec{\delta}_1 = (1, \sqrt{3})a/2, \vec{\delta}_2 = (1, -\sqrt{3})a/2$ and $\vec{\delta}_3 =$

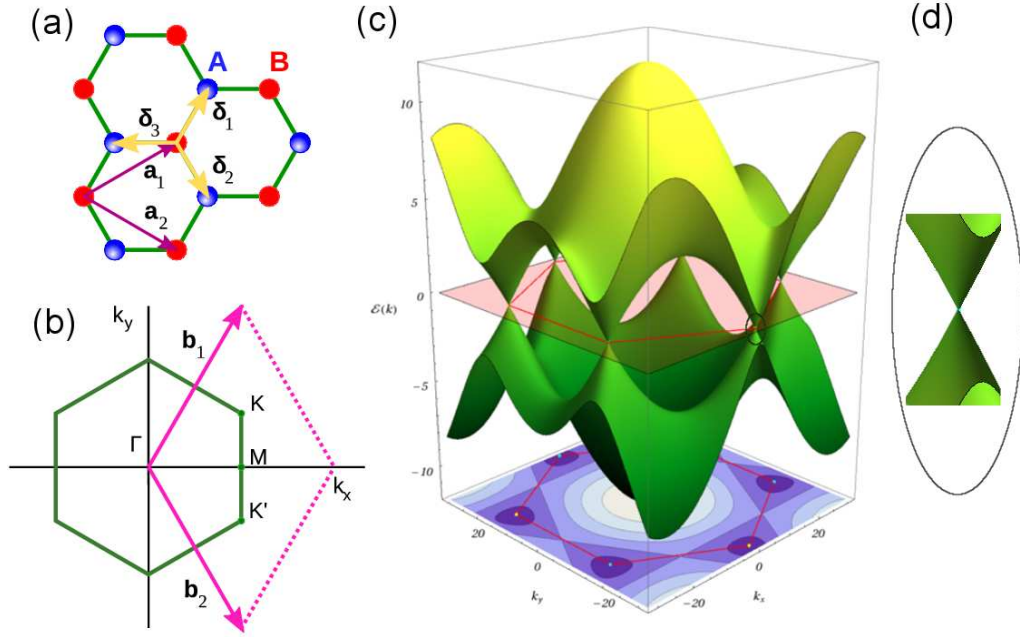


Figure 2.1: (a) Graphene lattice structure consistent of two sublattices A and B. Sublattice A is defined by the lattice vectors (\vec{a}_1, \vec{a}_2) . Vectors $(\vec{\delta}_1, \vec{\delta}_2, \vec{\delta}_3)$ connect sublattices A and B. (b) Reciprocal lattice defined by the vectors (\vec{b}_1, \vec{b}_2) and hexagonal first Brillouin zone with highly symmetry points. (c) The band structure of graphene. (d) Canonical dispersion around K or K' points. Adapted from Ref. [71].

$(-1, 0)a$.

Carbon atoms in graphene are connected by strong in-plane covalent bonds due to sp^2 orbitals, which follow from the sp hybridization of the isolated carbon orbitals $2s$, $2p_x$ and $2p_y$. As a consequence, high-energy σ bands emerge, while out-of-plane orbitals $2p_z$, which do not participate in the in-plane bond, give rise to a low-energy π band. Since there is only one electron per p_z orbital for each carbon atom, the Fermi level lies at the zero energy axis and therefore low-energy excitations are mainly carried out by π states [72]. Hence, an accurate description can be made within a simple tight-binding model considering only the interaction between $2p_z$ -orbitals localized in nearest-neighbors atomic sites. Lets consider the normalized wavefunction $\varphi(\mathbf{r}_{A,B}) = \langle \mathbf{r} | \varphi_{A,B} \rangle$ for the $2p_z$ -orbitals at atomic sites in sublattices A and B defined by the vectors $\vec{r}_A = n_1\vec{a}_1 + n_2\vec{a}_2$ and $\vec{r}_B = m_1\vec{a}_1 + m_2\vec{a}_2 + \vec{\delta}_3$ with n_1, n_2, m_1 and m_2 being integer numbers. The respective tight-binding Hamiltonian can be written down as

follows:

$$\mathcal{H} = -t \sum_{\mathbf{r}_n} \sum_l |\varphi_B(\mathbf{r}_A + \delta_l)\rangle \langle \varphi_A(\mathbf{r}_A)| + \text{h.c.}, \quad (2.1)$$

where $t = \langle \varphi_B(\mathbf{r}_A + \delta_l) | \mathcal{H} | \varphi_A(\mathbf{r}_A) \rangle \approx 2.4eV$ is the transfer or hopping integral matrix between nearest-neighbors, whereas the overlap integral matrix is neglected, *i.e.* $\langle \varphi_B(\mathbf{r}_A + \delta_l) | \varphi_A(\mathbf{r}_A) \rangle = 0$. In addition, atoms in the A and B sublattices are considered equivalent and therefore their on-site energy is equal, *i.e.* $\langle \varphi_A | H | \varphi_A \rangle = \langle \varphi_B | H | \varphi_B \rangle$. For simplicity the former integral is assumed to be null and one can consider the following Bloch wavefunctions for both single-orbital φ_A and φ_B states:

$$\psi_i(\vec{k}) = \frac{1}{\sqrt{N}} \sum_{\vec{r}_i} \exp(i\vec{k} \cdot \vec{r}_i) \varphi_i(\vec{r}_i), \quad (2.2)$$

where $i = A, B$ and N is the total number of unit cells. The Hamiltonian can be re-written in the basis of the two-component wavefunction $\psi = (\psi_A, \psi_B)$, which satisfies the Schrödinger equation $\mathcal{H}\psi = E\psi$, in the following matrix form:

$$\mathcal{H}(\vec{k}) = \begin{pmatrix} 0 & h(\vec{k}) \\ h^*(\vec{k}) & 0 \end{pmatrix}, \quad (2.3)$$

where

$$h(\vec{k}) = -t \sum_l \exp[i\vec{k} \cdot \vec{\delta}_l] = -t \left[2 \exp\left(\frac{ik_x a}{2}\right) \cos\left(\frac{k_y a \sqrt{3}}{2}\right) + \exp(-ik_x a) \right]. \quad (2.4)$$

A straightforward calculation of the eigenvalues through the secular equation, $\det[\mathcal{H} - E\mathcal{I}] = 0$ where \mathcal{I} is the identity matrix, leads to the following dispersion relation, as was deduced by Wallace in 1947 [2]:

$$E = \pm t \sqrt{1 + 4 \cos^2\left(\frac{\sqrt{3}ak_y}{2}\right) + 4 \cos\left(\frac{\sqrt{3}ak_y}{2}\right) \cos\left(\frac{3ak_x}{2}\right)}. \quad (2.5)$$

The corresponding energy bands described by the dispersion relation (2.5) are shown in Fig. 2.1(c). One can see that the conduction ($E > 0$) and valence ($E < 0$) bands touch each other at the six K and K' corners points where $E(K) = E(K') = 0$. Since only two of these valley points, K and K' , are inequivalent, there exists a two-fold degeneracy, called *valley degeneracy*, which is a direct consequence of equivalence between atoms in sublattice A and B . Thus, besides the pseudospin degree of freedom defined by the two equivalent sublattices, time-reversal states of valleys K and K' give rise to an additional degree of freedom

called isospin. An enlarged view around zero energy shows a linear form of the energy dispersion around the K point, where the Fermi surface is reduced to a singular point and separates the filled valence band with the empty conducting band demonstrating the semi-metallic nature of graphene (see Fig. 2.1(d)).

2.1.2 From tight-binding to Dirac equation

The linear dependence of the dispersion relation in the two-dimensional wave-vector $\vec{k} = (k_x, k_y)$ of Eq. (2.5) around each corner point K and K' , can be easily verified by expanding the non-diagonal element $h(\vec{k})$ in (2.4) around the inequivalent points $K(K') = (0, \pm 4\pi/3\sqrt{3}a)$ for low values of the wavevector $\delta\vec{k} = \vec{K} - \vec{k}$ or $(\delta\vec{k}' = \vec{K}' - \vec{k})$ such that $|\delta\vec{k}|a \ll 1$. A straightforward calculation leads to the effective Hamiltonian with the following form for K and K' [73]:

$$\mathcal{H}_{\vec{K}, \vec{K}'}^{\text{eff}} = \alpha \hbar v_F \begin{pmatrix} 0 & \delta k_x \pm i\delta k_y \\ \delta k_x \mp i\delta k_y & 0 \end{pmatrix}, \quad (2.6)$$

where the phase α can be excluded by a unitary transformation of the basis function and the Fermi velocity $v_F = 3at/2\hbar \approx 10^6\text{m/s}$ defines the speed of the carriers in graphene at low-energy excitation. In a more compressed notation, using the Pauli matrices, the Dirac Hamiltonian of relativistic particles results:

$$\mathcal{H}_{\vec{K}, \vec{K}'} = \hbar v_F (\delta k_x \sigma_x + \delta k_y \sigma_y). \quad (2.7)$$

The Hamiltonian (2.7) describes two-component independent states with wavevector centered at the K and K' valleys. A complete description involves a four-component spinor $\varphi = (\varphi_A, \varphi_B, \varphi'_B, \varphi'_A)$ containing both valleys.

2.1.3 Bilayer graphene

The tight-binding description performed for a single-layer graphene can be easily extended to the case of two coupled graphene layers, named bilayer graphene. These layers are bonded by van der Waals forces, which are much weaker than the in-plane covalent bonding in graphene. This weakness makes experimental techniques, like mechanical exfoliation suitable for obtaining graphene and few-layer graphene samples in the laboratory. In fact, together with the observation of single layer graphene, bilayer graphene was also identified among the exfoliated graphite samples [13]. Separated by a distance $c = 0.3\text{nm}$, much larger than the in-plane interatomic distance, the layers are stacked in Bernal or AB configuration as shown in Fig. 2.2(a) where the upper layer is shifted with respect to the lower one such that the atoms in the sublattice \tilde{A} in the upper layer and B

in the lower layer lies exactly on top of one another. Whereas, the atomic position of sublattices \tilde{B} and A project at the center of hexagon in the adjacent layer. A simple tight-binding model for bilayer graphene may therefore involve only an interlayer coupling with a hopping parameter $t_\perp \approx 0.4\text{eV}$ [74, 75] between atoms in sublattice \tilde{A} and those in B . Under this assumption, the tight-binding Hamiltonian (2.1) is adapted to the bilayer graphene case as follows:

$$\mathcal{H} = -t \left[\sum_{\vec{r}_A, l} |\varphi_B(\vec{r}_A + \delta_l)\rangle \langle \varphi_A(\vec{r}_A)| + \sum_{\vec{r}_{\tilde{A}}, \tilde{l}} |\varphi_{\tilde{B}}(\vec{r}_{\tilde{A}} + \tilde{\delta}_{\tilde{l}})\rangle \langle \varphi_{\tilde{A}}(\vec{r}_{\tilde{A}})| \right] - t_\perp \sum_{\vec{r}_{\tilde{A}}} |\varphi_B(\vec{r}_{\tilde{A}})\rangle \langle \varphi_{\tilde{A}}(\vec{r}_{\tilde{A}})| + \text{h.c.}, \quad (2.8)$$

where \tilde{r}_n and $\tilde{\delta}_{\tilde{l}}$ are the shifted in-plane coordinates and nearest-neighbors vectors, respectively. Since there are four atoms per unit cell, Bloch states are described according to the four-component wavefunction $\psi(\vec{k}) = (\psi_A, \psi_{\tilde{B}}, \psi_{\tilde{A}}, \psi_B)$ where the tight-binding Hamiltonian (2.8) has the following matrix form:

$$\mathcal{H}(\vec{k}) = \begin{pmatrix} 0 & 0 & 0 & h^*(\vec{k}) \\ 0 & 0 & h(\vec{k}) & 0 \\ 0 & h^*(\vec{k}) & 0 & t_\perp \\ h(\vec{k}) & 0 & t_\perp & 0 \end{pmatrix} = \begin{pmatrix} H_{11} & H_{12} \\ H_{21} & H_{22} \end{pmatrix}, \quad (2.9)$$

with H_{ij} being 2×2 matrix blocks. Neglecting all other interlayer interactions between carbons atoms other than those in the dimer sites (\tilde{A}, B), one can easily derive an effective Hamiltonian for low-energies, $E \ll t_\perp$, considering in this case $H_{22} - E\mathcal{I} \rightarrow H_{22}$ such that [76]:

$$\det[\mathcal{H} - E\mathcal{I}] = \det[H_{11} - H_{12}(H_{22} - E\mathcal{I})^{-1}H_{12} - E\mathcal{I}] \det[H_{22} - E\mathcal{I}] \approx -t_\perp^2 \det[H_{11} - H_{12}H_{22}^{-1}H_{12} - E\mathcal{I}]. \quad (2.10)$$

Approximating for low-lying bands around the $K(K')$ points in the same way as it was done for graphene, we arrive at the following form for the Hamiltonian (2.9) [77]:

$$\mathcal{H}_{\vec{K}, \vec{K}'}^{\text{eff}} = \frac{\hbar^2}{2m^*} \begin{pmatrix} 0 & (\delta k_x \mp i\delta k_y)^2 \\ (\delta k_x \pm i\delta k_y)^2 & 0 \end{pmatrix}, \quad (2.11)$$

where the solution of the secular equation (2.10) leads to a quadratic dispersion $E(k) = \pm \hbar^2 \delta k^2 / 2m^*$ for both K and K' , where $\delta k^2 = \delta k_x^2 + \delta k_y^2$ and $m^* =$

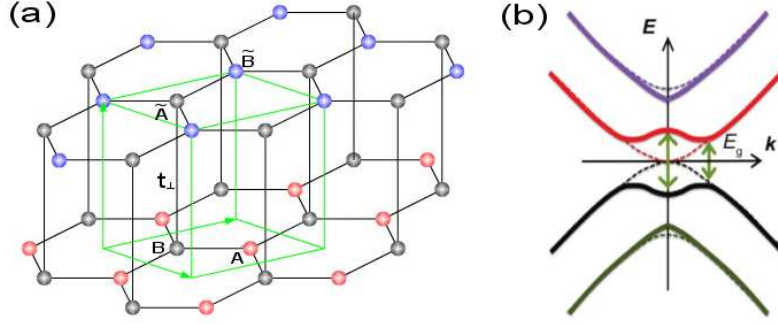


Figure 2.2: (a) Bilayer graphene lattice made of two coupled graphene layers in Bernal stacking where only atoms in sublattice \tilde{A} in the upper layer are connected to atoms in sublattice B through an interlayer coupling t_{\perp} . (b) Band structure for unbiased (dashed curves) and biased bilayer graphene (solid curves). Adapted from Ref. [79].

$t_{\perp}/2v_F^2$ represents the effective mass of particles in bilayer graphene. Thus, this reduced picture of the electronic band structure, which only includes non-dimer orbitals ($\psi_A, \psi_{\tilde{B}}$) [77, 78], shows that massless particles in graphene become massive particles by means of an interlayer interaction in bilayer graphene. Again, K and K' valleys points remain degenerate at the Fermi energy preserving the graphene semimetal character for the bilayer case. A more accurate approximation involving a wider energy range can be obtained for the dispersion relation of bilayer graphene around the valleys [77]:

$$E_{\pm}^{\pm} = \pm \frac{t_{\perp}}{2} \pm \sqrt{\frac{t_{\perp}^2}{4} + (\hbar v_f k)^2}. \quad (2.12)$$

Here, additional to the low-energy bands E_+ touching at the Dirac point found in (2.11), two high-energy bands E_- emerge as a consequence of direct coupling between the dimer sites (see Fig. 2.2(b)). One of the most remarkable features of electronic band structure in bilayer graphene is the possibility to control a tunable gap through a bias potential V_g applied between the layers [16, 77, 80, 81]. This switch-off ability of bilayer graphene has potential applications in field effect-transistor technology. A theoretical description of bilayer graphene as having a semiconductor gap can be achieved by introducing a symmetric energy potential V_g between the layers, which can be done through the transformations: $H_{11} \rightarrow H_{11} + U$ and $H_{11} \rightarrow H_{11} - U$ for the Hamiltonian blocks in (2.9), where U is the 2×2 matrix:

$$U = \begin{pmatrix} V_g/2 & 0 \\ 0 & -V_g/2 \end{pmatrix}. \quad (2.13)$$

Considering that this bias potential is restricted to $\hbar v_F k \ll V_g \ll t_\perp$, the low-lying energy bands are described by the following relation around the ungapped $K(K')$ valley points [82]:

$$E(k) = \pm \left(\frac{V_g}{2} - \frac{V_g \hbar^2 k^2}{t_\perp^2} k^2 + \frac{\hbar^4 v_F^4}{t_\perp^2 V_g} k^4 \right). \quad (2.14)$$

The gapped band structure appears in Fig. 2.2(b) resembling a ‘‘Mexican hat’’. Note that the minimum of the conduction band and the maximum of the valence band are not at the symmetry points K and K' anymore, and the dependence of the gap Δ_g on the bias potential goes according to $\Delta_g = V_g \sqrt{t_\perp^2 / (t_\perp^2 + V_g^2)}$ showing that this gap saturates to a value $\Delta_g = t_\perp$ for values of $V_g \geq t_\perp$.

2.1.4 Multilayer graphene

So far we have described the electronic characteristics of single and bilayer graphene within a tight-binding formalism. In order to draw up an effective model for graphite we can expand the previous model to multiple layers. Certainly, graphite is composed of many graphene layers one above another linked by van der Waals forces. Since van der Waals bonding is much weaker when compared to the in-plane covalent carbon bonding, graphite is considered to have a layered structure. Given the weakness of the interlayer interactions it is expected that the electronic characteristics of graphite might resemble those found in graphene single layer. However, as seen for bilayer graphene, important changes to the linear graphene dispersion occurs as both layers are coupled, allowing interlayer hopping. In multilayer graphene, for instance, the electronic band has been found to depend on the number of layers and the relative orientation of one layer with respect to its neighbors [83]. Despite the fact that there is always in-plane azimuthal disorder, even for graphite samples with the highest degree of three-dimensional ordering like HOPG [84, 85], graphene layers stacked in a staggered or Bernal configuration are most commonly found in natural graphite. This is the case for instance when a third layer is added on top of bilayer graphene and the shift between the additional layer and the top layer make it lies exactly on top of the bottom layer in an ABA configuration (see Fig. 2.3). In another case, a more symmetric stacking configuration can be achieved when all layers are shifted with respect to their neighbors such that inversion symmetry is preserved for any number of layers. This rhombohedral, or ABC stacking (see Fig. 2.3), is rarely found in natural graphite and was believed for a long time to be a defect in the bulk structure until this could be induced by mechanical treatment in Bernal graphite samples. Tight-binding description can be performed by considering the basis wavefunctions $\psi_{n,A}(\vec{k})$ and $\psi_{n,B}(\vec{k})$

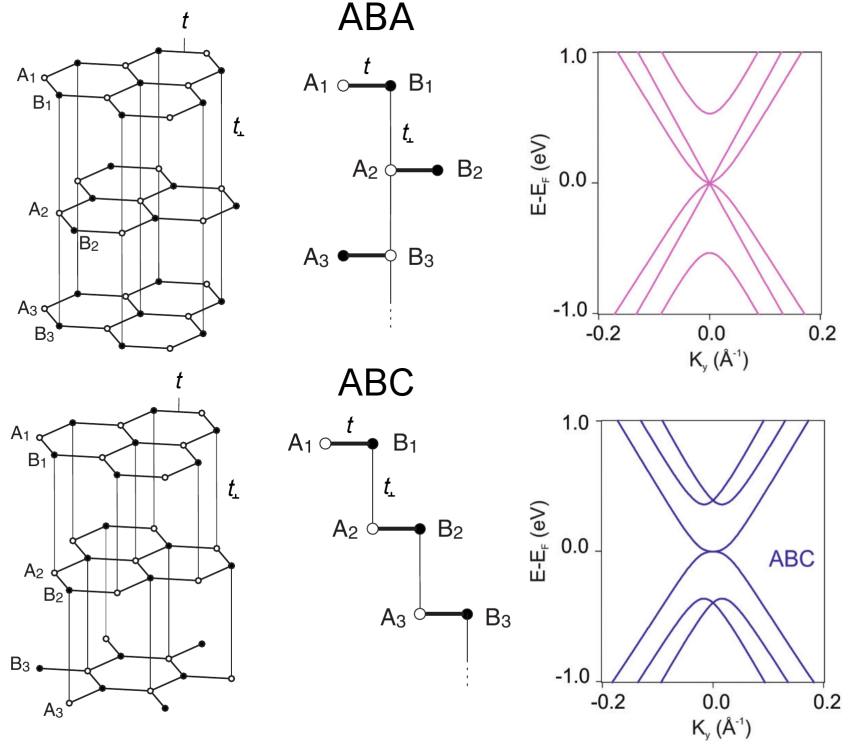


Figure 2.3: Schematic layout and side view of a multilayer graphene structure stacked in two different configurations: Bernal or ABA (top) and Rhombohedral or ABC (bottom). Sublattices A and B are coupled by t within the same layer, while interlayer coupling is described by t_{\perp} . Integer coordinate z corresponds to the index layer. Corresponding energy band structure is shown also. Adapted from Ref. [86].

for $n = 1, 2, \dots, N$ where N is the total number of graphene layers. The system of Schrödinger equations for these wavefunction can be simplified and solved under an infinite sequences of layers and the assumption of periodicity in the vertical axis leading to the following expression for the energies in the bulk [2]:

$$E(\vec{k}, \xi_n) = t_{\perp} \cos \xi_n \pm \sqrt{|h(\vec{k})|^2 + t_{\perp}^2 \cos^2(\xi_n)}, \quad (2.15)$$

where $\xi_n = \pi n / (N + 1)$ are discrete values with $n = 1, 2, \dots, N$ and $h(\vec{k})$ is defined in Eq. (2.4). One can easily prove that the relation (2.15) is reduced to the expressions (2.5) and (2.12) for the energy dispersion of single and bilayer graphene for $n = 1, 2$, respectively. For those cases beyond two layers ($N > 2$), solutions of the system of Eq. (2.15) show a remarkable different dependence on

the parity of the total number of layers N [86]. For even N , an equal number of conduction and valence parabolic bands appear touching at the Fermi energy and resulting in valley degeneracy at K and K' points. Interestingly, for the cases with odd N both linear and parabolic bands are present and the coexistence of Dirac massive fermions is found (an example is shown in Fig. 2.3) [87, 88]. The evolution of the electronic structure for N -stacked graphene layers in the rhombohedral configuration is even more particular [76, 89]. For a finite number of layers N all the dimer orbitals can be excluded in the first approximation as it was done in order to arrive at the effective Hamiltonian (2.11). Thus, due to the spatial inversion symmetry only one non-dimer site per surface remains. Consequently the effective Hamiltonian for the low-lying band can be written as [76]:

$$\mathcal{H}_{\vec{K}, \vec{K}'}^{\text{eff}} = -\frac{(\hbar v_F)^N}{t^{N-1}} \begin{pmatrix} 0 & k^{*N} \\ k^N & 0 \end{pmatrix}. \quad (2.16)$$

Therefore we have a power-law dispersion for the low-energy spectrum according to $E(k) = \pm(\hbar^N v_F^N / t_{\perp}^{N-1})k^N$ as a function of the in-plane moment k around the valleys K and K' . This flat band shows another particular characteristic as the corresponding density of states (DOS) is divergent at zero energy as this is given by the following equation [89]:

$$\rho(E) \propto E(k)^{(2-N)/N}. \quad (2.17)$$

This divergence is only present at non-dimer sites at the surface since the density of states for all the dimer sites vanishes around zero energy. The same behavior is presented for dimer sites in Bernal or ABA multilayer graphene. However, no singularities are present in this case, only a finite density of states is observed for non-dimer sites around the Fermi energy [89].

2.2 Superconductivity basics

2.2.1 BCS theory

Superconductivity is the phenomenon whereby the resistance of a metal spontaneously drops to zero upon cooling below a critical temperature. Discovered by the Dutch physicist Heike Kamerlingh Onnes in 1911 [90] while measuring the resistance of ultrapure mercury cooled by liquefied Helium. A satisfactory understanding of this phenomenon appeared decades later with the formulation of the first microscopy theory of superconductivity proposed by Bardeen, Cooper and Schrieffer [91]. The fundamental idea in the BCS theory is the creation of

a many-particles bound-state from the formation of Cooper pairs [92]. Since these Cooper pairs are made of two electrons with opposite spin (in an isotropic superconductor) and their total spin is zero, they are considered as bosons and therefore the condensation of all Cooper pairs occurs in the superconducting ground-state. The absence of resistance at finite temperature is then explained by the formation of this condensate since scattering of an electron by lattice vibrations, which is the only mechanism of electron scattering in the absence of impurities and lattice defects, requires a huge amount of energy, equivalent to the change of momentum needed to scatter the collective excitation of all the Cooper pairs involved in the coherent superconducting ground state. Thus, the coherent propagation of paired electrons in a superconductor is given by this collective excitation modes of the Cooper pairs with individual size corresponding to the coherence length predicted by Pippard [93] as a characteristic distance of superconductivity. At this length scale, despite their electrostatic strong repulsion, paired electrons are indirectly attracted to each other by a weak electron-phonon interaction [94] which was proven to be the key mechanism for superconductivity after the observation of the dependence of the superconducting transition temperature on the Debye frequency in an isotope of mercury [95].

This pairing mechanism as suggested by BCS theory, might lead to an attractive momentum-independent pairing potential, $V_{k,k'}$, which become zero for excitation energies above the Debye energy, with respect to the Fermi level. In addition, the ground-state must be constructed of pairs according to the following wavefunction:

$$\Psi_{\text{BCS}} = \prod_k (u_k + v_k c_{k\uparrow}^\dagger c_{-k\downarrow}^\dagger) |0\rangle, \quad (2.18)$$

where $|0\rangle$ is the ground state and $c_{k\uparrow}^\dagger$ creates an electron with momentum k and spin \uparrow . The BCS Hamiltonian capturing this low-energy physics can be written as follows:

$$\mathcal{H}_{\text{BCS}} = \sum_{k,\sigma} \epsilon_k c_{k\sigma}^\dagger c_{k\sigma} + \sum_{k,k'} V_{k,k'} c_{k\uparrow}^\dagger c_{-k\downarrow}^\dagger c_{-k'\downarrow} c_{k'\uparrow}, \quad (2.19)$$

where the effective interaction $V_{k,k'}$ has the form:

$$V_{k,k'} = \begin{cases} -g_0, & \text{for } |\epsilon_k| < \omega_D \\ 0 & \text{otherwise} \end{cases}, \quad (2.20)$$

and ω_D is the Debye energy. The long-range aspect of this theory given by the interaction range of order $1/\Delta k \sim v_F/\omega_D \sim O(\epsilon_F/\omega_D) \times a$ where a is the lattice spacing, allows us to obtain a solution of the BCS Hamiltonian (2.19) through mean-field theory [96]. Defining the operator $\Lambda_k = c_{-k'\downarrow} c_{k'\uparrow}$, the BCS

interaction term in (2.19) can be expanded in powers of the fluctuation operator $\delta\hat{\Lambda} = \hat{\Lambda} - \langle\hat{\Lambda}\rangle$ in the following form:

$$\hat{\Lambda}^\dagger\hat{\Lambda} = \langle\hat{\Lambda}^\dagger\rangle\hat{\Lambda} + \hat{\Lambda}^\dagger\langle\hat{\Lambda}\rangle + \langle\hat{\Lambda}^\dagger\hat{\Lambda}\rangle - \delta\hat{\Lambda}\delta\hat{\Lambda}. \quad (2.21)$$

In the thermodynamic limit one can neglect the last term such that the resulting mean-field Hamiltonian looks like:

$$\mathcal{H}_{\text{MFT}} = \sum_{k\sigma} \epsilon_k c_{k\sigma}^\dagger c_{k\sigma} + \sum_k \left[\Delta_k^* c_{k\uparrow}^\dagger c_{-k\downarrow}^\dagger + \Delta_k c_{-k\downarrow} c_{k\uparrow} \right] + |\Delta|^2/g_0, \quad (2.22)$$

where the imaginary expectation value $\Delta_k = -g_0 \sum_k \langle c_{-k\downarrow} c_{k\uparrow} \rangle$ is defined as the superconducting order parameter.

A more compact notation allows us to re-write the mean-field Hamiltonian (2.22) unifying kinetic and pairing terms in a single matrix by using Nambu spinors $\psi^\dagger = (c_{k\uparrow}^\dagger, c_{-k,\downarrow})$ [97]:

$$\mathcal{H}_{\text{MFT}} = \psi_k^\dagger \begin{pmatrix} \epsilon_k & \Delta \\ \Delta^* & -\epsilon_k \end{pmatrix} \psi_k + \frac{|\Delta|^2}{g_0}. \quad (2.23)$$

Diagonalizing this Hamiltonian by using an unitary transformation of the Nambu spinors according to the following Bogoliubov-Valatin transformations [98, 99]:

$$c_{k\uparrow} = \sum_n (u_k^i \gamma_{n\uparrow} - \nu_k^{i*} \gamma_{k\downarrow}^\dagger), \quad (2.24)$$

$$c_{k\uparrow} = \sum_n (u_k^i \gamma_{n\downarrow} + \nu_k^{i*} \gamma_{k\uparrow}^\dagger), \quad (2.25)$$

where electron and holes are mixed by the quasi-particle operators γ_k and γ_k^\dagger , leads to:

$$\mathcal{H} = E_0 + \sum_k E_k (\gamma_{k\uparrow}^\dagger \gamma_{k\uparrow} + \gamma_{k\downarrow}^\dagger \gamma_{k\downarrow}). \quad (2.26)$$

E_0 can be interpreted as a ground-state energy and the excitation spectrum is given in terms of single-particle energy ϵ_k according to [100]:

$$E_k = (\epsilon_k^2 + \Delta_k^2)^{1/2}. \quad (2.27)$$

A minimum excitation energy, when $\epsilon_k = 0$, evidences the gap energy character of the order parameter Δ_k . A clearer picture of this characteristic for isotropic superconductor, where $\Delta_k = \Delta_s$ is momentum-independent, can be observed in the density of states which is defined as $N(E) = \sum_k \delta(E - E_k)$. In the

continuum limit, the summation can be replaced by an integration over the k -points and introducing the excitation energies (2.27) we obtain:

$$N(E) = \int \frac{d\epsilon_k}{4\pi} \delta(E - (\epsilon_k^2 + \Delta_s^2)^{1/2}). \quad (2.28)$$

Using the property of the Dirac function $\delta(f(x)) = \sum_i \delta(x - x_i) f'(x_i)$, where x_i are the roots of $f(x)$, we have that the density of states has the form:

$$N(E) \sim \begin{cases} E/(E^2 - \Delta_s^2)^{1/2}, & \text{for } E > \Delta_s \\ 0, & \text{for } E < \Delta_s \end{cases}. \quad (2.29)$$

Notice that the density of states (2.29) describes the absence of quase-particles states in a superconducting gap of size $2\Delta_s$ surrounded by squared-root singularities named coherence peaks.

2.2.2 Inhomogenous superconductivity: The Bogoliubov de Gennes equations

The lacking of the translational invariance induced by the presence of lattice defects, impurities or interfaces, makes a k -space description, as it was done so far in the Hamiltonian (2.21), not suitable. Instead, a description of the BCS Hamiltonian in the real space is required. For solving this issue, a reduced attractive Hubbard model is assumed, where the main features of the BCS theory in (2.19) are captured by the following Hamiltonian, written in second quantization formalism:

$$\mathcal{H} = \sum_{\langle i,j \rangle, \sigma} [-t_{ij} - (\mu - \varepsilon_i) \delta_{ij}] c_{i\sigma}^\dagger c_{j\sigma} + \sum_i U_i c_{i\uparrow}^\dagger c_{i\uparrow} c_{i\downarrow}^\dagger c_{i\downarrow}, \quad (2.30)$$

where t_{ij} is the hopping parameter between the nearest-neighbors $\langle ij \rangle$, ε_i is the impurity on-site energy and μ_i is the chemical potential which shifts the Fermi level. The on-site attractive potential, U_i , describes the attractive correlations between electrons with opposite spin sitting on the same atomic site. In this way, the Hubbard Hamiltonian models effectively the usual electron-phonon coupling mechanism in conventional superconductors, where vibrations of the lattice created by electrons, affect in turn other electrons, giving rise to an attractive interaction, which overcomes the repulsive Coulomb correlations.

The same approach as the one considered in (2.22) can be used to approximate the complex many-body problem with interactions to a single-particle one, where an average potential replaces the interaction of all the other particles on

an arbitrary particle. The following mean-field Hubbard Hamiltonian is deduced from the mean-field approach:

$$\mathcal{H} = \sum_{\langle i,j \rangle, \sigma} (-t_{ij} - \mu_i \delta_{ij}) c_{i\sigma}^\dagger c_{j\sigma} + \sum_i (\Delta_i c_{i\uparrow}^\dagger c_{i\downarrow}^\dagger + \Delta_i^* c_{i\downarrow} c_{i\uparrow}), \quad (2.31)$$

where $\Delta_i = U_i \langle c_{i\uparrow} c_{i\downarrow} \rangle$ is the superconducting order parameter and we have neglected the Hartree-shift in the last term of (2.22), which can be absorbed by the chemical potential leaving the properties of the superconducting order parameter unaffected.

Such a Hamiltonian, described by Eq. (2.31), can be diagonalized by an appropriate transformation of the fermionic operators as follows:

$$c_{i\uparrow} = \sum_n (u_n^i \gamma_{n\uparrow} - \nu_n^{i*} \gamma_{n\downarrow}^\dagger), \quad (2.32)$$

$$c_{i\downarrow} = \sum_n (u_n^i \gamma_{n\downarrow} + \nu_n^{i*} \gamma_{n\uparrow}^\dagger). \quad (2.33)$$

This canonical transformation was introduced independently by Bogoliubov [98] and Valatin [99] in 1958. By replacing (2.32) and (2.33) in (2.31) it can be shown that Hamiltonian matrix has a diagonal form, in analogy with the representation of Eq. (2.26) in the k -space, for those values of u_n^i and ν_n^i satisfying the following Bogoliubov-de Gennes (BdG) equations:

$$\begin{pmatrix} \hat{\mathcal{H}}_0 & \hat{\Delta} \\ \hat{\Delta}^\dagger & -\hat{\mathcal{H}}_0 \end{pmatrix} \begin{pmatrix} U_n \\ V_n \end{pmatrix} = E_n \begin{pmatrix} U_n \\ V_n \end{pmatrix} \quad (2.34)$$

with the vectors $U_n^\dagger = (u_n^1, u_n^2, \dots, u_n^N)$ and $V_n^\dagger = (\nu_n^1, \nu_n^2, \dots, \nu_n^N)$. The $N \times N$ matrix $\hat{\mathcal{H}}_0$ in the BdG Hamiltonian (2.30) corresponds to the tight-binding Hamiltonian of the normal states for electrons, which involves the hopping parameter t between nearest neighbors and the chemical potential μ of Hamiltonian (2.31). Meanwhile, the elements of the diagonal matrix $\hat{\Delta}$ correspond to the on-site order parameters of the N atomic sites of the lattice. On the other hand, $-\hat{\mathcal{H}}_0$ represents the normal state Hamiltonian for holes while the entries of the diagonal matrix $\hat{\Delta}^\dagger$ are the complex conjugated of the on-site order parameter. The states $(U_n, V_n)^\dagger$, mixing electron and holes, together with E_n define an eigenvalue problem from which physical properties can be calculated. For instance, using the transformations from Eqs. (2.32) and (2.33) we have that:

$$\begin{aligned} \Delta_i &= U_i \langle c_{i\uparrow} c_{i\downarrow} \rangle \\ &= U_i \left\langle \sum_{n,n'} (u_n^i \gamma_{n\uparrow} - \nu_n^{i*} \gamma_{n\downarrow}^\dagger) (u_{n'}^i \gamma_{n'\downarrow} + \nu_{n'}^{i*} \gamma_{n'\uparrow}^\dagger) \right\rangle \\ &= U_i \sum_n u_n^i \nu_n^{i*} (1 + 2f_n), \end{aligned} \quad (2.35)$$

where we have taken into account that the fermionic operator obeys the Fermi statistic $\langle \gamma_{n\uparrow}^\dagger \gamma_{n\uparrow} \rangle = f_n = 1/[\exp(\beta E_n) + 1]$. A self-consistent estimation of the order parameter can be performed through Eq. (2.35).

2.3 The Chebyshev-Bogoliubov-de Gennes method

A self-consistent solution for the spatially-dependent order parameter is known to provide a suitable way to solve the Bogoliubov de-Gennes equations (2.30) in real space. To compute the order parameter, a numerical treatment of the BdG equations (2.30) is usually needed. Nonetheless, according to the dimension of the system, *i.e.*, the number of atoms involved, the performance of these numerical methods could demand considerable amount of computational resources. For our particular case, the most immediate solution is the direct diagonalization of the BdG Hamiltonian (2.30), providing the eigenvectors and eigenvalues required for the calculation of the order parameter. Diagonalizing this matrix is appropriate in case of finite systems for low dimensions, D , of this matrix. For large systems this method is almost intractable since numerical effort scales as D^3 . This also corresponds to the case of Hermitian matrices as those described by the BdG Hamiltonian (2.30), where the dimension D is twice the number of atomic sites. Thus, a moderate number of atomic sites involving hundreds or few thousands of atoms will imply an already large amount of memory and a considerable number of computational operations. An alternative method for studying large sparse matrices is the recursive Lanczos method [101]. Based on a tri-diagonalization of the matrix in question, the new basis (where the matrix is in fact tridiagonal) obtained through a recursive procedure allows the calculation of the local spectral density or Green function:

$$\mathcal{G}_{ij} = \langle c_i | [E\mathcal{I} - \mathcal{H}]^{-1} | c_j^\dagger \rangle, \quad (2.36)$$

where $|c_i^\dagger\rangle = c_i^\dagger|0\rangle$ creates an electron at the atomic site i where $|0\rangle$ is the ground state. Once the Green function is known, eigenvalues are extracted from its zeros, or conversely physical properties can be directly calculated. The former case holds, for instance, for the local density of states, which corresponds to the imaginary part of the local spectral function according to:

$$N_i(E) = -\frac{1}{\pi} \text{Im} \mathcal{G}_{ii}(E + i\eta), \quad (2.37)$$

where η is a small energy. The Lanczos method proved to be efficient for the approximation of the Green functions and for solving self-consistently the Bogoliubov de-Gennes equations [102, 103]. In spite of this, instabilities in the

numerical algorithm eventually appear, as the basis loses orthogonality during the recursive procedure. A different approach for the computation of the Green function (2.36) is achieved by using an expansion in terms of Chebyshev polynomials. Implemented through the kernel polynomial method (KPM) [104], computational resource consumption scales linearly with the dimension D of the matrix since the most consuming operations consist of multiplications of sparse matrices with vectors. The computational cost of the iterative procedure is similar or slightly better if compared to the Lanczos method. However, it has been demonstrated that the Chebyshev expansion offers certain advantages in terms of precision and stability for matrices with dimension D larger than a million [105]. In addition, this expansion allows us to calculate real and imaginary dynamical correlation functions and spectral functions over the whole energy range at once. Unlike the Lanczos method, where different calculations of the continued fraction are needed in order to find the Green function for different energies. The Chebyshev expansion method has been successfully applied in different problems in solid-state physics [106–110]. In particular, this method becomes very efficient when implemented for solving Bogoliubov de Gennes equations in the case of inhomogeneous superconductivity [111]. In order to implement the Chebyshev expansion technique, Covaci and co-workers described normal-superconducting transition by using a method developed by Gor'kov [112] which leads to two coupled “normal” and “anomalous” Green functions. These Gor'kov-Green functions measure the different pair correlations according to the following 2×2 matrix written within the Nambu formalism [97]:

$$\hat{\mathcal{G}}(t - t') = -\frac{i}{\hbar} \begin{pmatrix} \langle \mathcal{T} c_{i\uparrow} c_{j\uparrow}^\dagger \rangle & \langle \mathcal{T} c_{i\uparrow} c_{j\downarrow} \rangle \\ \langle \mathcal{T} c_{i\downarrow}^\dagger c_{j\uparrow}^\dagger \rangle & \langle \mathcal{T} c_{i\downarrow} c_{j\downarrow}^\dagger \rangle \end{pmatrix}, \quad (2.38)$$

where the operator \mathcal{T} denotes the time-ordering operator. Changing this expression under a temporal Fourier transform leads to:

$$\hat{\mathcal{G}}(\omega) = \begin{pmatrix} \mathcal{G}_{ij}(\omega) & F_{ij}(\omega) \\ F_{ij}^*(\omega) & -\mathcal{G}_{ij}(\omega) \end{pmatrix}, \quad (2.39)$$

where ω is the energy. The upper left element, resembling the ordinary electron correlation of Eq. (2.36), corresponds to the “normal” Green function, which is defined by the following expectation value:

$$\mathcal{G}_{ij}(\omega + i\eta) = \langle c_{i\uparrow} | \frac{1}{\omega + i\eta - \mathcal{H}} | c_{j\uparrow}^\dagger \rangle, \quad (2.40)$$

while the upper right term, named ‘‘anomalous’’ Green function, accounting for the spin-opposite pair correlation, is given by the expression:

$$F_{ij}(\omega + i\eta) = \langle c_{i\uparrow} | \frac{1}{\omega + i\eta - \mathcal{H}} | c_{j\downarrow} \rangle. \quad (2.41)$$

Gor’kov function (2.39) satisfies the equation $(\omega\mathcal{I} - \mathcal{H})\hat{\mathcal{G}}(\omega) = \mathcal{I}$ and it is feasible to find that the anomalous Green function determines the order parameter function:

$$\Delta_i = -\frac{iU_i}{2\pi} \int F_{ii}(\omega + i\eta)(1 - 2f(\omega))d\omega, \quad (2.42)$$

where U_i is the on-site pair potential and $f(\omega)$ corresponds to the Fermi distribution in analogy with expression (2.35). Thus, the normal and anomalous Gor’kov-Green functions provide an useful tool for solving self-consistently the BdG Hamiltonian of Eq. (2.30). As it can be observed from Eq. (2.42) solution is given separately for each lattice point. As was demonstrated by Covaci and co-workers, the expansion of both spectral functions in terms of Chebyshev polynomials offers a powerful alternative route for solving BdG equations in inhomogeneous systems, since limitations imposed by the size of the system can be avoided.

2.3.1 Basic properties of Chebyshev polynomials

Before giving an explicit expression of the Chebyshev expansion, it is worth recalling some basic features of the Chebyshev polynomials. Chebyshev polynomials are a particular set of polynomials satisfying orthogonality relations and therefore an useful tool for the expansion of integrable functions. For this purpose, Chebyshev polynomials are an optimal choice since their expanded series has a good convergence and a close relation to Fourier transforms. Defined on the interval $[-1, 1]$, there are two types of Chebyshev polynomials distinguished by their respective weight function. For instance, Chebyshev polynomials of the first kind T_n with weight function $w(x) = (\pi\sqrt{1-x^2})^{-1}$, define the following orthogonality relation:

$$\langle T_n | T_m \rangle = \int_{-1}^1 \frac{T_n(x)T_m(x)}{\pi\sqrt{1-x^2}} dx = \frac{1 + \delta_{n,0}}{2} \delta_{n,m}. \quad (2.43)$$

An explicit expression for these Chebyshev polynomials is deduced from the latter orthogonality relation as follows :

$$T_n(x) = \cos[n \arccos(x)], \quad (2.44)$$

which satisfies the following recursion relations:

$$\begin{aligned} T_0(x) &= 1, \quad T_1(x) = x, \\ T_{n+1}(x) &= 2xT_n(x) - T_{n-1}(x). \end{aligned} \quad (2.45)$$

In the same way, the Chebyshev polynomial of second kind U_n are defined according to the weight function $w(x) = \pi\sqrt{1-x^2}$ as follows:

$$U_n(x) = \frac{\sin[(n+1)\arccos(x)]}{\sin[\arccos(x)]}. \quad (2.46)$$

Both sets of Chebyshev polynomials are related by the Hilbert transformation:

$$\mathcal{P} \int_{-1}^1 \frac{T_n(y)dy}{(y-x)\sqrt{1-y^2}} = \pi U_{n-1}(x). \quad (2.47)$$

2.3.2 Expansion of the Gor'kov-Green functions

An integrable function $f(x)$ defined within the interval $[-1, 1]$ can be expanded in terms of Chebyshev polynomials of the first kind as follows:

$$f(x) = \frac{1}{\pi\sqrt{1-x^2}} \left[a_0 + 2 \sum_{n=1}^{\infty} a_n T_n(x) \right], \quad (2.48)$$

where the pre-factor $1/(\pi\sqrt{1-x^2})$ is included such that the integral which defines the moments becomes independent of the weight function as follows:

$$a_n = \int_{-1}^1 f(x) T_n(x) dx. \quad (2.49)$$

Hence, the form of the above integral allows us to use the relations (2.45) for the recursive calculation of these modified moments.

To further expand normal and anomalous Green functions, a dynamical correlation function for two arbitrary fermionic operators \hat{A} and \hat{B} is defined as follows [104]:

$$\begin{aligned} \langle \hat{A}; \hat{B} \rangle^\omega &= \lim_{\eta \rightarrow 0} \langle 0 | \hat{A} \frac{1}{\omega + i\eta - \mathcal{H}} \hat{B} | 0 \rangle \\ &= \lim_{\eta \rightarrow 0} \sum_{k=0}^{D-1} \frac{\langle 0 | \hat{A} | k \rangle \langle k | \hat{B} | 0 \rangle}{\omega + i\eta - E_k}, \end{aligned} \quad (2.50)$$

where E_k corresponds to the eigenvalues of the Hamiltonian \mathcal{H} in the basis extended by the eigenstates $|k\rangle$ and η is a small positive number. After decomposing the dynamical correlation function by using the Plemelj-Dirac formula: $\lim_{\eta \rightarrow 0} 1/(x + i\eta) = \mathcal{P}(1/x) - i\pi\delta(x)$, an expansion in terms of Chebyshev polynomials of the first kind is performed for the imaginary part of the function (2.48):

$$\text{Im}\langle\hat{A};\hat{B}\rangle^\omega = \pi \sum_{k=0}^{D-1} \langle 0|\hat{A}|k\rangle \langle k|\hat{B}|0\rangle \delta(\omega - E_k) \quad (2.51)$$

$$= -\frac{1}{\sqrt{1-\omega^2}} \left(a_0 + 2 \sum_{n=1}^{\infty} a_n T_n(\omega) \right). \quad (2.52)$$

By performing the integral (2.49) one can arrive at the following expectation value for the calculation of the moments as follows:

$$\begin{aligned} a_n &= \frac{1}{\pi} \int_{-1}^1 \text{Im}\langle\hat{A};\hat{B}\rangle T_n(\omega) d\omega \\ &= \sum_{k=0}^{D-1} \langle 0|\hat{A}|k\rangle \langle k|\hat{B}|0\rangle T_n(E_k) \\ &= \sum_{k=0}^{D-1} \langle 0|\hat{A}T_n(\mathcal{H})|k\rangle \langle k|\hat{B}|0\rangle \\ &= \langle 0|\hat{A}T_n(\mathcal{H})\hat{B}|0\rangle. \end{aligned} \quad (2.53)$$

On the other hand, an expression for the real part of Eq. (2.50) can be achieved once the imaginary part is obtained. According to the Plemelj-Dirac formula and the sifting property of the Dirac delta function we find that:

$$\begin{aligned} \text{Re}\langle\hat{A};\hat{B}\rangle &= -\frac{1}{\pi} \mathcal{P} \int_{-1}^1 \frac{\text{Im}\langle\hat{A};\hat{B}\rangle}{\omega - \omega'} d\omega' \\ &= -2 \sum_{n=1}^{\infty} a_n U_{n-1}(\omega), \end{aligned} \quad (2.54)$$

where the expansion in Eq. (2.52) and the Hilbert transform of Eq. (2.47) have been used. Mixing the expanded real and imaginary parts we obtain the full correlation function in terms of Chebyshev polynomials [104]:

$$\langle\hat{A};\hat{B}\rangle^\omega = \frac{-i}{\sqrt{1-\omega^2}} \left[a_0 - 2 \sum_{n=1}^{\infty} a_n \exp(-i \arccos \omega) \right]. \quad (2.55)$$

This expansion of the dynamical correlation function can be used for the calculation of the different components of the full Green-Gor'kov functions. Replacing $\hat{A} = c_{i\uparrow}$ and $\hat{B} = c_{j\uparrow}^\dagger$ we have that normal Green function in Eq. (2.40) is expanded by the series of Eq. (2.55) where the moments are given according to the following expecting values:

$$a_n^{11} = \langle c_{i\uparrow} | T_n(\mathcal{H}) | c_{j\uparrow}^\dagger \rangle. \quad (2.56)$$

Likewise, the anomalous Gor'kov-Green function can be reconstructed from the moments:

$$a_n^{12} = \langle c_{i\downarrow}^\dagger | T_n(\mathcal{H}) | c_{j\uparrow}^\dagger \rangle^*. \quad (2.57)$$

2.3.3 Implementation details

Moments can be calculated by using Eqs. (2.56) and (2.57) once the Hamiltonian is rescaled such that the energy spectrum lies in the interval $[-1, 1]$. We therefore have to normalize the Hamiltonian and all energy arguments through the following linear transformations:

$$\tilde{\mathcal{H}} = \frac{\mathcal{H} - b\mathcal{I}}{a}, \quad \tilde{E} = \frac{E - b}{a}, \quad (2.58)$$

where the rescaling parameters are given by the maximum and minimum eigenvalues of the Hamiltonian according to:

$$a = \frac{E_{\max} - E_{\min}}{2 - \epsilon}, \quad b = \frac{E_{\max} + E_{\min}}{2}. \quad (2.59)$$

The E_{\max} and E_{\min} bounds of the spectrum could be obtained analytically or estimated numerically through a Lanczos method since the accuracy is not essential. Furthermore, whether the rescaled energies include or exceed the edges of the interval $[-1, 1]$ a small cut-off parameter ϵ is introduced in order to avoid instabilities.

Once the Hamiltonian and its eigenvalues are properly rescaled, we proceed to the calculation of the states $|j_n\rangle = T_n(\mathcal{H})|c_{j\uparrow}^\dagger\rangle$ in order to evaluate the expectation values of Eqs. (2.56) and (2.57). This can be performed by successive applications of the Hamiltonian, according to the recursive relations between the Chebyshev polynomials of Eqs. (2.45):

$$\begin{aligned} |j_n\rangle &= [2\mathcal{H}T_{n-1}(\mathcal{H}) - T_{n-2}(\mathcal{H})] |c_{j\uparrow}^\dagger\rangle \\ &= 2\mathcal{H}|j_{n-1}\rangle - |j_{n-2}\rangle, \end{aligned} \quad (2.60)$$

with the first two elements of the expansion given by $|j_0\rangle = T_0(\mathcal{H})|c_{j\uparrow}^\dagger\rangle = |c_{j\uparrow}^\dagger\rangle$ and $|j_1\rangle = T_1(\mathcal{H})|c_{j\uparrow}^\dagger\rangle = \mathcal{H}|c_{j\uparrow}^\dagger\rangle$. Note that the calculation of these recursive

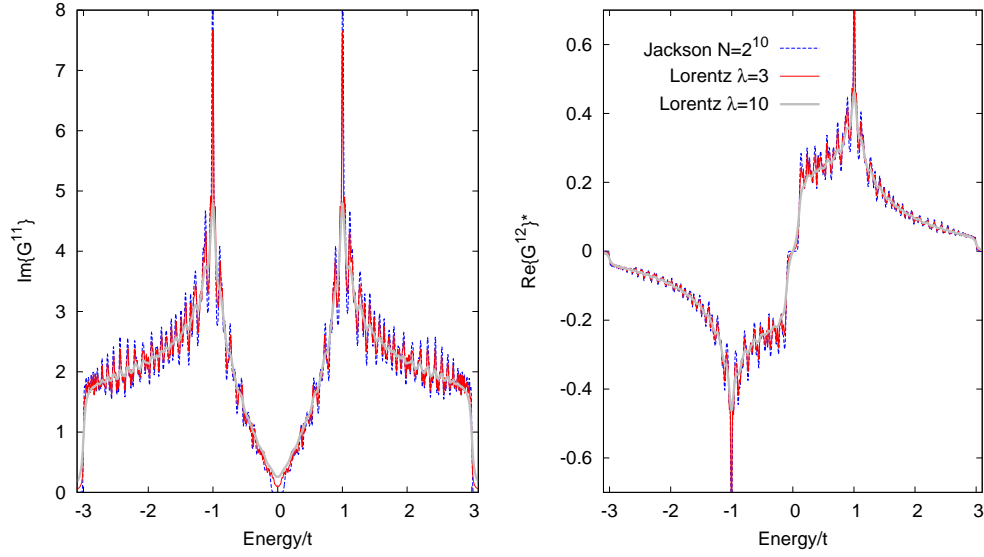


Figure 2.4: Chebyshev expansion of the (left) imaginary part of the normal Green function and (right) real part of the anomalous Green function with $N = 1024$ expansion coefficients based on different kernels functions.

states are at the core of the Chebyshev expansion method. Moments are finally obtained from iterative states from internal products $a_n^{11}(i, j) = \langle c_{i\uparrow} | j_n \rangle$ and $a_n^{12}(i, j) = \langle c_{i\downarrow}^\dagger | j_n \rangle$ for the normal and anomalous Gor'kov-Green functions respectively.

However, a real numerical implementation of this method requires that the summation in Eq. (2.55) must be truncated at some finite order N . Keeping a finite number N in the series (2.55) of terms might introduce some imprecisions in the approximation and fluctuations around discontinuity points of the integrable function. These fluctuations, named Gibbs oscillations, in fact increase with the frequency or equivalently with the order of the expansion N . To avoid them, a commonly used method consists in the introduction of a damping factor which transform the expansion coefficients, $\mu_n \rightarrow g_n \mu_n$. In a more strictly sense, this corresponds to the convolution of the expanded function $f(x)$ with a kernel function $K_N(x, y)$ mapped into a function, f_{KPM} , such that in the limit when $N \rightarrow \infty$ we have the absolute difference $\|f - f_{\text{KPM}}\| \rightarrow 0$. The problem is then reduced to the finding of the optimal kernel function $K(x, y)$, *i.e.*, the damping factors g_n . A summary of different integral kernels can be found in the literature related to the Chebyshev expansion method [104]. For most of the practical applications an optimal kernel corresponds to the Jackson kernel $K_N^J(x, y)$ where the

damping factors are the following:

$$g_n^J = \frac{(N - n + 1) \cos(\pi n / (N + 1)) + \sin(\pi n / (N + 1)) \cot(\pi / (N + 1))}{N + 1}. \quad (2.61)$$

One way to quantify the error of this approximation is obtained by mapping the delta function into δ_{KPM} with $K_N^J(x, y)$. It can be demonstrated that δ_{KPM} can be approximate by a Gaussian function of width $\sigma = \pi/N$, where N is the order of the expansion. Recalling the Plemelj-Dirac relation, one can realize a different approximation for the delta function which is given in terms of the Lorentz function:

$$\delta(x) = -\frac{1}{\pi} \lim_{\eta \rightarrow 0} \text{Im} \frac{1}{x + i\eta} = \lim_{\eta \rightarrow 0} \frac{\eta}{\pi(x^2 + \eta^2)}. \quad (2.62)$$

This introduce us to an alternative kernel, K_N^L , called Lorentz kernel which is more appropriated for the expansion of Gor'kov-Green function since the features of Eq. (2.62) are perfectly mimicked by the divergences at energies close to the true eigenvalues of the Hamiltonian. The damping factors defined by the Lorentz kernel have the following form:

$$g_n^J = \frac{\sinh[\lambda(1 - n/N)]}{\sinh(\lambda)}, \quad (2.63)$$

where the free parameter λ allows us to control the resolution of the approximation since the broadening of the Lorentzian depends on this parameter according to $\epsilon = \lambda/N$.

The expansion of the imaginary and real component of normal and anomalous Green function in Fig. 2.4 allows us to make a direct comparison between the convergence of Jackson and Lorentz kernels. Under the same order N of expansion we observed the strong presence of Gibbs oscillation and finite size effect in the Jackson kernel compared to Lorentz where smooth convergence can be achieved by adjusting the λ factor. While the Lorentz kernel is the best option for the approximation of the LDOS obtained from Eq. (2.37), the smoothness induced by the λ factor may introduce errors in the calculation of the order parameter through the integral of Eq. (2.42).

2.3.4 Complex absorbing potential

Conventional calculations of the real space electronic structure in solids use open or periodic boundary conditions with a finite computational unit cell. While

infinite dimensions are emulated through periodic boundary conditions, open boundary conditions give rise to non-desired edges or surface states. Inconvenient for the calculation of bulk states, open boundary conditions lead to large dimension systems in order to buffer interference coming from the edge. Periodic boundary conditions are more suitable for bulk characteristics of the system, where size dependence of the calculation are related to the number of momentum values needed to achieve convergence. It is a common issue found in quantum reactive scattering calculations where non-realistic reflections of a wave packet from the finite grid should be avoided. An alternative to these conventional boundary conditions is the implementation of an arbitrary absorbing potential. This procedure has been optimized and applied and have shown a very low reflection probability when using small unit cells [113–117]. Following Ref. [114] we consider an absorbing potential operator $\hat{\Gamma}$ such that the normal Hamiltonian is redefined according to:

$$\hat{H} \rightarrow \hat{H} + \hat{\Gamma}$$

where a proper choice requires $\text{Im}\hat{\Gamma}$ to be negative and $\text{Re}\hat{\Gamma} = 0$. It is expected that a well-behaved absorbing potential eliminates the so-called reflection effects effectively mimicking an infinite region. It has been shown that absorbing boundary conditions could be incorporated easily in the Chebyshev expansion of the Green functions [113] by considering an operator sequence $\hat{Q}_n(\hat{H}, \gamma)$ which satisfies the following recursion formula:

$$\hat{Q}_{n+1} = e^{-\hat{\gamma}}(2\hat{H}_n\hat{Q}_n - e^{-\hat{\gamma}}\hat{Q}_{n-1}), \quad (2.64)$$

with the initial conditions $\hat{Q}_0 = I$ and $\hat{Q}_1 = e^{-\hat{\gamma}}\hat{H}$ and where $e^{-\hat{\gamma}}$ is a damping factor with spatial-dependent operator phase $\hat{\gamma}(\vec{r})$. Latter recursive procedure corresponds to a more general case than represented in Eq. (2.60) where the Chebyshev expansion of the Green function in terms of the \hat{Q}_n operator is written as follows:

$$\hat{G} = \frac{1}{i} \sum_{n=0} (2 - \delta_{n0}) e^{-in\phi} \hat{Q}_n(\hat{H}, \hat{\gamma}) \times [\sin(\phi - i\hat{\gamma})]^{-1}, \quad (2.65)$$

where $\phi = \arccos(\tilde{\omega})$ being $\tilde{\omega}$ the normalized eigenvalues of \hat{H} . The relation between the absorbing potential $\hat{\Gamma}$ and the dimensionless damping potential $\hat{\gamma}$ is given by [114]:

$$\hat{\Gamma} = a [\cos \phi (1 - \cosh \hat{\gamma}) - i \sin \phi \sinh \hat{\gamma}], \quad (2.66)$$

where a is the scale parameter from Eq. (2.58). If $\hat{\gamma}$ does not depend on the energy, which makes the operators $\hat{Q}_n(\hat{H}, \hat{\gamma})$ energy independent and which is the most practical choice, the optical potential $\hat{\Gamma}$ will be a function of the energy

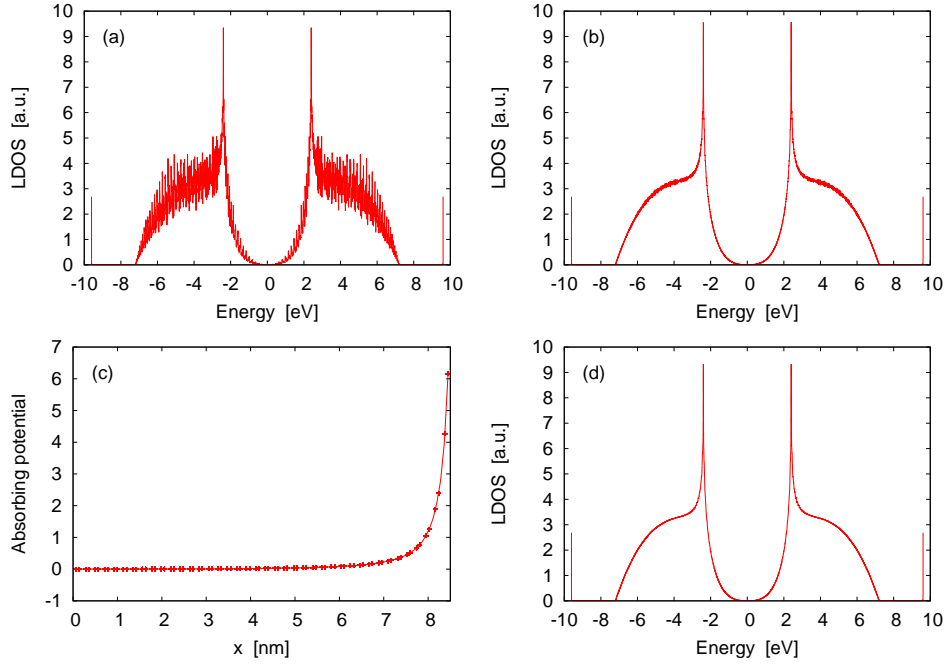


Figure 2.5: LDOS at one of the edges for graphene nanoribbon with width (a) $W = 8.52\text{nm}$ and (b) $W = 85.2\text{nm}$. (c) Profile of the absorbing potential described by Eq. (2.71), (d) LDOS at $x = 0$ for a graphene nanoribbon with width $W = 8.52\text{nm}$ with the absorbing potential given in (c).

ω [114].

It is easy to demonstrated that under normal conditions, *i.e.* for $\hat{\Gamma} = 0$, the Chebyshev expansion of the Green function is:

$$\hat{G} = \frac{1}{i} \sum_{n=0} (2 - \delta_{n0}) e^{-in\phi} \hat{T}_n(\hat{H}) \times [\sin \phi]^{-1}, \quad (2.67)$$

where according to the definition of ϕ the factor $\sin \phi = (1 - \tilde{\omega}^2)^{1/2}$ corresponds to the weight function for the Chebyshev polynomials . Note that this factor becomes imaginary when the complex potential is taken into account and therefore an imaginary phase is introduced by the argument of the damping factor:

$$\sin(\phi - i\hat{\gamma}) = (1 - \tilde{\omega}^2)^{1/2} \cosh \hat{\gamma} - i\tilde{\omega} \sinh \hat{\gamma}. \quad (2.68)$$

Nevertheless, by performing calculations only over the region where the complex potential, as well as the damping potential vanishes, this factor reduces effectively to the usual weight function of the Chebyshev polynomials in Eq. (2.67).

On the other hand, under the assumption that $\hat{\Gamma}$ is a pure negative imaginary operator, we can deduce from a given absorbing potential, $\hat{\Gamma} = -iV(x)$, with $V(x)$ being real, the following approximated x -dependence for the $\hat{\gamma}$ operator using the relation (2.66):

$$\hat{\gamma} = \sinh^{-1}(\tilde{V}(x)). \quad (2.69)$$

A typical procedure consists in assuming a functional form for the absorbing potential $-iV(x)$ and then adjust its parameters in order to optimize the absorption [116].

A trivial example but not the most optimal form of the function $V(x)$, is the simple linear absorbing potential [118]. Other more complicated forms for the absorbing potential have been proposed, some of which have a second-order singularity at the end of the absorbing regions, with exactly transmission free [115, 117].

An example of these functions correspond to the following relation suggested by Kosloff *et al.* [119]:

$$\hat{\Gamma}(x) = -iV(x) = \frac{-iV}{\cosh^2[(x - x_1)/\alpha]}, \quad (2.70)$$

where x_1 is the end of the absorbing region and the parameter α is a decay factor. In a more recent calculation of the electrical transport a complex absorption potential was added to the Hamiltonian of a semi-infinite lead. By solving analytically for the respective a Schrödinger equation the following potential was deduced [115]:

$$\hat{\Gamma}(x) = -iV(x) = -i \frac{\hbar^2}{2m} \left(\frac{2\pi}{\Delta x} \right)^2 f(y), \quad (2.71)$$

where m is the electron mass and $\Delta x = x_2 - x_1$ is the absorbing region, $c = 2.62$ is a constant and

$$f(y) = \frac{4}{(c - y)^2} + \frac{4}{(c + y)^2} - \frac{8}{c^2}, \quad y = \frac{c(x - x_1)}{\Delta x}. \quad (2.72)$$

Following we show some results for the surface local density of states (LDOS) for a graphene nanoribbon of width W considering an absorbing potential along the axis parallel to the width direction with spatial dependence given by Eq. (2.71). Calculations are performed by using Eq. (2.37) where the normal Gor'kov-Green function is obtained from Eq. (2.67). Since, we are including the absorbing potential, expansion moments are calculated by using the recursive relations given by Eq. (2.64). As observed in Fig. 2.5(a) for a graphene nanoribbon with

$W = 8.52\text{nm}$, LDOS at one of the edges shows a series of peaks which correspond to the appearance of sub-bands. The same plot for a wider graphene nanoribbon with $W = 85.2\text{nm}$ shows that these peaks tend to disappear as long as the edge states are more separated (see Fig. 2.5(b)). Surprisingly, the effect of a wider graphene nanoribbon can be achieved with a shorter width by including an absorbing potential at the opposite edge in the way that is shown in Fig. 2.5(c). We see that sub-bands peaks disappear as the absorbing potential at one edge emulate effectively a semi-infinite lead.

2.4 GPU computing

The most demanding computing effort of Chebyshev-Bogoliubov-de Gennes method relies on the iterative relation needed for the recursive calculation of the moments. As it can be observe from Eq. (2.60), this iterative procedure mainly involves successive multiplication of Hamiltonian matrix, defined from Eq. 2.34, with the iterative vectors. Most of the entries in the BdG matrix Hamiltonian are zero and therefore this can considered as a sparse matrix. The sparsity nature of this matrices allows us to exploit the fine-grained parallelism in sparse matrix-vector multiplication (SpMV). Realizing this potential, SpMV computation is optimized by using hardware multithreading where sparse algebra is executed in parallel through thousands or tens of thousands of threads. This throughput optimization is expected to provide abundant parallelism different from the latency-oriented CPU processors where the computing architecture is aimed at improving transistor performance in order to minimize the running time of sequential tasks. A example of throughput-oriented many-core processors are the graphic processors units (GPUs). The high-performance computing of GPUs takes advantage of a large number of execution threads, sacrificing the single-thread execution speed, in order to increase the total amount of work completed for by the threads in a unit of time. It has been demonstrated that SpMV computation can be successfully mapped onto the fine-grained parallel architecture employed by the GPU [120]. In Fig. 2.6 we shown a comparison between the performance of SpMV operations executed both in a GTX460 Nvidia GPU and an Intel Pentium CPU. In this case, calculation is performed by 16384 iterations for a graphene grid of size $N \times N$. As we can observe in Fig. 2.6, the execution time increases dramatically with the size of the grid by performing the iterative calculation using CPU. On the contrary, performance on GPU gets better as size of the grid is increased, showing that a high speed-up can be achieved by implementing parallel computation on GPU.

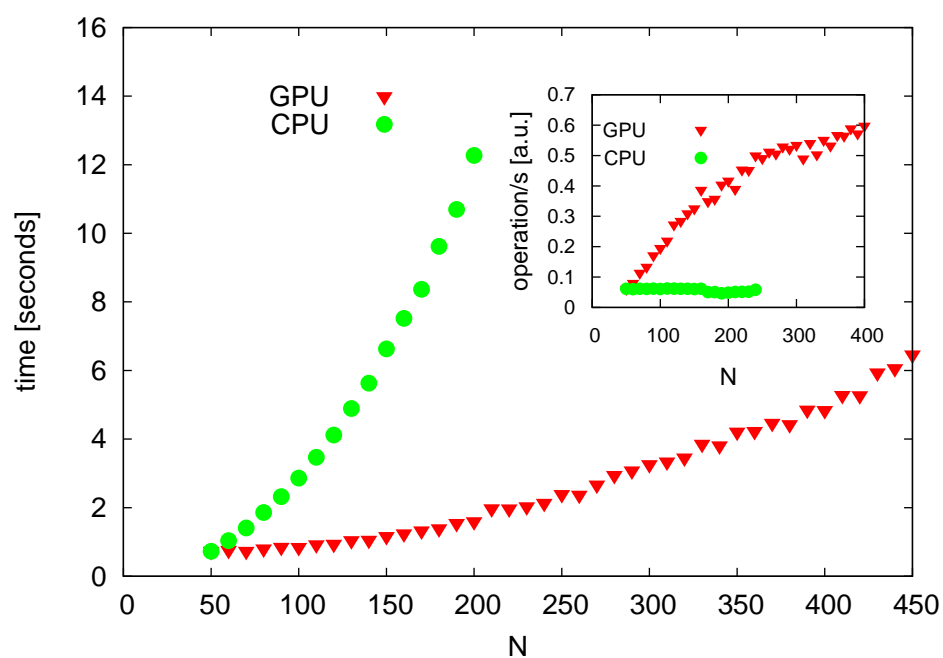


Figure 2.6: GPU vs. CPU performance for Chebyshev iterative calculation of the moments for different graphene grids of size $N \times N$.

3

Tight-binding study of bilayer graphene Josephson junctions

In this chapter, we solve self-consistently for the pair correlation and the Josephson current in a superconducting-bilayer graphene-superconducting Josephson junction by using highly efficient simulations of the tight-binding Bogoliubov-de Gennes model. Different doping levels for the non-superconducting link are considered in the short and long junction regime. Self-consistent results for the pair correlation and superconducting current resemble those reported previously for single layer graphene [121] except at the Dirac point where remarkable differences in the proximity effect are found as well as a suppression of the superconducting current in the long junction regime. Inversion symmetry is broken by considering a potential difference between the layers and we found that the supercurrent can be switched if the junction length is larger than the Fermi length.

3.1 Introduction

When in contact to superconductors, graphene exhibits exotic superconducting properties. Although graphene was not found to sustain intrinsic superconductivity itself, there is experimental evidence [58, 63, 64, 122, 123] that when in proximity with a conventional superconductor it becomes superconducting. Because of the conventional superconducting proximity effect, which describes

how Cooper pairs diffuse from the superconducting material into metals, superconducting hybrid structures like superconducting-normal-superconducting (SNS) Josephson junctions are interesting systems in which one can study electronic correlation of relativistic-like particles. In the ballistic regime, which is realizable in SNS graphene Josephson junctions according to recent experiments [62, 63], theoretical studies have shown the existence of a finite bipolar superconducting current through the junction [59, 121, 124–126]. With a gapless parabolic, instead of linear, band structure, bilayer graphene (BLG) appears at this point as a suitable alternative for investigating electronic correlations in two dimensional systems. Also, as it is widely known theoretically and experimentally, a tunable gap can be induced in BLG by an out-of-plane applied electric field, which is very useful for transistor applications [9, 81]. We expect that the role of the gapless parabolic dispersion may be important since the superconducting correlations depend strongly on the electronic properties of the material. Moreover, the ability to open a gap in the spectrum by an external electric field could be of interest in superconducting devices. Within a tight-binding Bogoliubov-de Gennes formalism we calculate self-consistently the pair correlation and the Josephson current through a Superconducting-BLG-Superconducting Josephson junction.

3.2 Model System

We study the Josephson effect in a BLG-based junction by considering the hybrid nano-structure illustrated in Fig. 3.1. We consider a bilayer graphene in the common AB (Bernal) stacking as it was described in Sub-section 2.1.3. The top and bottom layers are both in contact with superconducting leads while a junction of size L is suspended. The influence of the superconducting contacts is modeled by assuming an on-site attractive pairing potential, $U_S < 0$ and heavy doping, $\mu_S > 0$ in the contact regions, which are labeled by S , such that a s-wave superconducting state is induced in the outermost regions of both layers. The normal region labeled by N , which has a tunable Fermi level μ_N and zero pairing potential, $U_N = 0$, acts like a non-superconducting channel through which Cooper pairs could tunnel. Similar models for graphene based Josephson junctions were previously considered in the Dirac limit [59, 124–126] as well as in the tight-binding formulation [121, 127, 128]. We solve self-consistently for the order parameter along the junction following closely the self-consistent calculation performed in Ref. [121] for a ballistic single-layer graphene Josephson junction. This is necessary in order to consider the possibility of Cooper pairs being depleted close to the interface in the superconducting region due to the existence of the normal region, i.e. the inverse proximity effect. As is usually

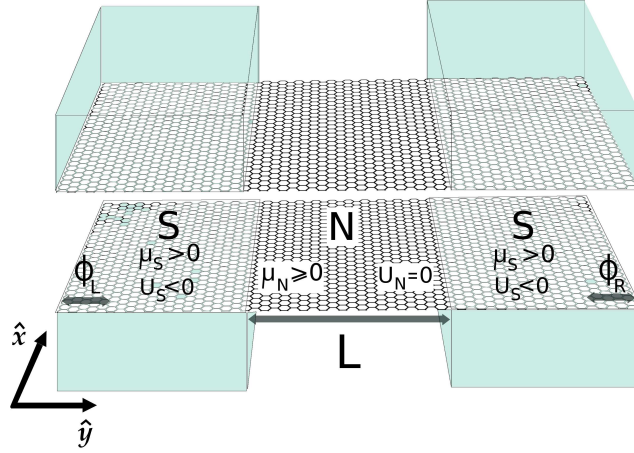


Figure 3.1: Layout of the SNS-BLG Josephson junction where the superconducting leads are modeled by assuming on-site attractive pairing potential U_S and a heavy doping μ_S in the regions under the contacts labeled by S. For the non-superconducting link, with length L and labeled by N, we took the pairing potential $U_N = 0$ and a varying chemical potential μ_N . Phases ϕ_L and ϕ_R are kept fixed during the self-consistent calculation.

assumed for SLG-based junctions we consider a clean and smooth interface such that all physical quantities are homogeneous along the \hat{x} -direction parallel to the interface. In addition, we have considered a wide junction, with width $W \gg L$, as well as periodic boundary conditions imposed along the \hat{y} -direction. The latter assumptions make it possible to reduce the self-consistent calculation of the order parameter from a two-dimensional problem to a one-dimensional one since we can restrict the calculation to only a unit cell along the \hat{y} -direction perpendicular to the interface. It is worth mentioning that the pairing potential does not distinguish between the sublattices defined on either layer. However, due to the interlayer coupling, the self-consistent calculation should be performed separately for only two inequivalent sites A and B (or \tilde{A} and \tilde{B}) within the unit cell. The breaking of the inversion symmetry, which is easily achieved by considering a potential difference applied between the layers, makes it necessary to perform the self-consistent calculation for all four sub-lattice types within the unit cell.

In order to describe the DC Josephson effect we fix the difference in the phases of the order parameter, $\Delta\phi^S = \phi_R - \phi_L$, in the outermost parts of the S regions (see Fig. 3.1). In a finite region near the interfaces, with size of the order of the coherence length, the order parameter is allowed to relax self-consistently. Therefore the phase gradient over the non-superconducting region $\Delta\phi^N$ will be restricted according to $\Delta\phi^N \leq \Delta\phi^S \leq \pi$, considering that the maximum value

of $\Delta\phi^S$ is π . This constraint for $\Delta\phi^N$ was recently pointed out by Black-Shaffer *et al.* [121] in a SLG-based ballistic junction.

3.3 Numerical Method: Chebyshev expansion of the Green's function

Superconducting correlations are described by using the tight-binding Hamiltonian with on-site attractive Hubbard interactions (2.30). Write in a convenient form for BLG-based Josephson junction it has the following form:

$$\begin{aligned} \mathcal{H} = & - \sum_{\langle i,j \rangle \sigma} t \left(c_{i\sigma}^\dagger c_{j\sigma} + \tilde{c}_{i\sigma}^\dagger \tilde{c}_{j\sigma} \right) - t_\perp c_{i\sigma}^\dagger \tilde{c}_{j\sigma} \\ & - \sum_{i\sigma} (\mu_i + \epsilon_1) c_{i\sigma}^\dagger c_{i\sigma} + (\mu_i + \epsilon_2) \tilde{c}_{i\sigma}^\dagger \tilde{c}_{i\sigma} \\ & + \sum_i U_i \left(c_{i\uparrow}^\dagger c_{i\uparrow} c_{i\downarrow}^\dagger c_{i\downarrow} + \tilde{c}_{i\uparrow}^\dagger \tilde{c}_{i\uparrow} \tilde{c}_{i\downarrow}^\dagger \tilde{c}_{i\downarrow} \right), \end{aligned} \quad (3.1)$$

where $\tilde{c}_{i\uparrow}^\dagger |\text{vac}\rangle$ creates a spin-up electron on the i -site in the top layer whereas $c_{j\downarrow} |\text{vac}\rangle$ creates a spin-down hole on the j -site in the bottom layer. The hopping parameter, t , describes the intra-layer hopping integral between next-nearest neighbors in the same layers while $t_\perp = 0.143t$ correspond to the interlayer nearest-neighbors hopping which couples the dimer sites \tilde{A} and B . Other hopping terms, like the interlayer coupling between the non-dimer \tilde{B} and A sites, are not considered in the present work, since they influence only very low-energy excitations. The Fermi level is shifted from the charge neutrality point or Dirac point by the chemical potential μ_i and U_i is the on-site attractive pairing potential which is non vanishing only in the right and left superconducting regions. The on-site energies ϵ_1 and ϵ_2 for atomic sites on the top and bottom layer, respectively, have been introduced in order to simulate a potential difference or gate voltage $V_g = \epsilon_1 - \epsilon_2$ between the layers.

By using the Hartree-Fock decomposition and keeping only terms relevant to the superconducting order, one can transform the many-body Hamiltonian (3.1) into a mean-field single-particle Hamiltonian, which within the Nambu formalism can be written as follows:

$$\mathcal{H} = \sum_{\langle i,j \rangle} \left(c_{i\uparrow}^\dagger \tilde{c}_{i\uparrow}^\dagger c_{i\downarrow} \tilde{c}_{i\downarrow} \right) \begin{pmatrix} \hat{\mathcal{H}}_0 & \hat{\Delta} \\ \hat{\Delta}^\dagger & -\hat{\mathcal{H}}_0^\dagger \end{pmatrix} \begin{pmatrix} c_{i\uparrow} \\ \tilde{c}_{i\uparrow} \\ c_{i\downarrow}^\dagger \\ \tilde{c}_{i\downarrow}^\dagger \end{pmatrix}, \quad (3.2)$$

where $\hat{\mathcal{H}}_0$ and $\hat{\Delta}$ are the following 2×2 matrices:

$$\hat{\mathcal{H}}_0 = \begin{pmatrix} \epsilon_1 + \mu_i & 0 \\ 0 & \epsilon_2 + \mu_i \end{pmatrix} (-\delta_{ij}) - \begin{pmatrix} t & t_\perp \\ t_\perp^* & t^* \end{pmatrix} (1 - \delta_{ij}), \quad (3.3)$$

$$\hat{\Delta} = \begin{pmatrix} \Delta_i & 0 \\ 0 & \tilde{\Delta}_i \end{pmatrix} \delta_{ij}, \quad (3.4)$$

where the diagonal elements of the matrix (3.4) correspond to the on-site mean-field superconducting order parameter $\Delta_i = U_i \langle c_{i\uparrow} c_{i\downarrow} \rangle$.

Following methodology shown in Section 2.3 we have performed the self-consistent mean-field calculation through a numerical approximation of the Gorkov Green's function by using the Chebyshev-Bogoliubov-de-Gennes method. Both, the normal and anomalous Gorkov Green's function, can be approximated by a superposition of a finite number of Chebyshev polynomials as follows:

$$G_{ij}^{1\alpha}(\tilde{\omega}) = \frac{-2i}{\sqrt{1 - \tilde{\omega}^2}} \left[\sum_{n=0}^N a_n^{1\alpha}(i, j) e^{-in \arccos(\tilde{\omega})} \right], \quad (3.5)$$

where the expansion coefficients for the diagonal, or normal ($\alpha = 1$), and the off-diagonal, or anomalous ($\alpha = 2$), components of the 2×2 Green function are defined respectively as [111]:

$$a_{ij}^{11}(\omega) = \langle c_{i\uparrow} | T_n(\mathcal{H}) | c_{j\uparrow}^\dagger \rangle, \quad (3.6)$$

$$a_{ij}^{12}(\omega) = \langle c_{i\downarrow}^\dagger | T_n(\mathcal{H}) | c_{j\uparrow}^\dagger \rangle^*, \quad (3.7)$$

where $T_n(x) = \arccos(n \cos(x))$ is the Chebyshev polynomial of order n .

Physical quantities, like the local density of states, the pair correlation function and the Josephson current, can be easily determined once the Green's functions are known:

$$N_i(\omega) = -\frac{2}{\pi} \text{Im} G_{ii}^{11}(\omega), \quad (3.8)$$

$$\langle c_{i\uparrow} c_{i\downarrow} \rangle = \frac{i}{2\pi} \int_{-E_c}^{E_c} G_{ii}^{12}(\omega) (1 - 2f(\omega)) d\omega, \quad (3.9)$$

and

$$J_{ij} = -\frac{1}{\pi} \int [it_{ij} G_{ij}^{11}(\omega) - it_{ij}^* G_{ij}^{11*}(\omega)] f(\omega) d\omega, \quad (3.10)$$

respectively [111]. Since most of the computational effort corresponds to sparse matrix-vector and vector-vector multiplication, high speed-up can be achieved by implementing parallel computation on graphical processing units (GPUs). We are therefore able to solve efficiently systems described by matrices of sizes $2N \times 2N$, where N is the number total of lattice sites which lies between 44×10^3 and 160×10^3 atoms according to the junction size considered in this study. Note that for system size of this order the direct diagonalization of the Hamiltonian matrix is not possible. Additional parallel computations can be implemented by considering that all physically quantities calculated here, such as density of states, pair correlation or the Josephson current, can be obtained from the Green's function for each lattice point separately.

3.4 Results

It is well-known that the energy dispersion in SLG and BLG differ around the neutrality point. Therefore, qualitative differences are expected in the proximity effect as well as in the Josephson current in the two systems. For a quantitative comparison between SLG and BLG Josephson junction we have set up the following values for the physical input parameters: $U_S = -1.36t = -3.4\text{eV}$ and $\mu_S = 0.6t = 1.5\text{eV}$, similar to the values used in a previous self-consistent study for ballistic SLG Josephson junctions [121]. These parameters lead to a finite s-wave bulk superconducting order parameter, $\Delta_0 = 0.041t$, which corresponds to a superconducting coherence length $\xi = \hbar v_F / \Delta_0 \approx 33a$, where a is the C-C inter-atomic distance, similar to the one considered in the SLG junction case. Due to the difference in the local density of states between dimer and non-dimer locations, the order parameter is slightly different for these two types of atoms. Both junction length regimes are solved with the proposed self-consistent numerical method, e.g. short junction for $L < \xi$ and long junction for $L > \xi$. For both cases the width of the samples has been chosen as the minimal value of the ratio L/W for which no important variations of the pair correlation are observed when increasing the width of the junction. For short and long junction it was found that $L/W = 0.05, 0.1$, respectively, were necessary in order to avoid a relevant width dependence of the results.

Previous analytical descriptions of BLG Josephson junctions based on the Dirac equation [125, 129] requires smooth interfaces and a low energy regime, for which $\Delta_0 \ll t_\perp \ll \mu_S$. Here these restrictions are lifted but in order to compare with relevant experimental scenarios we performed calculations only for situations corresponding to $\Delta_0 < t_\perp < \mu_S$.

3.4.1 Proximity effect

We show in Fig. 3.2 the self-consistently calculated pair correlation $\langle c_{i\uparrow}c_{i\downarrow} \rangle$ for both inequivalent sites, A (dimer) and B (non-dimer), in a unit cell defined along the \hat{y} -direction perpendicular to the interface. As was previously mentioned, both long and short junctions are considered here and plotted in Figs. 3.2(a) and 3.2(b), respectively. We present the pair correlation function for several doping levels in the non-superconducting region showing that the proximity effect is strongly dependent on the relative Fermi level mismatch (FLM) between the S and N regions. A significant difference between BLG and SLG can be seen for the undoped case ($\mu_N = 0$) while for other dopings the pair correlation exhibits similar behavior in BLG and SLG. In particular, we can see that in the undoped case dimer sites in BLG show a suppression of the pair correlation over the N region compared to the SLG case. Opposite behavior is seen for non-dimer sites where a larger pair leakage into N is found. This behavior is similar to the proximity effect in strained graphene where a sublattice polarization of the local density of states in the zeroth pseudo-Landau level induces sub-lattice dependent leaking distances [128]. No relevant differences in the pair correlation profile are found between dimer and non-dimer sites in BLG for the higher doping levels considered here: moderately doped $\mu_N = 0.3t$ and highly doped $\mu_N = 0.6t$. Note also in Fig. 3.2(b) that the reported interlayer asymmetry in the pair correlation in BLG is found to be not important for the short junction regime. In fact, we can clearly see in Fig. 3.2(c) that the difference between the pair correlation at sites A and B becomes larger as the junction length is increased, as large as a few orders of magnitude.

3.4.2 LDOS

To further understand this peculiar behavior observed only in the undoped case we plot the local density of states (LDOS) in the superconducting and non-superconducting regions. The LDOS is plotted for dimer (A) and non-dimer (B) lattice sites across the junction in the long junction limit where we have previously found differences in the proximity effect between SLG and BLG Josephson junctions. Three particular cases have been chosen and shown in the top panels of Fig. 3.3. Panel (a) shows the LDOS for two sites in the middle of the N region for the undoped case, whereas, in panel Fig. 3.3(b) we have depicted the LDOS for the same locations but when there is no-FLM, i.e. the doping is the same throughout the graphene layer. Results shown in Fig. 3.3(a)-(b) are consistent with the fact that the density of states at dimer sites vanishes linearly around the Dirac point, while being finite at the non-dimer sites [9, 89], as this can be clearly seen in the inset of Fig. 3.3(b). Due to the differences in the LDOS for inequiv-

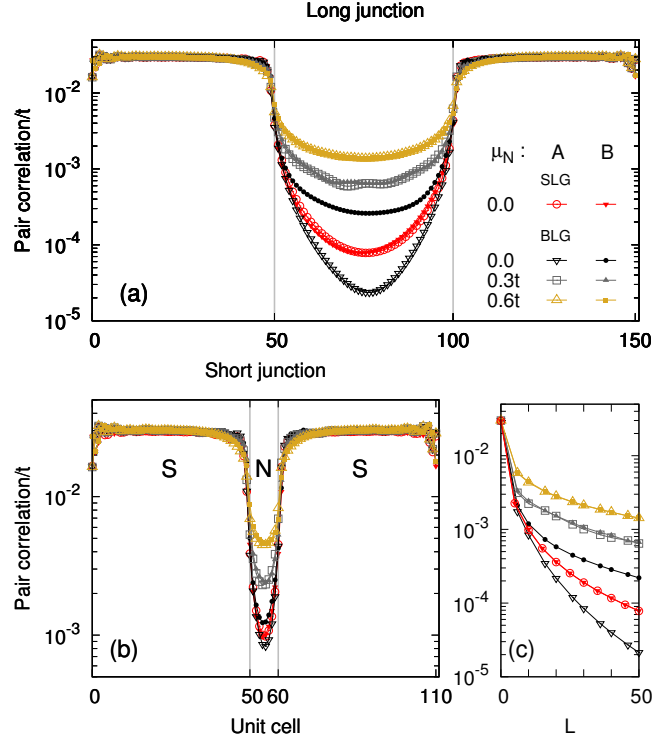


Figure 3.2: Absolute value of the pair correlation in a long (a) and short (b) BLG Josephson junction as a function of the position along the \hat{y} -direction perpendicular to the SN interface. Each unit cell has a length equal to $3a/2$ where a is the in-plane interatomic distance. Both inequivalent sites, dimer at A and non-dimer at B, are plotted separately for different doping levels considered for the non-superconducting region: $\mu_N = 0, 0.3t$ and $0.6t$. The first one corresponds to the case when the Fermi level is pinned at the Dirac point while the last one corresponds to no-FLM at the interface. (c) Pair correlation at $L/2$ in the N region as a function of the junction length L for different values of μ_N . SLG self-consistent results are shown for comparison with the BLG undoped case.

alent sites in BLG, the proximity effect will give different leaking distances in different sub-lattices, as we show in Fig. 3.2(c) for the undoped case. In fact, the inset of Fig. 3.3(d) shows a better appreciation of the LDOS of Fig. 3.3(d) around the Dirac point where we notice the formation of Andreev states for a non-dimer site in the middle of the undoped N region. For the cases of dimer sites and for SLG, where we have a vanishing density of states at the Dirac point,

we find that the Andreev peaks are strongly suppressed. In addition, we show in Fig. 3.3(d) the energy gap at the interface where the coherence peaks are more pronounced at the non-dimer sites in comparison to the dimer sites and the SLG junction.

Increasing the doping level in the normal region makes the LDOS more homogeneous. This result is consistent with the fact that no difference between both kind of sites is observed for the other doped cases in the pair correlation function shown in the previous section. Finally, Fig. 3.3(c) shows the LDOS deep inside the superconducting region where we can clearly see the coherence peaks on each side of the superconducting gap. Note that the LDOS becomes homogeneous in both sublattices and resembles the one of SLG one for the highly doped case, and no difference is observed in the superconducting gap even in the zoomed-in view shown in Fig. 3.3(e) for the N and S region.

3.4.3 Josephson current

3.4.3.1 Unbiased case

In the absence of applied bias voltage but in the presence of a finite phase difference between the two superconducting sides, a DC supercurrent will flow across the junction [121, 130]. This is the usual DC Josephson effect. For this purpose a phase bias is achieved by fixing a desired phase difference between the outermost parts of the superconducting regions, ϕ_L and ϕ_R for the left and right sides of the junction respectively (see Fig. 3.1). In order to numerically calculate the Josephson current we solve self-consistently for both phase and amplitude of the order parameter along the junction except in the extreme regions where we keep the phases fixed. The current profile along the junctions in both layers as well as the interlayer current are shown in Figs. 3.4(a)-(d) for an undoped non-superconducting link for different values of the pairing potential. As we can see, the supercurrent is found not to be constant within each layer separately, contrary to what is usually expected to happen for self-consistent current calculation in 2-dimensional systems [130]. Instead, one interesting feature in BLG is the appearance of a weak interlayer current between \tilde{A} - B dimer sites as a consequence of the current conservation law. We observe that the LDOS at the left interface is asymmetric in top-bottom layers while for the right interface the asymmetry is reversed. Because of this, the current is enhanced at the left interface in the top layer while being suppressed in the bottom layer, therefore a weak interlayer current appears. The reverse happens at the right interface, but the average current remains flat across the whole junction, as expected. Next we construct the current-phase relation (CPR) by performing self-consistent current calculations for different phase differences between the superconducting con-

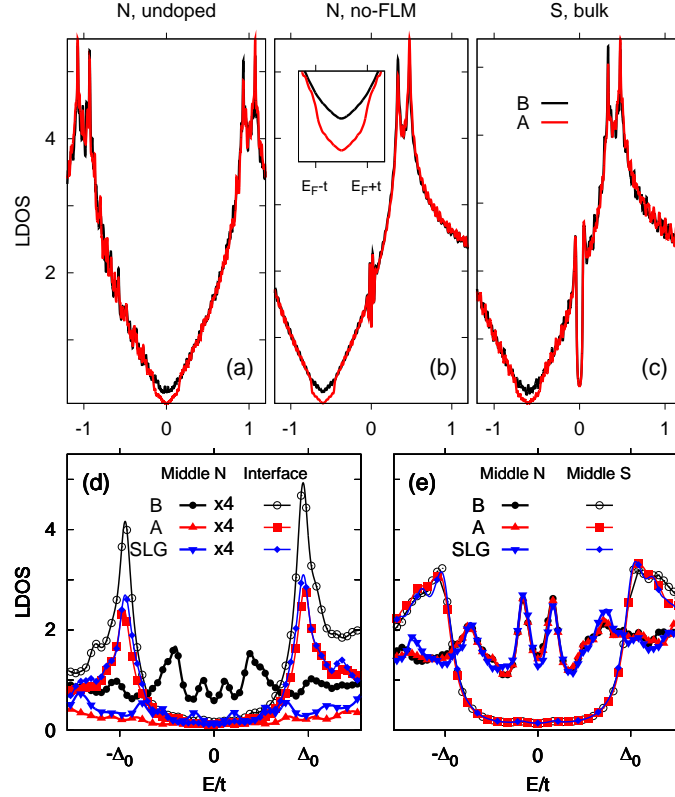


Figure 3.3: LDOS for A (red) and B (black) sub-lattice sites in the N region with (a) zero doping (at the Dirac point) and (b) heavy doping (or with no-FLM between the superconducting and normal regions). (c) LDOS in the highly doped S region showing the superconducting gap. The inset in panel (b) emphasizes the difference in the LDOS between A and B sublattice: a vanishing and finite density of states around the Dirac point. A magnification of (a) around the Dirac point is shown in panel (d) as well the LDOS of atomic sites at the interface for both sublattices. A close up view of the panels (b) and (c) around the zero energy is shown in (e) where the superconducting gap in the S region and the Andreev states in the highly doped N are discernible. SLG analogous cases (blue) have been included for comparison purposes. Note that the results presented here correspond to the long junction limit.

tacts and doping levels in the non-superconducting region. We show in Fig. 3.5 the phase-dependence of the current for both SLG and BLG for no-FLM cases with $\mu_N = 0.6t$, panels (a,b), slightly doped with $\mu_N = 0.1t < t_\perp$, panels (b,c) and undoped, panels (e,f). We consider both regimes, short junctions, panels (a,c,e), and long junctions, panels (b,d,f). Note that, in most of the cases shown

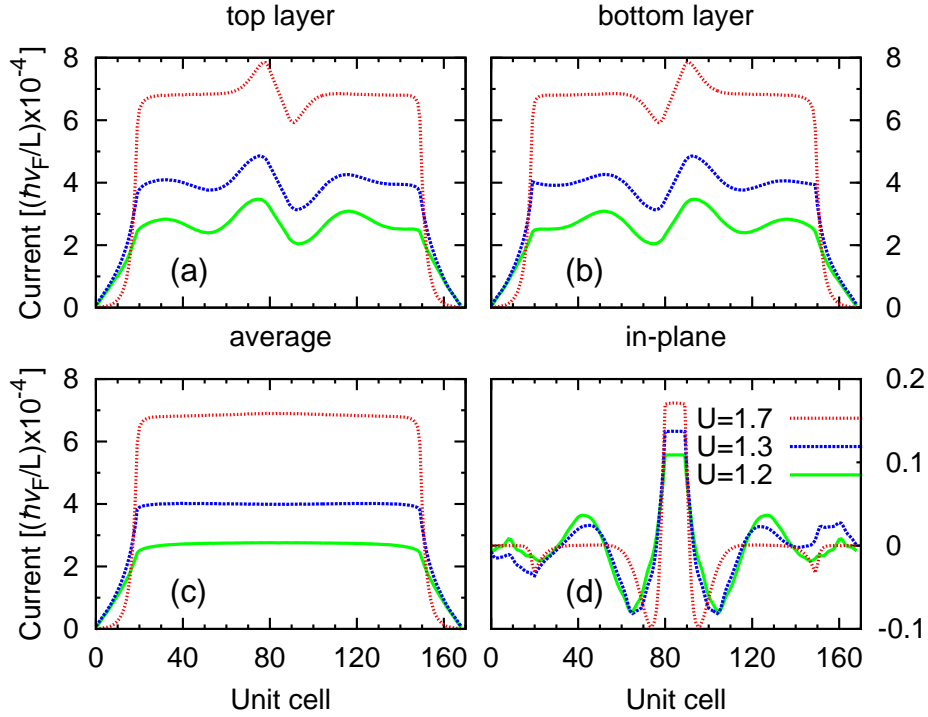


Figure 3.4: Self-consistent Josephson current as a function of position along the \hat{y} -direction for top (a) and bottom (b) layer as well as the average current (c) in the system for different values of the pairing potential, i.e. different coherence lengths. The inter-layer current between the \hat{A} - \hat{B} dimer sites is plotted in (d).

in Fig. 3.5 a complete description of the current over the full $[0, \pi]$ phase-range is not possible. This restriction appears as a consequence of the relaxation of the phase over the S region which becomes significant as the FLM is reduced in the junction until S and N regions are equally doped and the phase drop goes linearly through the self-consistent region. Therefore the phase difference over the normal region will always be smaller than the applied phase difference in the superconducting regions. A similar constraint is found for SLG-based junctions, as is shown in Fig. 3.5 and which was previously pointed out by Black-Schaffer *et al.* [121]. We find that for no-FLM situations the Josephson current density and the CPR of the BLG is almost identical to the one in SLG for both short and long junction. In contrast, for the undoped and slightly doped cases the short and long junctions have different behavior. Short BLG junctions are similar to short SLG ones, while for long BLG junctions the Josephson current is suppressed. The origin of this suppression could be traced back to the sublattice polariza-

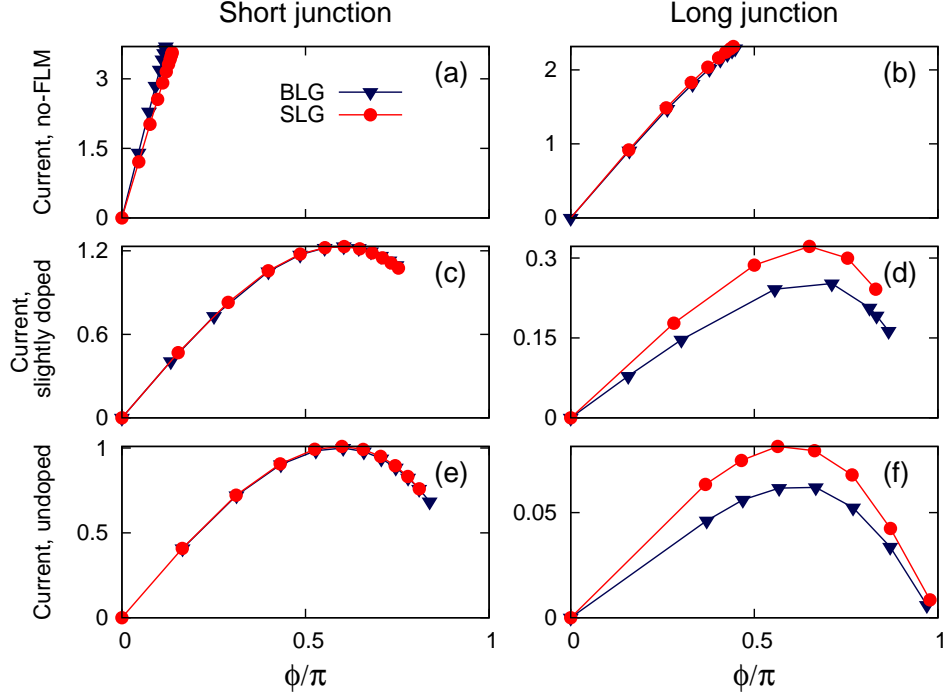


Figure 3.5: Current-phase relation normalized to the critical current found in (e) for SLG and BLG-based junctions considering different doping levels in the N region: (e),(f) undoped $\mu_N=0$, (c),(d) slightly doped $\mu_N=0.1t$ and (a),(b) no-FLM $\mu_N=\mu_S=0.6t$ for short (a),(c),(e) and long (b),(d),(f) junctions. The short and long junction lengths are $L = 10$ and $L = 50$, respectively.

tion of the leaking distance which remains even for doping levels lower than the interlayer hopping energy, t_{\perp} . While one sublattice (non-dimer sites) has an enhanced leaking distance, the other sublattice (dimer sites) behaves like an insulator with a short leaking distance. The resulting combination corresponds to a slightly suppressed Josephson current when compared to SLG.

3.4.3.2 Biased case

Inversion symmetry can be broken in the BLG nano-structure by considering a potential difference, $V_g = \epsilon_1 - \epsilon_2$ with $\epsilon_1 = V_g/2$ and $\epsilon_2 = -V_g/2$, applied between the layers. As a consequence, a tunable gap Δ_0 is induced at the Dirac point for the undoped case and therefore inversion symmetry breaking appears as a good possibility to switch off the superconducting current when the voltage induced gap overtakes the superconducting gap, $\Delta_g > \Delta_0$. At this point, we

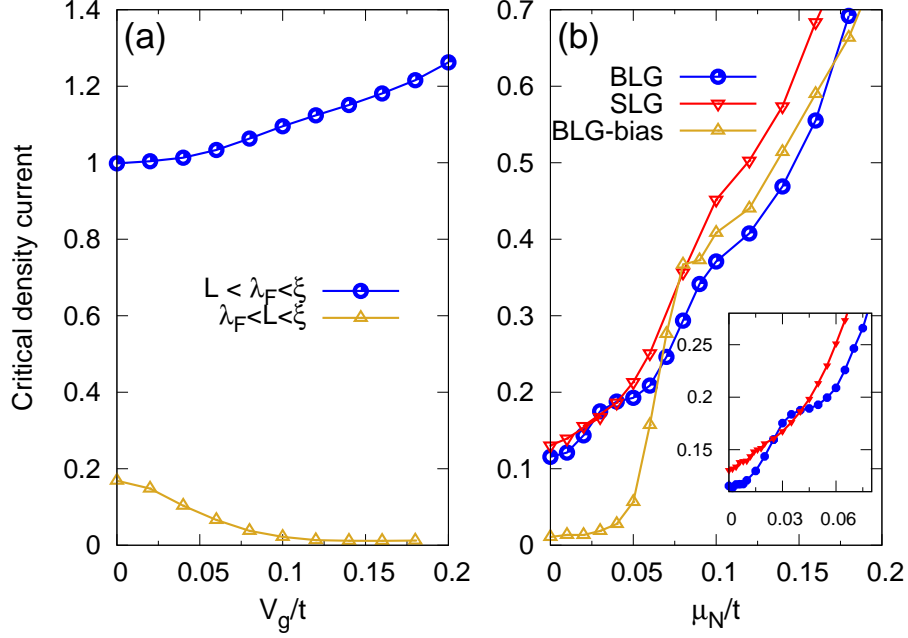


Figure 3.6: Critical density current in a short BLG junction, with $L = 40a$ and $U_S = -1.2t$, as a function of the gate voltage V_g at the Dirac point (a) and the chemical potential μ_N (b). In the left figure two different regimes are considered: $L < \lambda_F$ and $L > \lambda_F$, showing an enhancement and suppression of the superconducting current, respectively. On the right side μ -dependence is plotted for bias and unbiased cases. SLG is included for comparison.

only consider short junctions where such proposal might have potential technological applications. In Fig. 3.6(a) we show the dependence of the supercurrent on the applied bias voltage, V_g , perpendicular to the BLG layer. We observe two distinct regimes, according to the relation between the Fermi wavelength and the junction length. In the case when $\xi > \lambda_F = \hbar v_F / (V_g/2) > L$, we observe an enhancement of the Josephson current. This is because the charge density in the junction does not recover its bulk expected value when the BLG is under bias ($+n$ for one layer and $-n$ in the other layer) but has a finite positive value. In this regime the junction is effectively doped, thus showing an enhancement of the current. A different dependence of the current is achieved when $\xi > L > \lambda_F$. In this case for the center of the junction the charge density has the opposite polarity, and the expected suppression of the current with bias voltage is obtained.

In Fig. 3.6(b) we show the μ -dependence of the current for the biased and unbiased cases. A doping activation is found in the bias case for an energy value around Δ_g , in addition a slight increase in the current is observed at $\mu_N \approx \Delta_g$ due to the enhancement of the LDOS above the gap edge. SLG results are included in order to compare directly with BLG and show that for the chosen length the current density is slightly larger in SLG. In the inset of Fig. 3.6(b) we focus on the low doping regime and observe that in BLG additional oscillations appear, reminiscent of what was previously found analytically in the Dirac approximation [125].

3.5 Conclusions

In conclusion by using an efficient numerical procedure we have solved self-consistently the Bogoliubov de Gennes equations for a tight-binding model of the AB-stacked bilayer graphene Josephson junction. When compared to single layer graphene Josephson junctions we uncover several regimes. First, in the short junction regime, the current density is similar for SLG and BLG for any doping of the normal junction region. Second, in the long junction regime, for undoped junctions, the BLG current density is suppressed while for doped junctions (with doping larger than t_\perp) the BLG and SLG junction behave in a similar way. We attribute the peculiar behavior of the undoped BLG junctions to the difference of the LDOS between the dimer and non-dimer sites, which give suppressed or enhanced Cooper pair leaking distances depending on the sublattice. We have calculated the current-phase relation and showed that similar to SLG, even for short junctions there is a departure from conventional symmetric current-phase relation. Finally, we have shown that by applying a gate voltage perpendicular to the BLG a gap in the spectrum can be induced and a supercurrent switch can be achieved given that the junction length is larger than the Fermi wave-length.

Publication The results of this chapter were published as:

- W. A. Muñoz, L. Covaci and F. M. Peeters, *Tight-binding study of bilayer graphene Josephson junctions*, Phys. Rev. B **86**, 184505 (2012) (7 pages).

4

Tight-binding description of intrinsic superconducting correlations in multilayer graphene

Superconducting pair correlation in rhombohedral (ABC) and Bernal (ABA) multilayer graphene considering a finite intrinsic s-wave pairing potential are investigated. By using highly efficient GPU-based simulations of the tight-binding Bogoliubov-de Gennes equations, we find that the two different stacking configurations have opposite bulk/surface behavior for the order parameter. Surface superconductivity is robust for ABC stacked multilayer graphene even at very low pairing potentials for which the bulk order parameter vanishes, in agreement with a recent analytical approach. In contrast, for Bernal stacked multilayer graphene, we find that the order parameter is always suppressed at the surface and that there exists a critical value for the pairing potential below which no superconducting order is achieved. We considered different doping scenarios and find that homogeneous doping strongly suppresses surface superconductivity while non-homogeneous field-induced doping has a much weaker effect on the superconducting order parameter. For multilayer structures with hybrid stacking (ABC and ABA) we find that when the thickness of each region is small (few layers), high-temperature surface superconductivity survives throughout the bulk due to the proximity effect between ABC/ABA interfaces where the order parameter is enhanced.

4.1 Introduction

Superconducting correlations in graphene-based structures have been the focus of intensive theoretical and experimental research even before graphene became one of the most important topics in condensed matter physics. Following last decade experimental evidences reporting hints of superconductivity behavior in graphite [54] and graphite intercalated compounds [23, 34, 35, 131], a considerable amount of theoretical studies have been devoted to provide a clear understanding about possible mechanisms that could induce intrinsic superconducting states in single and multilayer graphene [30, 33, 37, 42, 43, 132–134]. More recently experimental investigations have reported intriguing traces of high-temperature superconducting behavior in highly oriented pyrolytic graphite (HOPG) samples [36, 52, 135], feeding speculations about the existence of intrinsic superconducting correlations in graphite and graphite-based compounds. Despite the fact that most of these experimental evidence suggests that superconductivity in graphite compounds appears due to external causes, several theoretical studies reveal the possibility of inducing superconductivity in graphite by considering unconventional symmetry of the order parameter [33, 37, 43, 132, 133]. However, these calculations show that superconductivity becomes stable after considering disorder [132] or high doping in the graphene layers [33, 37] while surface superconductivity appears to be stable in clean rhombohedral graphite in the absence of external doping [134]. Considering that most of these calculations are based on a reduced Hamiltonian or are performed within two-dimensional models, by ignoring the interplanar hopping, a numerical description of the superconducting correlation in multilayer graphene is urgently needed.

In view of this, we provide in the following a numerical description of intrinsic superconductivity in multilayer graphene at the tight-binding level. Following Ref. [134], we consider a simple *s*-wave pairing symmetry in a ABC (or rhombohedral) stacking multilayered graphene structure. Calculations are also performed for ABA (or Bernal) stacking where its quadratic low-energy band structure [83] shows a remarkable difference from the $|p|^N$ momentum dependent band structure seen in ABC multilayer [89] structures. In particular we are interested in the limit of large number of layers (N) where the lower-energy band in the rhombohedral case is flat over a large region in *k*-space signaling the suppression of the kinetic energy and therefore the strong effect of interactions. In addition, because of the sensitive stacking dependent band structure in multilayer graphene, we also considered hybrid stacking cases. It is known that exfoliated few-layer graphite samples are usually found to exhibit very stable Bernal stacking but often also display rhombohedral structures in part of the sample [136, 137]. It is worth mentioning that during the preparation of the

manuscript, new experimental results revealed the existence of superconducting correlations at two-dimensional interfaces that appear when angle misalignments about the c -axis exist in HOPG [36].

By using highly efficient graphics card (GPU) simulations of the tight-binding Bogoliubov-de-Gennes equations, we are able to solve self-consistently for the pair correlation in multilayer graphene by considering both planar and inter-planar coupling between nearest neighbors. Translational invariance is assumed along the 2-dimensional direction within the graphene sheets. In this way, an adequate description for the profile of superconducting correlations along the direction perpendicular to the graphene layers is achieved.

Our results confirm the main features of recent analytical approaches for ABC rhombohedral graphite where an enhancement of surface superconductivity, with respect to its bulk analog, was predicted [134].

The chapter is organized as follows. In Sec. 4.2 we introduce the model and the numerical approach that we use. In Sec. 4.3 we present and discuss the results of our numerical calculations. Finally, we briefly summarize our findings in Sec. 3.5.

4.2 Model and calculation approach

Superconducting correlations in multilayered graphene structures are described by the following mean-field single particle Hamiltonian written in Nambu space:

$$\mathcal{H} = \sum_{\substack{\langle l,m \rangle \\ \langle i,j \rangle}} \begin{pmatrix} c_{l\uparrow}^{i\dagger} & c_{l\downarrow}^i \end{pmatrix} \begin{pmatrix} \hat{\mathcal{H}}_{lm}^{ij} & \Delta_l^i \delta_{ij} \delta_{lm} \\ \Delta_l^{i*} \delta_{ij} \delta_{lm} & -\hat{\mathcal{H}}_{lm}^{ij\dagger} \end{pmatrix} \begin{pmatrix} c_{m\uparrow}^j \\ c_{m\downarrow}^{j\dagger} \end{pmatrix} \quad (4.1)$$

where the summation, $\langle i, j \rangle$, is done over nearest neighbors within each layer while the summation, $\langle l, m \rangle$, is done for adjacent layers. The non-diagonal elements Δ_l^i correspond to the s-wave superconducting order parameter at the atomic site i in layer l while the diagonal elements $\hat{\mathcal{H}}_{lm}^{ij}$ are the normal state components of the Hamiltonian:

$$\hat{\mathcal{H}}_{lm}^{ij} = [-t_0(1 - \delta_{i,j}) - \mu_l \delta_{i,j}] \delta_{l,m} - t(\delta_{l,m+1} + \delta_{l,m-1}) \quad (4.2)$$

where μ_l is the chemical potential and, following the schematic layout of Fig. 2.3, nearest-neighbors sublattices A and B are coupled within the layers by the hopping parameter $t_0 \approx 2.8\text{eV}$ (instead of t) while $t = 0.1t_0$ (instead of t_\perp) describes the hopping which couples A sites with the nearest B sites in the adjacent (upper and lower) layers. Bernal and rhombohedral stacking are defined according to the vertical symmetry along the z -axis as shown in Fig. 2.3. Due to this

symmetry, rhombohedral stacking allows us to reduce the description of the superconducting parameter to one of the sublattices, whereas the other sublattice can be deduced from a mirror reflection transformation. For Bernal stacking, we consider a more practical way of sorting sites inside the supercell as dimer sites, which correspond to the sublattices coupled by the interlayer hopping t , and no-dimer sites or sublattices which does not participate in the coupling between adjacent graphene sheets. As we previously pointed out in the previous Chapter 3, the pair correlation behaves differently in these inequivalent sites because at dimer sites the density of states vanishes around the Dirac point while being finite at no-dimer sites where the formation of Andreev states is more feasible.

We will not specify the origin of superconductivity in the multilayer graphene structure, but rather assume $\Delta_l^i = U \langle c_{l\uparrow}^i c_{l\downarrow}^i \rangle$ to be a conventional s-wave symmetric order parameter and the pairing potential U is fixed and homogeneous in the whole structure. Under this assumption and considering translational invariance along the transversal directions, we solve self-consistently for the amplitude of the pair correlation $|\langle c_{l\uparrow}^i c_{l\downarrow}^i \rangle|$ for the sublattice A (or both in the case of N-Bernal stacked layers for N odd), in the z direction. We have considered graphene multi-layer supercells of size $42\text{nm} \times 25\text{nm} \times N$ such that the order parameter is converged and no additional momentum summations in the parallel direction are needed. Thus, $4 \times 10^3 \times N$ atomic sites are distributed in N rectangular graphene layers. Instead of a direct diagonalization of the Hamiltonian we performed the self-consistent mean-field calculation through a numerical approximation of the Gorkov Green's function by using the Chebyshev-Bogoliubov-de Gennes method.

Physical quantities, like the local density of states and the pair correlation function, can be easily determined by using the Eqs 3.8, 3.9 and 3.10 presented in the Chapter 3.

4.3 Numerical results

We solved self-consistently for the order parameter along the z -direction, and show in Fig. 4.1(a) the different profiles of the order parameter (Δ_z) for different values of the pairing potential ($U < 0$) in an ABC stacked graphene with $N=20$ layers. The order parameter is only shown for the A sublattice, while the B sublattice value is achieved by a mirror reflexion symmetry along z , as can be deduced from lattice structure in Fig. 2.3. Analog results are shown in the inset of the Fig. 4.1(a) for the ABA stacking and different values of the pairing potential.

We notice in Fig. 4.1(a), that the superconducting order parameter at the outermost layers is larger than the vanishing pair correlation in the bulk for all the U -values considered here. The same surface enhancement is observed when

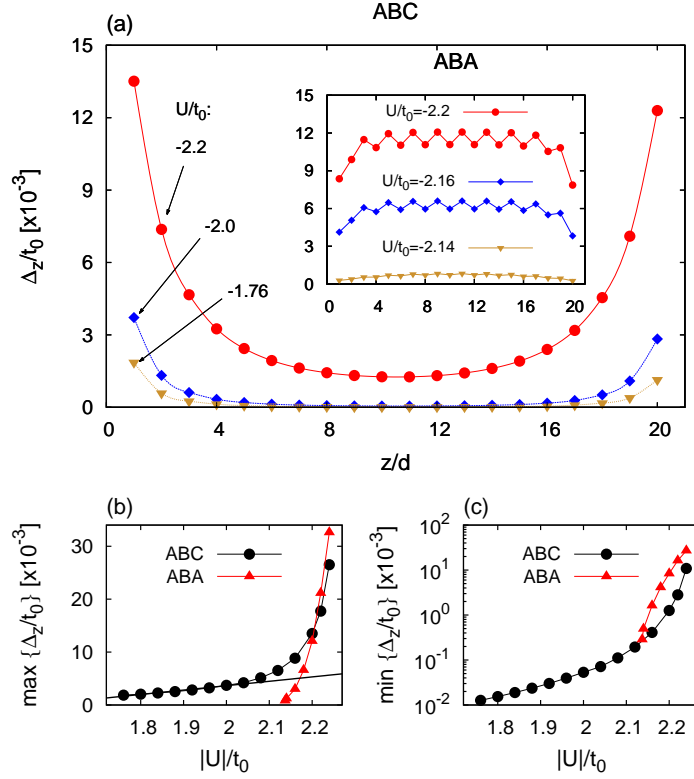


Figure 4.1: (a) Order parameter profile (Δ_z) along the z -direction perpendicular to the graphene sheets (see Fig. 6.1) for various values of the s -wave attractive pairing potential U in ABC stacked multilayer graphene with $N = 20$ layers. The inset shows the corresponding Δ_z profile for the ABA case where dimer and non-dimer sites follow different curves for higher values of U . U -dependence of the maximum (b) and minimum (c) value of Δ_z for both ABC and ABA stacking configuration. $d = 0.335\text{nm}$ is the inter-layer distance.

we decrease the pairing potential such that the penetration of the superconducting order parameter into the bulk becomes strongly suppressed. In the limit of very low pairing potential good agreement could be found with the analytical result previously reported in Ref. [134]. On the other hand, an opposite surface-bulk superconducting ratio is found for the Bernal stacking configuration (see inset in Fig 4.1(a)). Self-consistent calculations performed for ABA show that the bulk value of the order parameter is dominant while surface superconducting correlations are suppressed. Also, we can observe a sublattice polarization in the Δ_z profile where pair correlation is found be higher in non-dimer sites compare

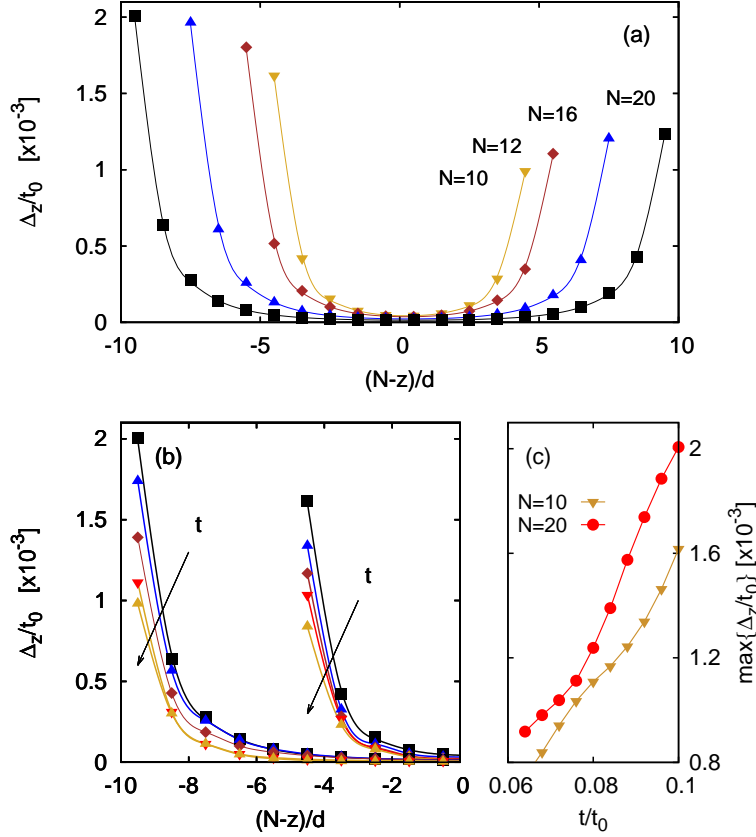


Figure 4.2: (a) Order parameter profile (Δ_z) for a rhombohedral multilayer graphene consisting of various total number of layers $N=10, 12, 16$ and 20 . (b) Order parameter profile for $N=10$ and 20 for different values of the interlayer hopping $t/t_0=0.1, 0.092, 0.084, 0.076$, in decreasing order as this is indicated by the arrows. (c) Dependence of the surface pair correlation, $\max\{\Delta_z\}$, as a function of t . Here we used $U = -1.76t_0$.

to dimer sites with an energy difference which become smaller as the pairing potential is decreased. We return to this issue in a later discussion about density of states.

A direct comparison between surface and bulk value of the pair correlation is given in Figs. 4.1(b) and 4.1(c) for both stacking configurations. Fig. 4.1(b) shows the maximum values of the superconducting correlation for both ABC and ABA cases for different values of U . According to the profiles observed in Fig. 4.1(a), the maximum value of the order parameter, $\max\{\Delta_z\}$, corresponds to the surface for ABC stacking while for the ABA stacking the maximum value corresponds to the bulk non-dimer sites. In contrast, the log-linear representation

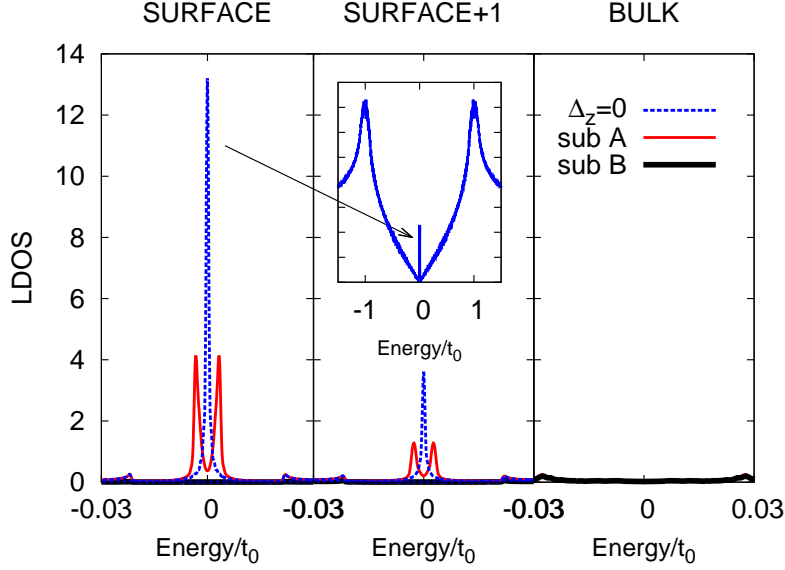


Figure 4.3: Local density of states (LDOS) showing the formation of the s -wave superconducting gap for $U = -2.0t_0$ at both sublattices A and B in different layers around the Fermi energy. Left and center panel show the LDOS at the surface and its adjacent layer while right panels show the LDOS at the bulk. The dashed line represent the corresponding normal state LDOS which shows the localized flat band at the outermost layers. The inset of the central panel shows the surface LDOS in ABC stacked graphene over a wider range of energies.

presented in Fig. 4.1(c) shows the U -dependence of the minimum value of the superconducting order parameter, $\min\{\Delta_z\}$, which corresponds to the bulk and surface locations for ABC and ABA respectively. Two different regimes can be inferred from Figs. 4.1(b) and 4.1(c), depending whether the pairing potential U is larger or smaller than a critical value, $|U_c|/t_0 \sim 2.14$. This value is also very close to the critical pairing for the ABA stacking, below which superconducting correlations vanish. As $|U|$ decreases, but is still larger than $|U_c|$, the order parameter decays exponentially for both ABC and ABA stacking, as the main contribution comes from the bulk. When $|U| < |U_c|$, for ABC stacking, the bulk order parameter vanishes exponentially but the surface one is still finite. Even more interesting is the fact that the surface order parameter decays only linearly and is non-zero for all the values of $|U|$ that we considered in the simulation, down to $|U|/t_0 = 1.76$ giving a surface order parameter $\Delta_{max}/t_0 = 0.002$. The self-consistent calculation becomes increasingly intensive as the order parameter decreases since more Chebyshev moments are needed to resolve the Green's function at higher and higher resolutions.

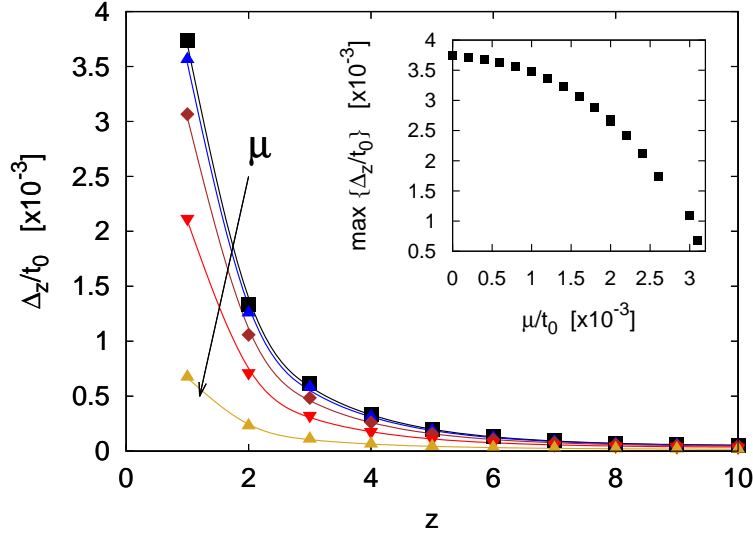


Figure 4.4: Effect of homogeneous doping on the intrinsic s-wave superconducting order parameter in a multilayer rhombohedral graphene with $U = -2.0t_0$. We shown here half of the profile for different doping values, $\mu/t_0 \times 10^{-3} = 0, 0.8, 1.6, 2.4$ and 3.1 , in decreasing order indicates by the arrow. Inset: Evolution of surface superconductivity ($\max\{\Delta_z\}$) as a function of doping (μ) showing that an increase in μ leads to a strong suppression of the order parameter at the surface.

The bulk behavior resembles the superconducting critical point reported for graphene, where in the undoped case it was found that critical the temperature vanishes below a finite value of an s-wave pairing interaction [38]. In contrast, the $|U|$ dependence of the surface order parameter in the ABC stacking configuration suggests that the surface states, which form a flat band with suppressed kinetic energy, are strongly influenced by any exponentially small interactions. Since the pair correlation at the surface is always enhanced for ABC stacking and survives even for lower values of the pairing potential, we will further only also report numerical results for this stacking. The dependence of the order parameter on the total number of graphene layers, N , and the interlayer coupling, t , is shown in Fig. 4.2 for $U = -1.76t_0$. An asymptotic enhancement of the surface superconductivity is observed in Fig. 4.2(a) as the Fermi surface size, defined by the flat band localized at the surfaces, increases with the number of layers. On the other hand, the decrease of the interlayer coupling leads to the suppression of the order parameter as this is seen in Fig. 4.2(b). The evolution of the surface pair correlation as a function of t is shown in Fig. 4.2(c) and indicates an almost linear suppression as a consequence of the linear dependence of the Fermi

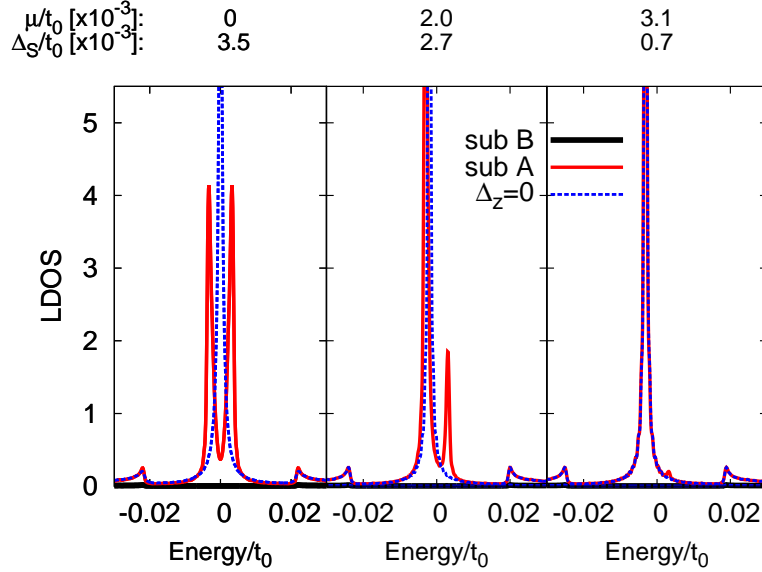


Figure 4.5: LDOS at the surface, on the A sublattice, for $U = -2.0t_0$ and three different dopings considered before in Fig. 4.4. The normal state represented by the dashed line has been included for the corresponding values of doping μ . Δ_S corresponds to $\max\{\Delta_z\}$.

surface size on t . [134]

In order to provide a better understanding of the peculiar behavior of the order parameter profile observed in Fig. 4.1 for the rhombohedral case, we next present the local density of states (LDOS). Fig. 4.3 shows the LDOS in different layers for both sublattices, A and B, within a small energy interval near the Fermi energy. The left panel of Fig. 4.3 represents the LDOS at the surface where the superconducting order parameter is enhanced for sublattice A. There, the normal state LDOS shows a sharp peak due to the existence of flat bands with dispersion $E \sim |p|^N$. The corresponding wave function of these states is localized at the surface and only on sublattice A. A zoomed-out view of the LDOS, over a wider range of energies, is shown in the inset of Fig. 4.3. This is very different for the B sublattice where the density of states vanishes around the Fermi energy and the superconducting coherence peaks are not visible. Despite this, a non-zero solution for the order parameter is obtained for atomic sites belonging to this sublattice as we can see in Figs. 4.1(a) and 4.2. This non-zero solution appears as a consequence of the proximity effect between the intra-layer neighbors A and B sites at the surface. We also observe less pronounced coherence peaks appearing in the LDOS of sublattice A in the layer adjacent to the surface (see

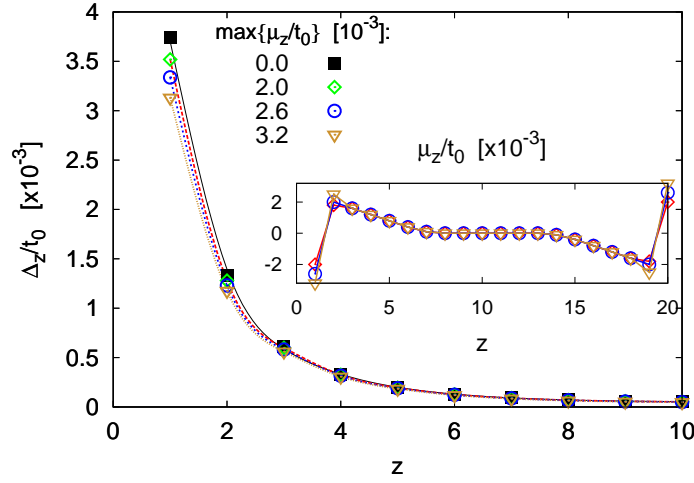


Figure 4.6: Effect of inhomogeneous field-induced doping along the z -direction on the order parameter in a rhombohedral multilayer graphene. Some cases previously shown in Fig. 4.4 are included for comparison. Inset: Doping profile along the z -direction perpendicular to the graphene sheets.

central panel of Fig. 4.3) while the LDOS vanishes for both sublattices in the bulk (see right panel of Fig. 4.3). According to this behavior of the LDOS for rhombohedral stacking, we expect that superconducting correlation will be more stable on the surface and on few adjacent layers rather than in the bulk where the LDOS vanishes around the Fermi energy.

With respect to the LDOS in the Bernal case, it is well known that a sublattice polarization appears around the Fermi energy. A finite density of states is found for non-dimer sites while the density of states vanishes at the dimer sites [89]. Such a polarization allows a finite order parameter to be induced only by large s -wave pairing potentials and therefore bulk superconductivity will not be stable for values of U for which surface superconductivity in ABC is still finite (see Fig. 4.1(b)). In this way, the suppression of surface superconductivity seen in Fig. 4.1(c) for ABA appears as a consequence of the lower density of states for surface non-dimer sites when compared to its bulk value. In order to see the effect of external factors we have considered homogeneous doping, as well as an inhomogeneous field-induced charge distribution, along the z -direction. The first case corresponds to graphite-intercalated compounds where dopant atoms are placed between the graphene layers while the inhomogeneous case can be easily realized in an experimental set-up where top and bottom electrodes have opposite gate voltages. Fig. 4.4 shows the evolution of the order parameter pro-

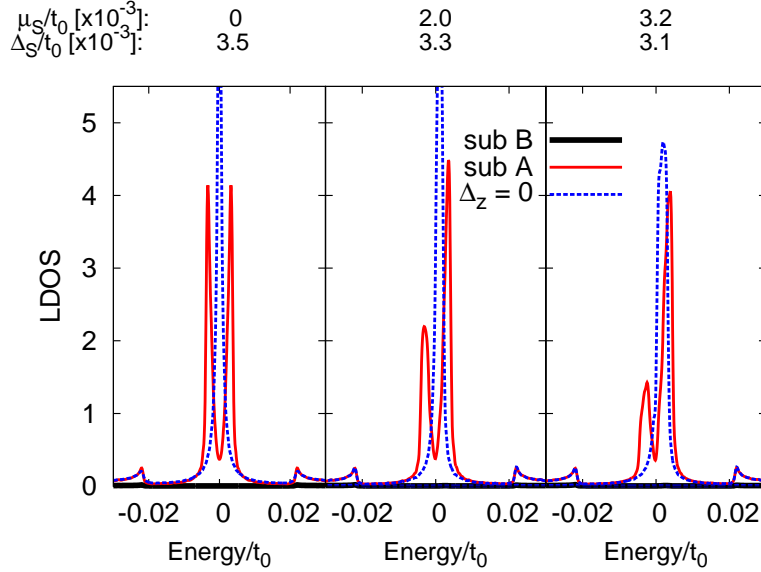


Figure 4.7: LDOS showing the effect of field-induced doping along the z -direction (see inset in Fig. 4.6) on surface superconductivity, obtained for $U = -2.0t_0$ in ABC multilayer graphene. Dashed curves represent the corresponding normal state LDOS.

file as a function of the homogeneous doping $\mu_z = \mu$ for a fixed value of the pairing potential $U = -2.0t_0$. Notice that, surface superconductivity becomes strongly suppressed as the doping shifts the Dirac point away from the Fermi energy. Total suppression occurs for doping lower than the value of the order parameter at the surface. Looking at the LDOS we found that this critical doping coincides with the extinction of the coherence peaks and the rising of the single peak away from the Fermi energy. Despite the fact that we do not find any relevant difference between homogeneous doping and surface only doping in our self-consistent calculation, the value of the critical doping is slightly higher than the one reported by the analytical results [134] where the critical doping was found to be $\mu_{crit} = (2/3)\Delta_S$. In addition to the homogeneous case we have also considered inhomogeneous doping, achieved when an electric field is applied perpendicular to the graphene sheets. Following Ref. [138] where the potential distribution due to an electric field was self-consistently calculated by taking into account screening effects, we consider the z -dependent doping as described in the inset of Fig. 4.6. For comparison purposes we have considered the same pairing potential $U = -2.0t_0$, as we did in Fig. 4.4, and three different cases for which the doping at the surfaces is strongly suppressing the superconducting correlations in the homogeneous case. Surprisingly, in contrast to homogeneous

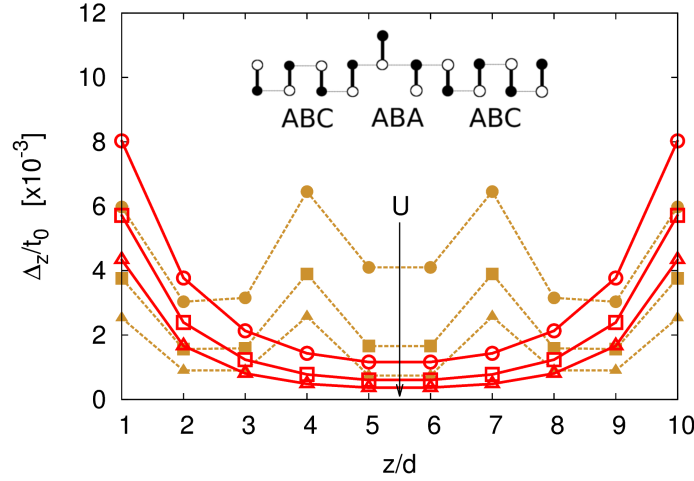


Figure 4.8: Self-consistent order parameter profile for a multilayer graphene considering the stacking configuration shown in the top part. Different point types correspond to different values of the pairing potential, $U/t_0 = 2.16, 2.12$ and 2.08 , where U decrease in the direction pointed by the arrow. Open points represent the corresponding cases for an ordered ABC stacked multilayer graphene.

doping, we found that the field-induced doping suppresses only slightly the pair correlation at the surface. According to this result, the electric-field induced gap in the inhomogeneous case is much lower than the value of the doping at the surface [138]. Therefore, even considering the same surface doping in both cases, superconducting correlations are weakly affected by an inhomogeneous doping configuration. Fig. 4.7 shows how coherence peaks still survive for this doping configuration even if the value of the doping at the surface is on the order of the surface order parameter (as obtained for zero-doping). This is in contrast with the effect observed in Fig. 4.5 where for a similar level of the doping causes a strong suppression of the superconducting gap. Finally, we consider multilayer graphene with hybrid stacking. In order to shift the high-temperature surface superconductivity, observed in ABC, to the bulk of the structure, we propose an intercalated hybrid stacked graphite with few layers. Numerical calculations considering stacking faults in multilayer graphene were recently reported [139], showing that surface superconductivity survives at the interface between ABC and ABA stacking. However, superconductivity in the bulk is still seen being suppressed when the thickness of the hybrid layers is large. By considering a few-layer structure where the external layers have the ABC stacking configuration while the inner ones have ABA stacking, we expected a slight suppression of

surface superconductivity and an enhancement of its bulk value. Fig. 4.8 shows self-consistent results obtained for the hybrid structure depicted in the top part of the figure. While surface superconductivity appears suppressed as compared to the non-hybrid ABC multilayer, bulk correlation are also enhanced. On the basis of these results we suggest that this kind of hybrid stacked multilayer structure, or more complex combinations, could support high temperature superconductivity due to the interplay between surface superconductivity present in ABC stacking and the bulk superconductivity preserved in the ABA case.

4.4 Conclusions

By using a highly efficient GPU-based numerical procedure we solved self-consistently for the s-wave order parameter within a mean-field approach for a tight-binding model of the ABA and ABC-stacked multilayer graphene. Main findings show that a surface superconducting state appear when the multilayer is in the ABC stacking configuration. Opposite behavior is seen for the ABA stacking where bulk superconductivity is predominant but unstable below a certain critical pairing potential. The LDOS for surface sites shows peculiar coherence peaks and sublattice polarization, i.e. large LDOS in one sublattice and zero in the other. We showed that under homogeneous doping this state is quickly suppressed. We extracted a critical doping which is slightly higher than the one reported previously based on an approximate analytical study [134]. In addition, we considered a field-induced inhomogeneous doping and showed that the superconducting correlations survive in this case for higher values of μ_S . Finally we pointed out the importance of hybrid stacking structures where surface superconductivity related to ABC stacking could be preserved even in the bulk of the structure, suggesting a possible path for the survival of high temperature superconductivity.

Publication The results of this chapter were published as:

- W. A. Muñoz, L. Covaci and F. M. Peeters, *Tight-binding description of intrinsic superconducting correlations in multilayer graphene*, Phys. Rev. B **87**, 134509 (2013) (7 pages).

5

Superconducting current and proximity effect in ABA and ABC multilayer graphene Josephson junctions

Using a numerical tight-binding approach based on the Chebyshev-Bogoliubov-de Gennes method we describe Josephson junctions made of multilayer graphene contacted by top superconducting gates. Both Bernal (ABA) and rhombohedral (ABC) stacking are considered and we find that the type of stacking has a strong effect on the proximity effect and the supercurrent flow. For both cases the pair amplitude shows a polarization between dimer and non-dimer atoms, being more pronounced for rhombohedral stacking. Even though the proximity effect in non-dimer sites is enhanced when compared to single layer graphene, we find that the supercurrent is suppressed. The spatial distribution of the supercurrent shows that for Bernal stacking the current flows only in the top-most layers while for rhombohedral stacking the current flows throughout the whole structure.

5.1 Introduction

The exceptional characteristics of carriers in a single graphene layer gives rise to unusual properties of superconductor-graphene junctions such as specular Andreev reflection [60] and finite superconducting current at the neutrality point [59]. Although there is still no clear evidence of the novel electron-hole conversion, a bipolar proximity-induced supercurrent has been detected in superconducting-graphene-superconducting Josephson junctions (JJ) [58, 63–65] opening a new perspective for Josephson field transistors. In these devices, carrier density modulations by the gate voltage plays an important role in controlling the strength of the proximity effect and therefore the dissipationless current flowing through the junction. It is also expected that other graphene structures show interesting properties when in contact with superconducting leads. In fact, Josephson junctions with non-superconducting few-layer graphite films have been the focus of experimental investigations [122, 140–142]. In most of the few preceding theoretical studies [143–145] the proximity-induced superconducting correlations in multilayer graphene were determined using analytical approximations where the electronic description was limited to parabolic energy bands near the Fermi energy. As a consequence the depth dependence of the order parameter was neglected and in some cases the superconducting pair diffusion was reduced to a 2-dimensional scenario, therefore ignoring any spread of the Cooper pairs among the different layers. Since all the experimental setups require top superconducting contacts, a calculation taking into account the depth dependence of the pair correlation is needed. Here, we describe the 3-dimensional diffusion of Cooper pairs through a non-superconducting multilayer graphene junction connected to two top superconducting electrodes. The Josephson superconducting current is also studied by setting a phase gradient between the superconducting leads. We find significant differences between the two possible stacking orders, Bernal and rhombohedral. For junctions with Bernal stacking the supercurrent flows mostly through the two top-most layers while for junctions with rhombohedral stacking the current is weaker and spread throughout the whole multilayer. We consider a multilayer graphene junction, shown in Fig. 5.1, where the top layer is in contact with two superconducting leads separated by a distance L , which corresponds to the junction length. We adopt the non self-consistent method employed in Ref. [128] where three-dimensional superconducting leads were assumed to act as external reservoirs of Cooper pairs. In our case the superconducting contacts, are single layer graphene with an intrinsic s-wave order parameter, $\Delta_0 = 0.1t_0$, and a high doping level, $\mu_s=0.6t$, where $t_0=2.8\text{eV}$. The coupling between the graphene multilayer and the superconducting contacts is chosen such that there is a sizable proximity effect and the edge effects are minimal for the size of the junctions considered here. At the present stage, we assume

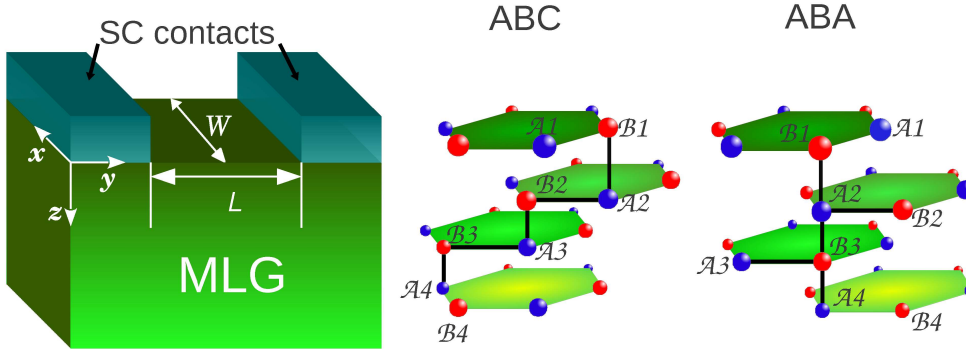


Figure 5.1: Schematic layout of a multilayer graphene JJ showing the superconducting (SC) leads which are separated by a distance L . W corresponds to the width of the junction. On the right-hand side the layer arrangements in multilayer graphene shows the two different stacking configurations: ABC(rhombohedral) and ABA(Bernal).

that the inverse proximity effect on the superconducting contacts is negligible.

It is well known that the electronic properties of multilayer graphene depend strongly on the particular type of coupling between the graphene layers. Likewise, intrinsic electronic correlations have been shown to behave differently according to the stacking configuration [146, 147]. A question that arises naturally is: how different is the superconducting pairing diffusion under the contacts and across the junction for different number of layers and stacking configurations?

Based on this motivation, we perform calculations considering the two most stable interlayer stackings found in multilayer graphene: ABA or Bernal, and ABC or rhombohedral. Bernal stacking is the natural way in which graphene layers are stacked inside graphite. In this case, for $N = 2M + 1$ layers the low-energy electronic dispersion shows $2M$ parabolic energy bands and 1 linear band [83]. On the other hand, for the ABC case the energy band structure for small k disperses as $|k|^N$ such that in the limit of large number of layers (N) the lower-energy band becomes flat over a large region in k -space [89]. This suppression of the kinetic energy results in low-energy surface states localized in the outer layer with a diverging density of states around the K point.

In order to describe superconducting correlations in multilayer graphene we use the same tight-binding mean-field Hamiltonian of Eq. 4.1 as we considered in Chapter 4. Both stacking configurations are defined according to the vertical symmetry along the z -axis as shown in Fig. 5.1. While the vertical atomic arrangement of ABA shows that we have only one sub-lattice per layer (A_l or B_l) participating in the interlayer coupling, both sub-lattices from each layer are directly coupled in the ABC stacking. Despite the fact that both atomic configurations are different we assumed for simplicity the same intra-layer and inter-layer

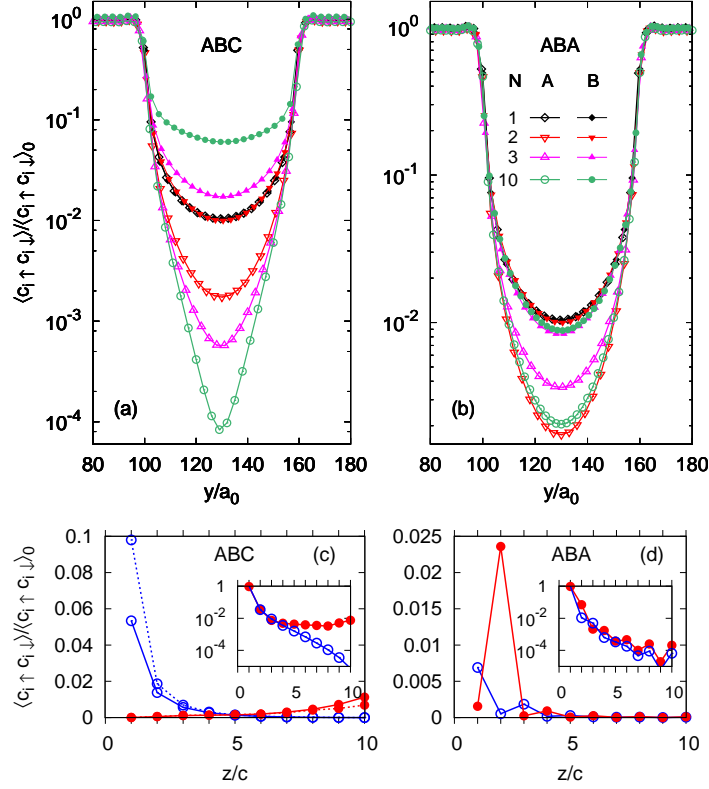


Figure 5.2: Absolute value of the pair correlation along the line $(x, y, z) = (W/2, y, 1)$ in a single-layer graphene JJ and in the top-most layer in (a) ABC and (b) ABA multilayer graphene JJs with $N=2, 3$ and 10 layers. $a_0=3a/2$ where a is the intra-layer C-C distance. Pair correlation function at the middle point of the junction along the \hat{z} vertical axis, $(x, y, z) = (W/2, L/2, z)$, for (c) ABC and (d) ABA multilayer graphene JJs with $N=10$ layers. The integer index z/c , where c corresponds to the distance between adjacent layers, labels the different layers where $z/c = 1$ correspond to the top-most layer and open(close) circles correspond to A(B) sub-lattice (see Fig. 5.1). Dotted lines in (c) correspond to the results obtained for small doping $\mu = 0.0014t$. The insets in (c) and (d) show the vertical profile of the pair correlation at the middle point right underneath the superconducting contacts.

hopping integrals to be t_0 and t , respectively for both cases. We define as dimer (non-dimer) atoms, the atoms that are coupled (not coupled) to adjacent layers.

Since these types of structures involve a large number of atoms (each graphene layer is considered to have hundreds of thousands of atomic sites) numerical calculations are performed by implementing the Chebyshev-Bogoliubov-de-Gennes method. In this way, we can numerically obtain an approximation of the Gorkov-

Green's functions by a superposition of Chebyshev polynomials as described in Eq. 3.5 in Chapter 3.

5.2 Model System

We next present the results of our simulations. In Fig. 5.2 we show the pair correlation profile along a line $(x, y, z) = (W/2, y, 1)$ for single and multilayer graphene JJs with $N = 2, 3$ and 10. In the case of multilayer graphene the profile corresponds to the top-most graphene layer. As expected, in single layer graphene JJ, the pair amplitude decays exponentially in the non-superconducting link in the same way for the A and B sub-lattice. However, a sub-lattice polarization is observed in the behavior of the pair amplitude for the multilayer graphene junctions where the Cooper pair diffusion across the junction has different decay characteristics in the A and B sub-lattice.

Previous self-consistent calculations performed by us revealed a similar sub-lattice polarization in the pair correlation function along a bilayer graphene JJ [148]. It can be observed in Fig. 5.2 that such a polarization of the pair amplitude in the surface depends strongly on the stacking configuration for the multilayer cases with $N \geq 3$. While no relevant differences in the pair depletion at the surface are observed for ABA stacking between the different values of N , a peculiar dependence on N is observed for the ABC case where the leaking distance is highly sensitive to the flatness of the lower energy band, i.e. to the number of layers N . Note in Fig. 5.2(b) that the interlayer coupled B sub-lattice in the top-most layer shows a suppression in the pair correlation while this is enhanced in the A sub-lattice which does not have a direct neighbor in the adjacent layer. In this way, and different from ABA, pair leaking in ABC is found to be larger than in the case of a single layer graphene JJ.

Complementary results are shown in Figs. 5.2(c) and (d) where we plot the pair amplitude along the vertical axis \hat{z} at the midpoint of the junction, $(x, y, z) = (W/2, L/2, z)$, as a function of the integer index z/c , which labels the different layers starting from the top-most layer with $z/c = 1$ (see Fig. 6.1), for both ABA and ABC stacking. Notice that the diffusion perpendicular to the contacts happens quite differently for ABC and ABA stacking. For ABC stacking the pair leaking through the layers decays exponentially for the B sub-lattice while at the same time increases slowly for the A sub-lattice. For ABA stacking the pair amplitude for both dimer and non-dimer sites decays with a coherence length much smaller than the one observed in ABC (for the A sub-lattice). A particular behavior is found for ABA in the non-dimer site at the $(z/c = 2)$ -layer, where a rise of the pair amplitude is observed. This fact can be explained from a density of states point of view because it is well know that the local density of states in

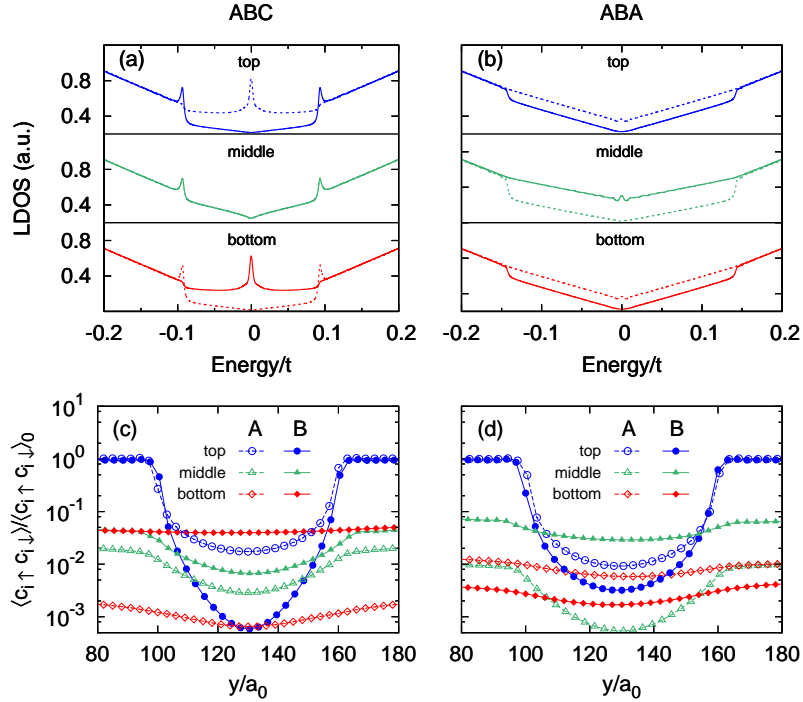


Figure 5.3: (a)-(b) LDOS around the Dirac point for both sublattices A (dashed) and B (solid) in $(x, y, z) = (W/2, L/2, z)$ along the z direction for a trilayer graphene (TLG) JJ with ABC and ABA stacking configuration. (c)-(d) Profile of the amplitude of the pair correlation along the line $(x, y, z) = (W/2, y, z)$ in the different layers of a ABC and ABA TLG JJ respectively.

non-dimer sites is enhanced in the bulk while being suppressed at the surface. We can therefore conclude that the vertical leaking distance is larger in ABC than in ABA.

In order to investigate the relation between the local density of states (LDOS) and the coherence length for both stacking configurations, these are showed in Fig. 5.3 for all the layers in a trilayer graphene (TLG) JJ. Around the Dirac point, the density of states differs for the different sublattices from within the same layer except for the middle layer for the ABC stacking. Sharp peaks are observed for the non-dimer sublattices from the top and bottom layers in ABC stacking, while the density of states vanishes for the dimer sublattices. As we can observe in Fig. 5.3(c), the LDOS peaks lead to longer coherence lengths in those layers. Interestingly, for ABC stacking, we observe that the coherence length for the bottom B sublattice overcomes the one of the top sublattice A. This is due

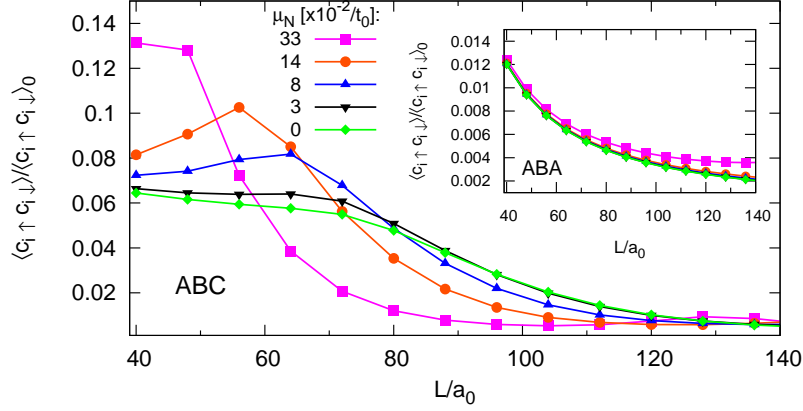


Figure 5.4: Amplitude of the pair correlation at the middle point $(x, y, z) = (W/2, L/2, 1)$ as a function of the junction length L for different values of the doping μ_N for the A sub-lattice in the top-most layer of the ABC and ABA (inset) multilayer graphene JJ containing $N = 10$ layers.

to the fact that the LDOS of the top layer is slightly affected by the coupling to the doped contacts, thus the zero energy peak is slightly shifted away from the Dirac point. Opposite to ABC stacking, where a notable enhancement of the pair amplitude is observed in the outermost layers, for the ABA stacking we show in Fig. 5.3(d) that coherence length is large in the A sublattice of the middle layer, since the LDOS is higher than the one for surface atoms.

Since previous results are performed at the Dirac point, i.e. for $\mu = 0$, we have included in Fig. 5.2(c) an additional case for which the junction is slightly doped by setting a chemical potential $\mu = 1.4 \times 10^{-3} t_0$. These results are shown as dotted lines in Fig. 5.2(c) where we see that the pair correlations are enhanced in the A sub-lattice of the upper layers while being suppressed in the B sub-lattice in the lower layers. Such a high sensitivity of the pair correlation on the chemical potential results from the sharp peak found in the LDOS for the surface sites of ABC multilayer graphene. The LDOS calculations (not shown here) demonstrate that the energy position of this peak is slightly shifted by the coupling of the multilayer graphene with the highly-doped superconducting leads. Therefore, a slight doping will reposition the peak at the Fermi level and contribute to a large modification of the pair correlation.

The pair amplitude for the region underneath the superconducting contacts is shown in the insets of Figs. 5.2 (c) and (d) as a function of the integer index z/c . In this case, an exponential decay is observed for both stacking orders, with the difference that for dimer-sites, in ABC stacking, this decay is much faster. The

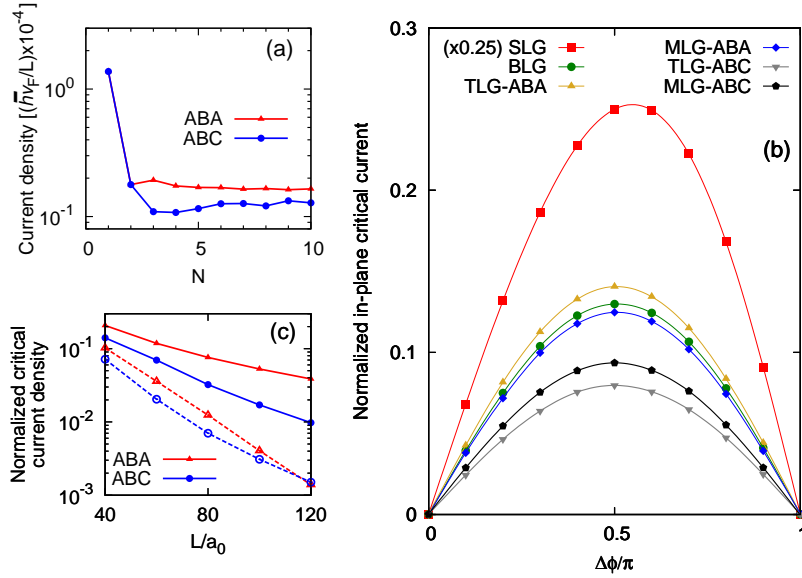


Figure 5.5: (a) Josephson current as a function of the total number of layers, N (b) Current density-phase relation for single ($N=1$), bilayer ($N=2$), trilayer ($N=3$) and multilayer ($N=10$) graphene JJs. Both stackings are considered. (c) Critical current density as a function of the junction length L for $T=0K$ (solid lines) and $T=10K$ (dashed lines). Note that the current densities in panels (b)-(c) are normalized by the maximum Josephson current obtained for single layer graphene, as shown in panel (a).

dependence of the pair correlation at the midpoint of the junction corresponding to the A sub-lattice in the top-most layer is shown in Fig. 5.4 as a function of the length of the junction for different values of the chemical potential μ . The L -dependence for ABC is notably different from the usual exponential decay observed in the ABA case (see inset Fig. 5.4). Each doping level exhibits a maximum for different values of L . The unusual behavior is a consequence of the electron-hole asymmetry induced in the junction by the contact. Since very low values of doping in the normal region shifts the sharp LDOS peak localized at the surface, this has a strong effect on the decay of the pair amplitude. We found that a maximal effect is achieved when the value of the doping coincides with the energy position of the peak from the undoped case for each junction length. As this effect is coming from the influence of the leads on the surface state, there is a small dependence of this optimal doping on L .

Since there are remarkable differences in the pair diffusion between ABC and ABA multilayer graphene it is expected that the superconducting current behaves differently in the two cases. In order to induce a zero-voltage super-current we set a phase difference, $\Delta\phi$, between the left and right superconducting

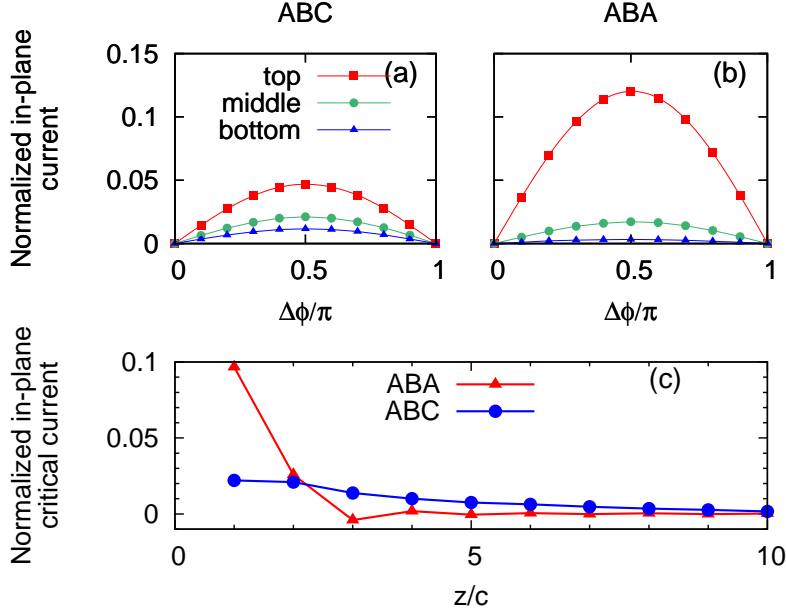


Figure 5.6: In-plane current-phase relation for the different layers in (a) ABC and (b) ABA stacked trilayer ($N=3$) graphene JJ. (c) z resolved in-plane critical current through the different graphene layers for ABC and ABA multilayer graphene JJs with $N=10$. Note that the current densities in panels (a)-(c) are normalized by the maximum Josephson current obtained for single layer graphene, as shown in Fig. 5.5 (a).

contacts. We observe that the same phase difference is kept along the vertical axis \hat{z} between two regions underneath the contacts which are away from the junction. However, near and inside the multilayer junction, the gradient of the phase along both the \hat{z} and \hat{y} directions varies in a different way in the two stacking configurations. This shows that the supercurrent is finite both within the intra-layers and between the inter-layers.

In Fig. 5.5(a) we plot the current density integrated over \hat{z} as a function of the number of layers for the two stacking configurations. Notice that the largest current density was obtained for single layer graphene while for the cases with $N \geq 2$ the current is suppressed. Interestingly, the current is always higher for ABA than ABC. In Fig. 5.5(b) we plot the current-phase relation and observe the same dependence on the stacking configuration. For $N \geq 2$ the current-phase relation has the conventional $\sin(\Delta\phi)$ dependence for short junctions. The length dependence of the current density is shown in Fig. 5.5(c) for two temperatures, 0 and 10K. Clearly, the current decays exponentially with the junction length. This is in contrast to the experimental finding from Ref. [122], where a linear length

dependence was uncovered. We believe that the main reason for this discrepancy comes from the different experimental setup, which considers a bottom gate that dopes only the lower layers.

In order to further elucidate these discrepancies we plot in Figs. 5.6(a) and (b) the current-phase relation for each layer of the trilayer graphene JJ while in Fig. 5.6(c) we shown the \hat{z} profile of the current for both stackings in the case of a multilayer with $N=10$. Thereby we find that the surface current is highly dominant in ABA stacking for which most of the current is observed in the two upper layers. This also explains the very weak dependence of the ABA current on the number of layers (see Fig. 5.5(a)). Alternatively, for ABC stacking the current is much more spread throughout the whole multilayer also explaining the stronger dependence of the current on the number of layers. In addition, for ABC stacking the larger the number of layers, the flatter the low energy band will be, which in turn will have an effect on the supercurrent by enhancing it.

5.3 Conclusions

In conclusion, by using a numerical tight-binding approach for multilayer graphene contacted by two superconducting electrodes, we showed how the Cooper pairs diffuse both perpendicular and across the junction. We found that the proximity effect as well as the induced supercurrent are strongly dependent on the stacking configuration of the multilayer structure. For both ABA and ABC stacking we observe a polarization of the pair amplitude between dimer and non-dimer sites. This effect is enhanced in ABC stacking due to the peculiar flat band at the Fermi level which is localized at the surface. Interlayer pair leaking is found to decay exponentially with a vertical-leaking distance larger in ABC than in ABA stacking. Despite the fact that the proximity effect is enhanced in ABC we found that the induced-current is larger in ABA but most of the current flows through the first two surface layers as opposed to ABC where the current is spread throughout the whole structure. We are therefore proposing that future experimental setups should use all the gates on the same side of the multilayer in order to take advantage of the surface currents.

Publication The results of this chapter were published as:

- W. A. Muñoz, L. Covaci and F. M. Peeters *Superconducting current and proximity effect in ABA and ABC multilayer graphene Josephson junctions*, Phys. Rev. B **88**, 214502 (2013) (5 pages).

6

Disordered graphene Josephson junctions

A tight-binding approach based on the Chebyshev-Bogoliubov-de Gennes method is used to describe disordered single-layer graphene Josephson junctions. Scattering by vacancies, ripples or charged impurities is included. We compute the Josephson current and investigate the nature of multiple Andreev reflections, which induce bound states appearing as peaks in the density of states for energies below the superconducting gap. In the presence of single atom vacancies, we observe a strong suppression of the supercurrent that is a consequence of strong inter-valley scattering. Although lattice deformations should not induce inter-valley scattering, we find that the supercurrent is still suppressed, which is due to the presence of pseudo-magnetic barriers. For charged impurities, we consider two cases depending on whether the average doping is zero, i.e. existence of electron-hole puddles, or finite. In both cases, short range impurities strongly affect the supercurrent, similar to the vacancies scenario.

6.1 Introduction

The notable absence of intrinsic superconductivity in graphene has not been an obstacle for recent experimental advances demonstrating potential applications of graphene in superconducting devices by using the proximity effect [58, 67–70]. Despite the fact that the interplay between superconductivity and quantum

relativistic dynamics in graphene, expressed in an unusual Andreev reflection, has been elusive to experiments, advances in lithography make graphene-based superconducting devices a possible platform for superconducting quantum engineering. However, it has been observed that superconducting states in graphene are strongly affected by the inherent disorder that is present in graphene samples. More relevant, the specular Andreev reflection predicted to take place in a clean superconducting-normal (S/N) graphene interface and where, different from the conventional retro-reflection, the path of the reflected hole does not retrace the path of the incoming electron, cannot be observed in the presence of dopant inhomogeneities.

Many speculations have been made on the effect of disorder, like for instance the report of a gate-tunable Josephson junction where the off state at the Dirac point is believed to be caused by the suppression of the supercurrent due to intrinsic ripples appearing in graphene [69]. A suppression of the critical current due to the presence of puddles of charges has been reported as well [67]. Thus, disorder can play an important role in graphene superconducting devices.

From a theoretical point of view, the interplay between superconductivity and disorder in graphene has not been thoroughly investigated. In only a few exceptional cases, works showing the role of disorder in intrinsic superconductivity [149], as well as in S/N graphene interfaces [150, 151] have been recently reported. For instance, a counter-intuitive enhancement of superconductivity by weak disorder has been predicted, while others have shown that the presence of disorder prevents the observation of the specular Andreev reflection and suppresses intrinsic superconductivity in graphene. From the perspective of the continuum Dirac approximation only scattering processes which mix the K and K' valleys, are predicted to matter [61]. However, it has been shown that inhomogeneous strain, which breaks the effective time-reversal symmetry in each cone but not the true time-reversal symmetry, can lead to the suppression of the Cooper diffusion in a graphene Josephson junction [128] by generating a pseudomagnetic barrier and allowing supercurrents to flow only as edge states.

The effect of disorder in graphene has been widely studied [9, 152] and was shown to break various symmetries, like the chiral or the effective time-reversal symmetries. The absence of these symmetries may strongly affect electronic transport [152–154]. The first and most commonly investigated type of extrinsic disorder corresponds to charge inhomogeneities [153, 155]. This type of disorder resembles charged puddles, which are usually present when graphene is put on a substrate [156], or when e.g. water molecules are deposited on its surface. Depending on the strength of the potential generated by these charged impurities, or the distance from the graphene sheet, they can be considered as long-range or short-range potentials. For instance, elastic scattering from a short-range disorder potential may mix electron states in different valleys K and K' , i.e.

inter-valley scattering. Instead, for a long-range potential varying smoothly over scales larger than the lattice constant, electrons in the K and K' valleys do not mix.

Scattering on vacancies, i.e. the absence of a carbon atom [153, 157, 158], unlike charged potentials, induces resonant states near the Dirac point. This short-range unitary scatterer may introduce a localized state, for which the wavefunction is formed equally from both K and K' [157] valleys, similar to the nature of the wavefunction at armchair edges. For this type of disorder, coupling between valleys is expected to occur [159] and thus have a strong influence on the supercurrent.

Yet another type of disorder is induced by lattice distortions, either intrinsic or designed by strain engineering. Due to its exceptional flexibility graphene can be easily deformed by mechanical stress or conform to the geometry of the substrate. Unusual high pseudo-magnetic fields have been predicted to emerge from strained graphene [15]. In fact, theoretical descriptions have revealed the existence of an effective vector potential coming from the change in the hopping parameter due to the geometrical deformation of the distance between nearest neighbors carbon atoms [160–164]. Particularly, some works have investigated the interplay between superconductivity and uniform strain [125] or pseudo-quantum Hall states in graphene Josephson junctions [128].

Both electrons and holes experience normal scattering inside the junction, therefore different dephasing mechanisms are expected to strongly influence the transmission of the Cooper pair between the superconducting leads. Since the more general description reported so far is based on the continuum Dirac approximation [61] a clear understanding of the effect of disorder in graphene Josephson junction is imperative. In this paper we work directly at the tight-binding level and consider three different types of disorder: vacancies, ripples and impurity scatterers. In all of these cases we find that disorder affects the Andreev bound states that are formed in the junction. For instance vacancies induce a zero-energy mode which destroys the Andreev gap when the concentration of vacancies is increased. Similarly short-range scatterers and strong pseudo-magnetic fields will broaden and subsequently destroy the Andreev peaks. We calculate the Josephson current induced by the phase difference of the superconducting order parameter of the two contacts, and provide a qualitative picture on the effect of various types of disorder.

This chapter is organized as follows: In Sec. II we introduce our model and the numerical approach used. Results are organized according to the type of disorder considered in Sec. III. For instance, results concerning vacancies are presented and discussed in Sec. III(a), while the same is done for the cases regarding ripples and impurity scatterers in Sec. III(b) and (c) respectively. Finally, we summarize our findings in Sec. VI.

6.2 Model

A graphene Josephson junction is modeled according to the layout depicted in Fig. 6.1. Following closely the recipe implemented in previous works [121, 148], we model the influence of the right and left superconducting contacts by assuming an on-site attractive pairing potential $U < 0$ and high doping, $\mu > 0$. In this way, we introduce a s -wave superconducting state over the outermost regions in the graphene sheet separated by a distance L . The width of the junction is considered to be much larger than the junction length, $W \gg L$. We consider here an impurity-free S/N interface and set a high Fermi level mismatch between the superconducting and the normal parts of the junction where the pairing potential is set to zero $U = 0$ (see Fig. 6.1). The large Fermi level mismatch between the highly doped contact region and the undoped interface may suppress Andreev reflection from non-relativistic electrons [165]. We allow disorder only over the middle region of the junction, away from the interfaces, in order to guarantee that the leakage of the Cooper pairs is homogeneous along the clean interface strips. In addition, an absorbing region is imposed at the borders of the junctions in order to eliminate reflections coming from the boundaries and manifesting as finite size effects.

Finally, a dc-Josephson current is induced by fixing a phase difference $\Delta\phi = \phi_R - \phi_L$ between the outermost parts of the contact regions, as shown in Fig. 6.1. The calculation of the supercurrent is performed once the amplitude and the phase of the order parameter is relaxed over the superconducting region and convergence is achieved. The Andreev scattering process [57] in graphene is described within the Bogoliubov-de Gennes formalism by using the Nambu Gor'kov Green functions of Eq. (2.39). The elements of the matrix (2.39) are calculated within the approximation of the Gor'kov Green's functions by implementing the Chebyshev-Bogoliubov-de Gennes method of Chapter 2. The BdG Hamiltonian, in a real-space tight-binding formulation, has the following form at the mean-field level:

$$\mathcal{H} = \sum_{\langle i,j \rangle} \begin{pmatrix} c_{i\uparrow}^\dagger & c_{j\downarrow} \end{pmatrix} \hat{\mathcal{H}}_{ij} \begin{pmatrix} c_{j\uparrow} \\ c_{j\downarrow}^\dagger \end{pmatrix} \quad (6.1)$$

where the matrix \mathcal{H} can be seen as arrangements of matrix blocks as follows:

$$\hat{\mathcal{H}}_{ij} = \begin{pmatrix} \epsilon_i - \mu & \Delta_i \\ \Delta_i^* & \mu - \epsilon_i \end{pmatrix} \delta_{ij} + \begin{pmatrix} -t_{ij} & 0 \\ 0 & t_{ij}^* \end{pmatrix} (1 - \delta_{ij}), \quad (6.2)$$

where ϵ_i denotes the on-site potential of the carbon atoms while μ is the chemical potential which pins the Fermi energy. Nearest-neighbor p_z -orbitals A_i and B_j are coupled through the hopping parameter t_{ij} which is known to be

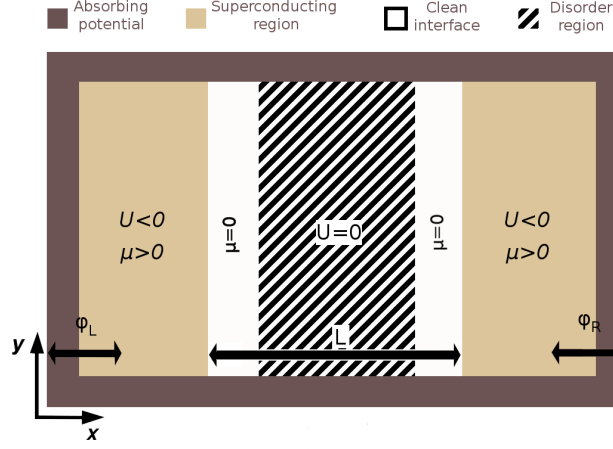


Figure 6.1: Layout of graphene Josephson junction considered in this work. Disordered and superconducting regions are separated by clean interface strips where Andreev reflection takes place.

$t_{ij} = t \approx 2.7\text{eV}$ for pristine graphene, where the minimum distance between carbon atoms is assumed to be $a_0 \approx 1.42\text{\AA}$. Inhomogeneous superconductivity is taken into account through the on-site s-wave order parameter $\Delta_i = U_i \langle c_{i\uparrow} c_{i\downarrow} \rangle$ where U_i corresponds to the strength of the pairing potential and the complex correlation function $\langle c_{i\uparrow} c_{i\downarrow} \rangle$ is derived from the Gor'kov Green function (3.5) according to the Eq. (3.9) in Chapter 3. Another physically relevant quantities considered here are the local density of states and the Josephson current, which are obtained from the Green function (3.5) through the formulas in Eqs. (3.8) and (3.10). In order to obtain the average DOS in the disordered region, we use a more suitable approach to calculate the moments (3.6) is more suitable. It was shown that the average DOS can be expanded in terms of Chebyshev polynomials and the coefficients of order n can be expressed as the trace of the polynomials of order n of the Hamiltonian matrix. Instead of performing the full trace, i.e. averaging over the LDOS, we perform a stochastic evaluation of the trace of the Hamiltonian as follows [104]:

$$a(n) = \text{Tr}[T_n(\mathcal{H})] \approx \frac{1}{R} \sum_{r=0}^{R-1} \langle r | T_n(\mathcal{H}) | r \rangle. \quad (6.3)$$

where the summation is carried out over R random vectors $|r\rangle$, which in an arbitrary basis are defined as: $|r\rangle = \xi_{ri} |c_{i\uparrow}^\dagger\rangle$ with random coefficients ξ_{ri} having a normal random distribution over the interval $[-1, 1]$. The statistical average

over the R vectors of the expectation value approximates the trace in Eq. (6.3). Here the number of vectors R required to perform (6.3) is much lower than the order M of the Hamiltonian (6.1) ($R < M$) [166] and the number of atoms in the disordered region.

The average DOS is calculated by using Eq. (3.8) with the moments obtained using Eq. (6.3). The number of random vectors, R , is taken to be large enough such that the DOS converges. We typically use $R \sim 200$. In order to mimic effectively an infinite region we introduce an absorbing potential operator $\hat{\Gamma}$ at the boundary by following the recipe shown in Section 2.3. It was shown that this absorbing boundary condition could be easily incorporated in the Chebyshev expansion of the Green's function by considering an imaginary damping factor $\hat{\gamma}$, which redefines the recursion formula (2.60) as follows:

$$|\nu_n\rangle = e^{-\hat{\gamma}} (2\mathcal{H}|\nu_{n-1}\rangle - e^{-\hat{\gamma}}|\nu_{n-2}\rangle), \quad (6.4)$$

with the initial conditions $|\nu_0\rangle = |c_{i\uparrow}^\dagger\rangle$ and $|\nu_1\rangle = e^{-\hat{\gamma}}|\nu_0\rangle$. Our calculations for pristine graphene (not presented here) show that we can remove all the finite size interference peaks in the LDOS, appearing due to scattering from the boundaries, without implementing periodic boundary conditions or considering large lattice sizes.

6.3 Results

6.3.1 Vacancies

Within the tight-binding formalism considered here, a vacancy at atomic site i is modeled by setting the on-site energy larger than any energy scale present in the pristine normal state in graphene, $\epsilon_i \gg 3t$. In addition, the corresponding hopping parameters that connect the i -site to its neighbors are set to zero, $t_{ij} = 0$. Our numerical procedure considers any finite concentration of vacancies, defined through the ratio $x_{vac} = N_{vac}/N$, where N is the total number of atomic sites in the junction.

It has been shown that divergences in the DOS are present around the Dirac point when a finite concentration of vacancies are induced in graphene [157]. Here, we calculate the DOS of the graphene Josephson junction while introducing different concentrations of vacancies over the disordered region depicted in Fig. 6.1. The DOS is averaged over different realizations for the configuration of vacancies in order to include all possible scattering and interference processes between the electron/hole wave and the scatterers induced by the missing atoms. In Fig. 6.2 we show the different Andreev peaks that are present in our clean Josephson junction of graphene (bottom curve). The electron and hole wave

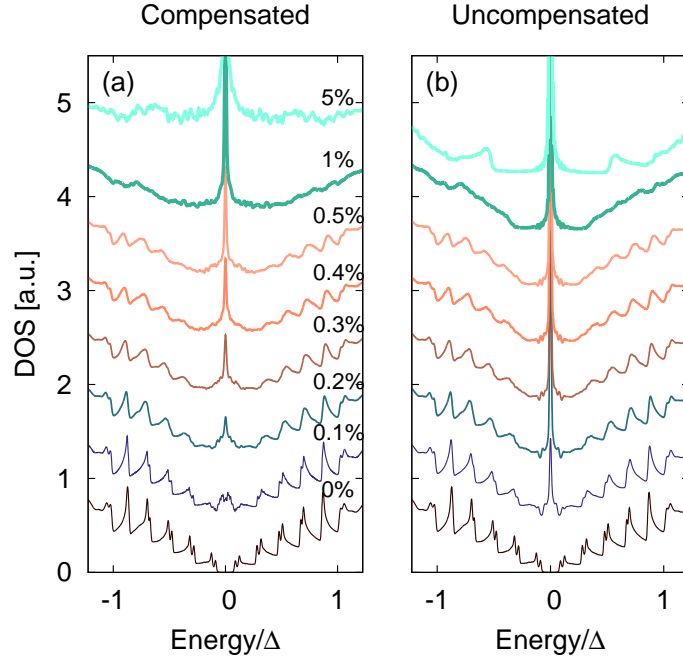


Figure 6.2: DOS for a graphene Josephson junction considering different concentration of vacancies $x_{vac} = N_{vac}/N = 0, 0.1, 0.2, 0.3, 0.4, 0.5, 1$ and 5% from bottom to top. Energy scale is normalized to the bulk value of the order parameter (Δ) in the graphene superconducting regions. Two cases are considered, according to the compensation in the distribution between the two sublattices: (a) completely compensated where vacancies are distributed equally in the two sublattices and (b) completely uncompensated where vacancies are randomly present only in one of the sublattices.

are scattered by the N/S interface and interfere, giving rise to the well known Andreev peaks. Note that because the chemical potential in the junction is at the Dirac point, the Andreev peaks show the specific energy dependence in the graphene junctions, i.e. traveling modes with a gapped spectrum versus bound states with an ungapped spectrum as observed in conventional S/N/S junctions. As we can see clearly in Fig 6.2, as the concentration of impurities increases, the Andreev peaks are progressively suppressed. Notice that the lowest energy peaks are the first to disappear as the scattering probability for long paths between the interfaces becomes higher, affecting lower energy states, when compared to short paths, which contribute to higher subgap energy states. As the concentration is increased above $x > 0.5\%$, traces of the Andreev reflection processes on the DOS vanish.

Selective dilution of the vacancies in the different sublattice sites has been

shown to induce different zero modes in the DOS [157, 167]. For instance, complete dilution of the vacancies in one of the sublattices, or complete uncompensated dilution, leads to the opening of a gap around the zero mode at the Dirac point and whose magnitude is proportional to the vacancy concentration. On the opposite, complete compensated dilution brings an increase of the spectral weight for energies surrounding the Dirac point. We have investigated both cases and found slight differences in the DOS around the Fermi level, which are more remarkable for larger vacancy concentrations, $x > 0.5\%$ (see Fig. 6.2). In order to further clarify the contrast between the compensated and uncompensated cases we show in Fig. 6.3 the average critical current density across the junction as a function of vacancy concentration. Note that the current is averaged over the junction width and over impurity configurations. As we can observe both cases lead to different power-law suppression of the the critical current. For instance, the suppression of the current goes according to $J_c \sim x^{-1.8}$ for uncompensated dilutions of the vacancy configurations. This agrees with the fact that a gap of energy scale $E^2 \sim x_{vac}$ is induced for complete uncompensated dilution of vacancies in graphene [157]. On the other hand, vacancies diluted in both sublattices still show a strong suppression of the supercurrent but weaker than the uncompensated case. As an interesting fact, we note that by placing these vacancies in pairs of bounded atomic sites (bivacancies), we can observed that the suppression is much weaker than in previous cases. The slow linear suppression of the supercurrent in the presence of bivacancies is due to the absence of inter-valley scattering, as was already reported previously for this type of atomic-scale defects [159].

6.3.2 Ripples: Gaussian bumps

We next analyze the effects of inhomogeneous strain over the disordered area in the graphene Josephson junction. For this purpose, we model the ripples in graphene as smooth bumps where the out of plane deformation is described by a Gaussian function. It has been theoretically shown that a six-fold spatially symmetric pseudo-magnetic fields, with alternating sign, emerges from this strain configuration [164, 168, 169].

The Gaussian deformation is introduced in the tight-binding description of Eq. (6.2) by the strained hopping parameter:

$$t_{ij} = \gamma_0 \exp^{-3.37(\frac{l_{ij}}{a_0} - 1)} \quad (6.5)$$

where $\gamma_0 = 2.7\text{eV}$ and $a_0 = 1.42\text{\AA}$ are the unstrained hopping and lattice parameter, respectively, while l_{ij} is the strained distance between nearest-neighbors i

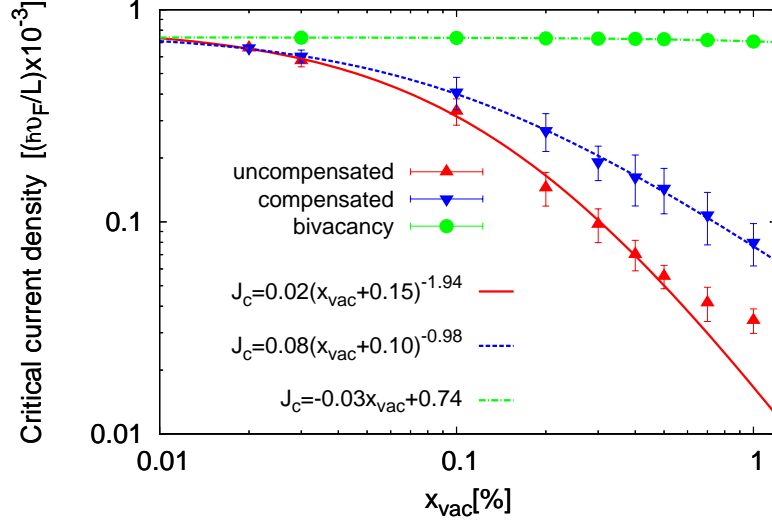


Figure 6.3: Average critical current density in a graphene Josephson junction for different concentrations of vacancies, diluted randomly over both sublattices (compensated), or over a single sublattice (uncompensated), or over two-coupled sublattices (bivacancy). The continuous lines correspond to a least squares fit to $f(x) = a(x + b)^c$ and $g(x) = ax + b$.

and j . The corresponding out of plane deformation is given by a Gaussian function as follows:

$$Z(R_{ij}) = Z_0 \exp^{-|R_{ij}|^2/2\varepsilon^2} . \quad (6.6)$$

where $R_{ij} = r_{ij} - R_0$ is the in-plane atomic position with respect to the center of the Gaussian, R_0 . It is important to mention that the Gaussian width parameter ε is constrained here, such that $Z(R_{ij}) \approx 0$ in the clean interface regions (see Fig. 6.1). Once the width is fixed, the height parameter Z_0 is adjusted according to a desired maximal strain. Since we know from the continuum model how the strength of the pseudomagnetic field depends on the parameters of the Gaussian, we considered different configurations for the size and the number of Gaussian bumps inside the junction (see Fig. 6.4). As a particular case, we have included in Fig. 6.4 an arrangement of triangular bumps made from a superposition of four Gaussians in a triangular configuration, where three are centered in equidistant vertices while the last is placed a distance d from the vertices in the middle of the triangle. This particular strain has been inspired by a previous theoretical study where a nonuniform deformation is engineered by depositing graphene

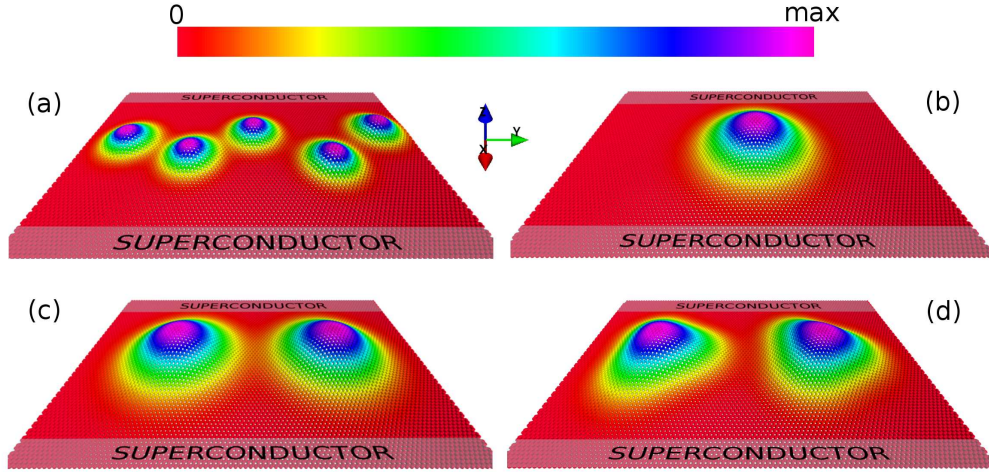


Figure 6.4: Strained graphene Josephson junction with different configurations of Gaussian bumps. Panels (a)-(c) show isolated Gaussian bumps while (d) corresponds to an arrangement of four Gaussian bumps in a triangular configuration.

on a substrate decorated with nanopillars set in a triangular configuration [170]. The corresponding pseudomagnetic fields emerging from these deformation exhibit a non-trivial symmetry, consisting of larger regions with an almost constant pseudo-magnetic field, when compared to the sixfold symmetric fields generated by isolated Gaussian bumps. In order to investigate the effect of ripples on Andreev scattering in the junction we calculated the average DOS for the different configurations of Gaussian bumps shown in Fig. 6.4. These results are shown in Fig. 6.5(a)-(d) for different values of the maximum strain: 0%, 5%, 10% and 20%. The Andreev states seen in Fig. 6.5(a) start to be affected by the presence of the Gaussian bumps even for the lowest values of the strain. Particularly, high-energy Andreev peaks are mainly suppressed for the case of high density of Gaussian bumps depicted in Fig. 6.4(a). This suggests that short paths are influenced more by the pseudomagnetic field than the long paths, which contribute to the low energy spectrum.

Alternatively, the configuration with a single Gaussian bump, shown in Fig. 6.4(b), for which the DOS is presented in Fig. 6.5(b) shows that high-energy Andreev peaks remain conserved despite the fact that the pseudo-magnetic field is supposed to be stronger over a wider region. At low energies, sharp peaks appear, and the quasi-particle gap starts to close.

The next two cases, shown in Figs. 6.4(c) and (d) and Figs. 6.5(c) and (d), reveal an interplay between the size of the Gaussian bump and the strength of the pseudo-magnetic field. As seen previously, the high energy peaks are the

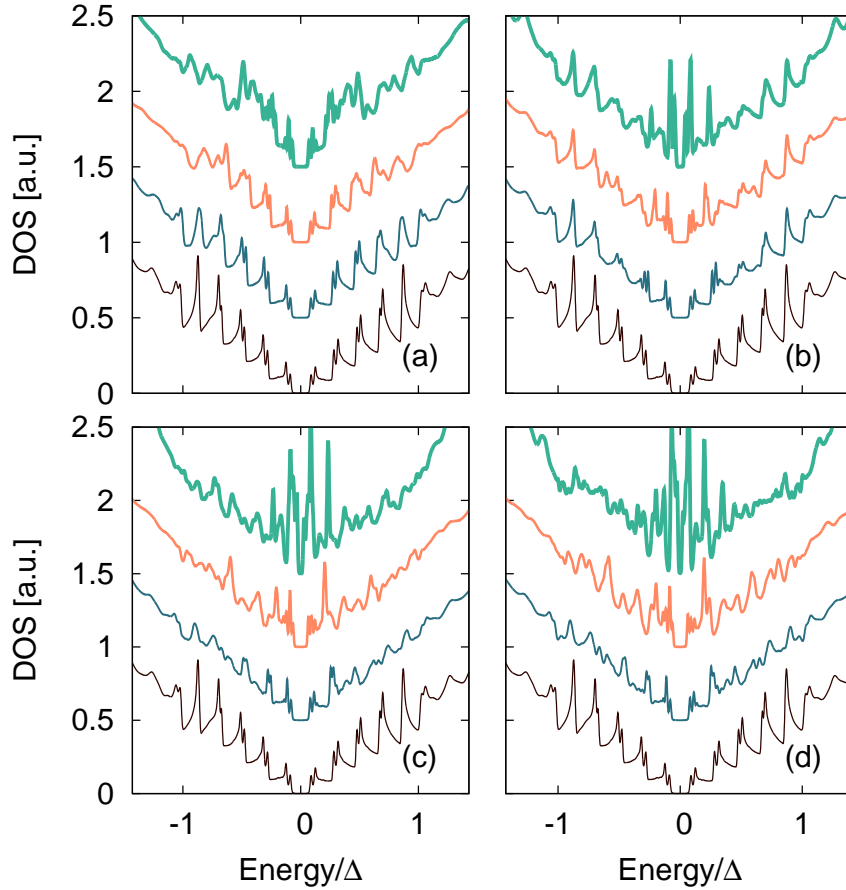


Figure 6.5: DOS for a graphene Josephson junction for the different strain configurations shown in Fig. 6.4. Panels from left to right correspond to cases from top to bottom shown in Fig. 6.4, respectively. Areas delimited by subsequent curves have been filled in order to present a better contrast between the Andreev peaks for deformations with the maximum strain increasing from 0% to 5%, 10% and 20% (bottom to top).

first to be affected as the strain is increased. At low energies, Landau level-like peaks appear and the gap observed for the clean system closes. Because of the oscillating pseudo-magnetic field, a combination of snake-like states and pseudo-Landau levels, appear where the field vanishes or is maximal. The existence of extended regions with large pseudo-magnetic fields, will act as a pseudo-magnetic barrier for the electron or hole quasiparticles propagating in the junction. As a consequence, although the time-reversal symmetry is not broken, it is expected that the supercurrent is suppressed and will flow only as edge states near the boundaries [128]. We next investigate the Josephson current flowing through

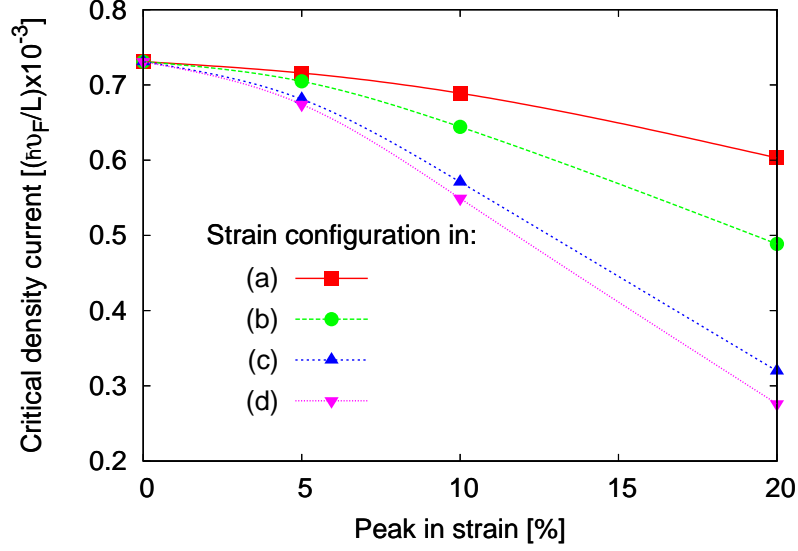


Figure 6.6: Average critical current density in strained Josephson junctions as a function of maximal strain for the strain configurations depicted in Figs. 6.4(a)-(d).

the strained junctions in Fig. 6.6, where we present the average critical current density as a function of the maximum strain applied in each configuration. We find a suppression of the critical current as the strain is increased. In particular, this suppression is stronger for the configurations shown in Figs. 6.4(c) and (d) when compared with the single bump case, Fig. 6.4(b), and the many smaller bumps, Fig. 6.4(a). As suggested previously, these results can be explained by noticing that the current is more effectively suppressed in the cases in which the pseudo-magnetic field is larger over a more extended area, thus providing a better magnetic barrier. Although the size of the bump in case (d) is the same as the one in case (c), the current is further suppressed because the triangular bump induces larger regions with pseudo-magnetic fields with the same sign, although the average field is zero.

6.3.3 Charged impurities

Finally, we investigate the effect of scattering due to the presence of impurities on the diffusion of Andreev pair in graphene Josephson junctions. It is well-known that the presence of these types of impurities may induce local charged puddles in graphene, which can be emulated through spatial fluctuations of the Fermi energy around the Dirac point. These fluctuations are modeled here by means of a random superposition of N_{imp} potentials with a Gaussian-like spatial

dependence. Thus, we assume that the proximity of a single charged impurity is reflected in the parameters of a Gaussian potential such that on-site energies of carbon atoms in the disordered region are given as follows [171]:

$$\epsilon_i = \sum_{j=1}^{N_{imp}} V_j \exp\left(-\frac{|r_i - R_j|^2}{2\varepsilon^2}\right) \quad (6.7)$$

where V_j and ε correspond to the amplitude and range of a single Gaussian potential centered at the atomic position R_j , respectively. These on-site potentials as described by Eq. (6.7) are introduced in our formalism described by the Hamiltonian (6.2) but we constrain their scope to $\varepsilon < L, W$ such that they vanish in the interface strips where the Fermi level is pinned at the Dirac point.

In order to characterize the effect of this sort of disorder we follow the recipe proposed in previous works [171, 172] where the mean-free path is considered as being inversely proportional to the following parameter:

$$\kappa_0 \propto \left(\frac{V_i}{t}\right)^2 x_{imp} \kappa^2 \quad (6.8)$$

where V_i/t is amplitude of the random potential in units of the hopping parameter while the ratio of the number of impurities and the total number of atoms in the junction corresponds to the concentration of impurities $x_{imp} = N_{imp}/N$. The averaged charge density per impurity atom is described by the factor κ according to:

$$\kappa = \frac{1}{N_{imp}} \sum_j^{N_{imp}} \sum_i^N \exp\left(-\frac{|x_i - x_j|^2}{2\varepsilon^2}\right) \quad (6.9)$$

For practical purposes, we consider the same amplitude for all potentials in Eq. (6.7), *i.e.* $|V_j| = V$ for all j . In addition, for a given value of the Gaussian width ε , we fixed the maximum of the Gaussian, V , such that the density of charges obtained from Eq. (6.9) is the same for the different values of ε considered here. This allows us to make a more clear discussion about the effect of the Gaussian potential, mainly of its height and width parameters, as long as the total charge density is kept fixed under a constant concentration of vacancies. We consider two separate cases. First, in the presence of electron and hole puddles, the total charge density is zero, meaning that the number of electron and hole-doped Gaussians is equal. We next investigate the presence of charged impurities of the same type, *i.e.* electron-doped Gaussians, in which case the charge density will increase as the concentration of impurities increases.

We first present our results for the electron-hole charge puddles. In Figs. 6.7(a)-(c) we show the average DOS in a graphene Josephson junction with doping inhomogeneity profiles given by Eq.(6.7) for three different cases according to the size of the Gaussian potential induced by single impurities. As in the previous disorder cases, the DOS is averaged over different realizations of the impurity configurations. The most trivial case, where $\varepsilon/a = 0.1 \ll 1$, is depicted in Fig. 6.7(a). In this limit, which resembles the typical Anderson disorder model, we can observe that the effect of increasing the concentration of impurities x_{imp} leads to a suppression of the Andreev bound states. Despite that this on-site defect is similar to the case of vacancies (in the limit of large V) we can see that when comparing with Fig. 6.2 the dispersion mechanism acts differently in the two cases, as lower energy Andreev states are preserved even for the highest values of x_{vac} in Fig. 6.7(a).

Next we proceed to a larger $\varepsilon/a = 0.5$, a value still smaller than the lattice parameter. In this situation, we see in Fig. 6.7(b) that Andreev bound states are affected much more strongly as inter-valley scattering is expected to become more pronounced. It is clearly seen that the lower energy gap disappears in the first place as the concentration of impurities is increased. This is similar to what was observed for vacancies, with the difference that the quasiparticle gap does seem to be completely suppressed as the impurity concentration increases.

Contrary to the previous cases, when $\varepsilon > a$, the influence of disorder on the Andreev states is weak. As the potential profile becomes smoother on the scale of the lattice parameter, inter-valley scattering is suppressed, thus having a weak influence on the average DOS in the junction, as seen in Fig. 6.7(c). In order to verify the insights given by the change in the Andreev levels seen in the averaged DOS, we plot in Fig. 6.8 the average critical current density as a function of impurity concentration for different values of ε . First, in panel Fig. 6.8(a), the electron-hole puddles scenario is considered. In this case the current is suppressed for all ranges of the potential profiles, with a much stronger effect when $\varepsilon \leq a$, and a very weak effect when $\varepsilon > a$. The case $\varepsilon/a = 0.5$ deserves particular attention as the current becomes strongly suppressed when the impurity concentration is increased, confirming the strong suppression of the Andreev peaks observed in the averaged DOS. This effect was investigated experimentally in graphene Josephson junctions in the long-junction limit [67] and presence of electron-hole puddles was given as an explanation for the strong suppression of the supercurrent at charge neutrality. As shown here, we only observe a strong suppression when the charge scatterers are short-range.

In addition to the charge puddles case, the effect of an impurity distribution with positive charge, inducing an average finite doping in graphene, is also studied. The average critical current density for this scenario is presented in Fig. 6.8(b). Here the dependence of the current is not monotonic as a function of

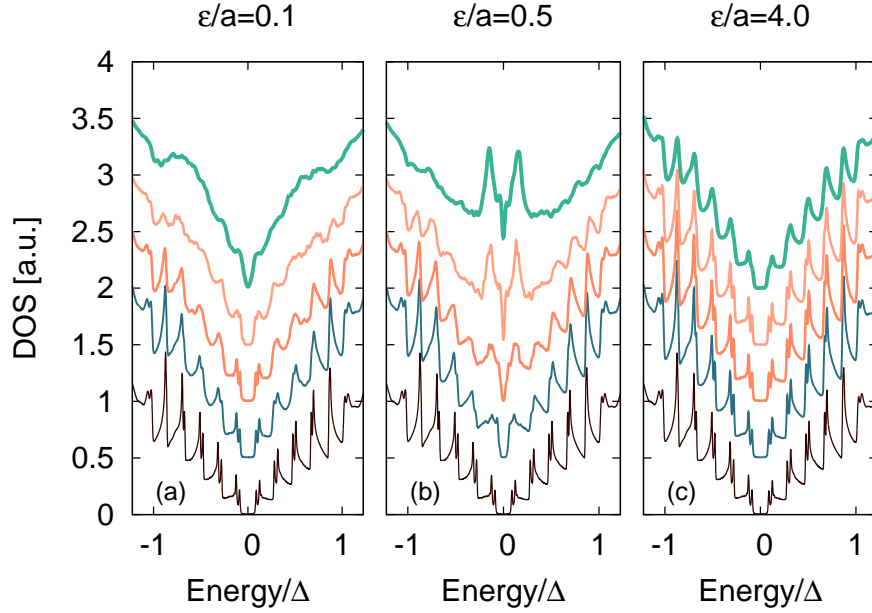


Figure 6.7: (Color online) Average DOS for disordered graphene Josephson junctions, considering impurity scattering potentials with different ranges, $\varepsilon/a = 0.1, 0.5$ and 4.0 . The area between the curves has been filled in order to have a better contrast for lines corresponding to different impurity concentrations. Different values of the impurity concentration considered inside the panels are $x_{imp} = 0\%, 1\%, 2\%, 3\%$ and 5% , from bottom to top.

ε . The overall tendency is for the supercurrent to be enhanced since finite doping brings the Fermi level away from the Dirac point. On the other hand, the presence of short-range scatterers will also generate inter-valley scattering events, thus suppressing the current. Therefore we observe two separate regimes, depending on whether $\varepsilon < a$ or $\varepsilon \geq a$. For $\varepsilon = 0.1a$ and $0.5a$, the current is suppressed even for low impurity concentration, signaling the fact that inter-valley scattering is the main contribution, larger for $\varepsilon = 0.5a$. If $\varepsilon \geq a$, at low impurity concentration the supercurrent is increasing due to an increase in the average doping but depending on the inter-valley scattering probability it will be eventually suppressed, more for $\varepsilon = a$ than $\varepsilon = 4a$.

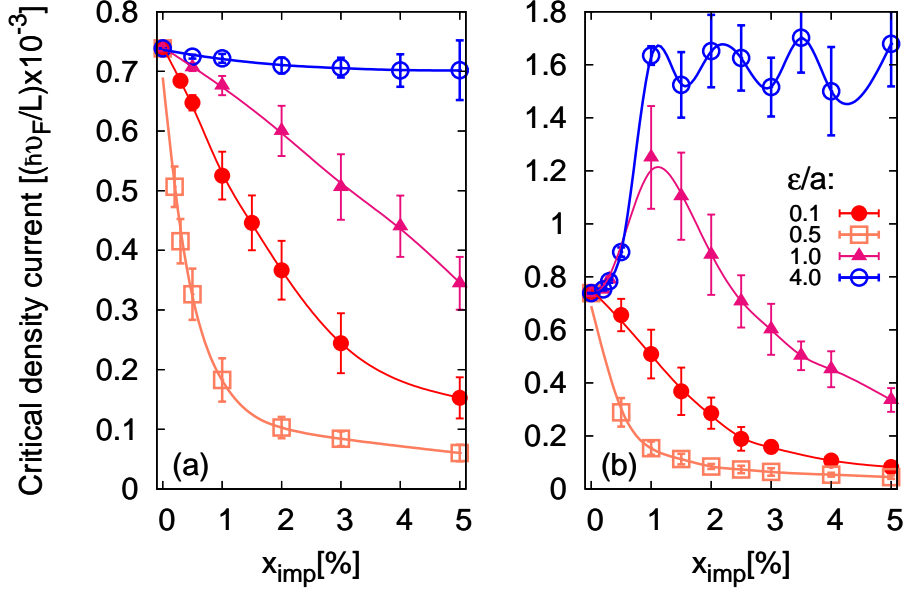


Figure 6.8: (Color online) Average critical current density in a graphene Josephson junction as a function of the impurity concentration x_{imp} for different widths of the Gaussian potential induced by isolated impurities. Equal number of electron and hole-like potentials are considered in panel (a) while only electron-like potentials are assumed in (b) leading to a inhomogeneous but finitely doped junction.

6.4 Conclusion

In conclusion, by using a numerical tight-binding approach, we described various disorder scenarios in graphene Josephson junctions near charge neutrality. We investigated both the disappearance of the multiple Andreev reflection peaks in the junction and the suppression of the Josephson current. We observed that the supercurrent is most strongly suppressed in the presence of vacancies or resonant impurities, e.g. adsorbed hydrogen atoms. In this case, the presence of strong inter-valley scattering destroys the interference of time reversed electron-hole pairs which undergo Andreev reflections at the N/S interfaces. As a test, we show that when the vacancies come in pairs, and thus the sub-lattice symmetry is not being broken, the supercurrent is very weakly suppressed.

Another scattering mechanism is given by the presence of ripples. We show that although there should be no inter-valley scattering in this case, Gaussian bumps will act as pseudo-magnetic barriers, thus suppressing the supercurrent. The larger the regions with finite pseudo-magnetic fields, the more efficient the

scattering will be.

A third disorder scenario involves the presence of charged impurities, which are modeled as variations of the local potential. We show that in the presence of electron-hole charge puddles, the supercurrent is always suppressed, but the strongest effect is obtained when the range of the potential disorder is very small, thus inducing significant inter-valley scattering. When the impurities only dope with electrons, we observe an interplay between an enhancement of the current due to the shift of the Fermi energy away from the Dirac point, and a suppression by short range scatterers due to inter-valley scattering.

Publication The results of this chapter will be published as:

- W. A. Muñoz, L. Covaci and F. M. Peeters *Disordered graphene Josephson junctions*, Phys. Rev. B , (2014) (9 pages).

7

Summary

7.1 Concluding remarks of the thesis

In the present thesis, we theoretically investigated intrinsic and proximity-induced superconducting correlations in single and multilayer graphene. In order to describe inhomogeneous superconductivity in these lattice structures we solved self-consistently the Bogoliubov-de Gennes equations within a tight-binding formalism. For our study we used an efficient numerical method for the calculation of Green-Gor'kov functions through an expansion in terms of Chebyshev polynomials. Significant speed-up is achieved for the present method by implementing massive parallel algorithms in Graphic Processing Units (GPUs). This allows us to solve efficiently systems described by matrices with large sizes ($\sim 10^4 - 10^6$ atoms) as this corresponds to the typical dimension of the Hamiltonian matrix for multilayer graphene structures, where direct diagonalization is not suitable.

In chapter 3, we performed a study of the proximity effect and the superconducting current in a normal-superconducting-normal single and bilayer graphene Josephson junction. Proximity is emulated through the self-consistent calculation of the pair amplitude along the junction, where the Fermi level is shifted in the normal (non-superconducting) region. For large and moderate doping, where BLG seems to behave similar to SLG, the characteristic leakage length is found to match with the SLG Josephson junction case. However, we observed that for doping levels below the interlayer coupling energy, the pair amplitude behaves quite differently from SLG case. Due to the polarization in the local density of

states in BLG between dimer and non-dimer sites, we found two different leaking distances. As a consequence, we observed that around the Dirac point the current-phase relation differ from SLG where the critical current is suppressed for the BLG case. Broken space inversion symmetry was also considered in our work and it is shown that an electric field perpendicular to the bilayer suppresses the current in short junction where the length of the junction (L) is comparable to the Fermi length (λ_F). For the $L < \lambda_F$ regime, where doping effects from the contact are important, we found an enhancement of the current as the electric field increases.

In chapter 4, we used the same method to solve self-consistently for the s -wave pair order parameter in a rhombohedral (ABC) and Bernal (ABA) multilayer graphene. We examined the effect of both stacking configurations and found opposite bulk/surface behavior of the order parameter. Surface superconductivity is robust for ABC stacked multilayer graphene even at very low pairing potentials for which the order parameter vanishes in the bulk. This is in contrast to Bernal stacked multilayer graphene, where we find that the order parameter is always suppressed at the surface and that there exists a critical value for the pairing potential below which no superconducting order is achieved. We also considered different doping scenarios and find that homogeneous doping strongly suppresses surface superconductivity while a non-homogeneous field-induced one has a much weaker effect on the superconducting order parameter in rhombohedral multilayer graphene. For those multilayer structure with hybrid stacking (ABC and ABA), we find that when the thickness of each region is small (few layers), rhombohedral surface superconductivity survives throughout the bulk due to the proximity effect between ABC/ABA interfaces where the order parameter is enhanced.

In chapter 5, we presented a 3-dimensional description of a Josephson junction made of two superconducting contacts linked weakly by a non-intrinsically superconducting multilayer graphene substrate. Both Bernal (ABA) and rhombohedral (ABC) stacking are considered and we found a strong dependence of the pair leaking on the type of stacking. For instance, the amplitude of the pair correlation function shows a polarization between dimer and non-dimer atoms, which is more pronounced for rhombohedral configuration. Despite the fact that proximity effect in non-dimer sites is enhanced when compared to single layer graphene, we find that the Josephson current is suppressed. In fact, the spatial distribution of the supercurrent shows that for ABA stacking the current flows mostly in the top-most layers while for ABC stacking the current flows throughout the whole structure.

In chapter 6, we investigated the effect of disorder on the Andreev states and the Josephson current in a graphene Josephson junction. We considered different disorder scenarios like vacancies, ripples and charged impurities. In presence of

vacancies, for instance, we observed the disappearance of the multiple Andreev peaks and suppression of the Josephson current. This follows from the intervalley scattering induced by this resonant impurities which destroys the quantum interference between the time-reversal trajectories of the Andreev-reflected electron-hole pair. The situation is similar under another scattering mechanism induced by the presence of ripples, which do not mix valleys but, where we have also observed the suppression of the supercurrent. This suggests that the presence of the ripples act as pseudo-magnetic barriers on the electron and holes trajectories. Finally, we considered the case where the presence of charged impurities induces local variation in the Fermi energy named charged puddles. We examined the effect of both electron-hole and only electron charged puddles and found that for the former case the supercurrent is always suppressed with strong effect for short-range potential where intervalley scattering seems to be important. The later case shows an enhancement of the supercurrent since Fermi level in the junction is shifted away the neutrality point as a consequence of the non-zero averaged doping induced for the electron charged puddles. Suppression of the supercurrent is found in this case only for short-range potential due to the intervalley scattering.

7.2 Future prospects

In chapter 3 we considered exclusively clean graphene systems. Nonetheless, we have demonstrated in chapter 6 that it is possible to extend our calculations to disordered graphene. We expect that disorder will influence differently the single and bilayer cases since the LDOS modification near impurities is different in the two cases. Also, in bilayer graphene, one can have different levels of disorder in the two layers, for example hydrogenation at one side, which will make bilayer distinct from single layer. It is expected that different effects on the Andreev states emerge from the presence of charged impurities since Klein tunneling in BLG is converted to total reflection instead of total transmission as was found in SLG [173].

In chapter 4 we discussed about possible superconducting correlations in multilayer graphene with different stacking configuration. Our calculations were made under the assumption of the existence of a *s*-wave coupling. It will be interesting to continue similar calculations but assuming *p*-wave coupling. The reason is that there are several hints suggesting that magnetism may play some role in the superconducting signal obtained for HOPG samples [51, 52]. In analogy with rhombohedral multilayer graphene, the electronic band structure shows the presence of flat band close to the Fermi level for slightly twisted bilayer graphene [174]. According to our findings in chapter 4, van Hove singularity

near the Fermi energy, which is a clear sign of flattening of the band, may provide some enhancement in the electronic correlations in twisted bilayer graphene which in turn can trigger high critical temperature superconductivity.

Finally, in chapter 5 we numerically studied Josephson junctions of a multilayer graphene. Numerical calculations can be performed including a bottom gate which dopes only the lower layers as in the experimental setup of Ref. [122]. In order to do that, screening effects have to be included such that a proper charge distribution in the layers is accounted for.

8

Samenvatting

8.1 Overzicht van de thesis

In dit proefwerk berekenen we de intrinsieke en nabijheid geïnduceerde supergeleidende correlaties in enkele en multilaag grafen. Om inhomogene supergeleiding in deze materialen te kunnen beschrijven, hebben we zelfconsistent de Bogoliubov-de Gennes vergelijkingen opgelost binnen een tight-binding formalisme. In onze studie hebben we een efficiënte numerieke methode gebruikt om de Green-Gorkov functies te berekenen door ze te ontwikkelen in termen van Chebyshev polynomen. Voorts werden significanten snelheidswinsten geboekt door deze theorie parallel te implementeren op Graphic Processing Units (GPUs). Dit laat ons toe om grote systemen ($10^4 - 10^6$ atomen) te simuleren. Bij deze grootte orde is het niet mogelijk om voor multilaag grafen de Hamiltoniaan rechtstreeks te diagonaliseren.

In hoofdstuk 3 hebben we een studie uitgevoerd om het nabijheidseffect en de supergeleidende stroom in een normaal-supergeleidend-normaal junctie te berekenen op enkele en bilag grafen. Het nabijheidseffect manifesteert zich in zelf consistente berekeningen van de paar amplitude langs de junctie waar het Fermi niveau bepaald wordt door het niet supergeleidende deel. Indien het systeem gemiddeld tot sterk gedoopt wordt, blijkt dat bilag grafen (BLG) zich gelijkaardig gedraagt als monolaag grafen (SLG), de karakteristieke leklengte komt overeen met een SLG Josephson junctie. We observeerden echter dat indien het doping niveau onder de interlaag koppeling energie ligt, de paar ampli-

tude zich vrij anders gedraagt dan voor het SLG geval. Door de polarizatie van de lokale toestandsdichtheid in de BLG tussen de gedempte en vrije toestanden, vonden we twee verschillende lek lengtes voor beide toestanden. Bijgevolg observeerden we dat rond het Dirac punt de stroom-fase relatie verschilt van SLG. Bij BLG is de kritische stroom onderdrukt ten opzichte van de SLG. We onderzochten ook een gebroken ruimtelijke inversie symmetrie en toonden aan dat een elektrisch veld loodrecht op de bilaag de stroom onderdrukt indien de junctie kort is, i.e. de lengte (L) is vergelijkbaar met de Fermi lengte (λ_f). Voor het $L < \lambda_f$ regime, waar effecten van contactdoping belangrijk zijn, vonden we een versterking van de stroom als het elektrisch veld verhoogd werd.

In hoofdstuk 4 gebruikten we dezelfde methoden om de s-golf paar orde parameter in een rhombohedraal (ABC) en Bernal (ABA) multilaag grafeen te bestuderen. We onderzochten het effect van beide stapelconfiguraties en vonden een tegenovergestelde bulk/oppervlakte gedrag in de ordeparameter. Oppervlakte superconductiviteit is robust in ABC multilaag grafeen zelfs bij kleine paringspotentialen waarvoor de ordeparameter verdwijnt in de bulk. In tegenstelling tot Bernal gestapeld multilaag grafeen, waar we vinden dat de ordeparameter altijd onderdrukt wordt aan het oppervlak en dat er een kritische waarde bestaat voor de potentiaal waaronder geen supergeleidende orde wordt bereikt. We onderzochten ook verschillende manieren van doperen en vonden dat homogene doping de oppervlakte supergeleiding sterk onderdrukt terwijl niet-homogene doping die geïnduceerd is door een veld een veel zwakker effect heeft op de supergeleidende ordeparameter in ABC multilaag grafeen. Voor deze multilaag structuren met een hybride stapeling (ABC en ABA), vinden we dat, voor een kleine dikte van iedere regio (enkele lagen), rhombohedraal oppervlakte supergeleiding in de bulk overleeft door het proximity effect tussen ABC / ABA tussenvlakken die de orde parameter versterken.

In hoofdstuk 5 presenteren we een driedimensionale beschrijving van een Josephson junctie die gemaakt is van twee supergeleidende contacten zwak verbonden door een niet-intrinsiek supergeleidend multilaag grafeen substraat. Beide Bernal (ABA) en rhombohedraal (ABC) stapel wijzen zijn bestudeerd en we vonden dat de mate waarin paarlekking optreedt sterk afhankelijk is van de stapelwijze. Zo vertoont bijvoorbeeld de amplitude van de paarcorrelatie functie een sterke polarizatie tussen de boven en naast elkaar gestapelde atomen, wat het sterkst duidelijk is bij de ABC configuratie. Ondanks het feit dat het nabijheidseffect in de boven elkaar gestapelde toestanden versterkt is in vergelijking met SLG, vinden we dat de Josephson stroom onderdrukt is. In feite toont de ruimtelijke distributie van de superstroom dat voor ABA stapeling de stroom hoofdzakelijk in de bovenste lagen stroomt terwijl dit voor ABC stapeling in de hele structuur gebeurt.

In hoofdstuk 6 onderzoeken we het effect van wanorde op de Andreev toes-

tanden en de Josephson stroom in een grafeen Josephson junctie. We beschouwen verschillende wanorde scenarios zoals gaten, rimpeld en geladen onzuiverheden. In de nabijheid van gaten, bijvoorbeeld, observeerden we dat verschillende Andreev pieken verdwenen en dat de Josephson stroom onderdrukt werd. Dit volgde uit de intervallei verstrooiing geïnduceerd door resonante onzuiverheden die de kwantum interferentie tussen de tijdsomgekeerde paden van de Andreev gereflecteerde elektron-gat paren vernietigde. De situatie is gelijkaardig voor andere verstrooiingsmechanismen zoals rimpels, waarvoor de valleien niet gemengd worden, waarvoor we vonden dat de superstroom onderdrukt werd. Dit suggereert dat de aanwezigheid van rimpels zich uitdrukt als pseudo-magnetische barrières voor de elektron en gat paden. Uiteindelijk beschouwden we ook het geval waarvoor de aanwezigheid van geladen onzuiverheden lokale variaties in de Fermi energie induceren. Deze variaties noemen we geladen poelen. We onderzochten het effect van elektron-gat en enkel elektron poelen en vonden dat voor de eerste de superstroom altijd onderdrukt wordt als gevolg van het sterke effect voor korte dracht potentialen waarvoor de intervallei verstrooiing belangrijk begint te worden. In het andere geval vinden we een versterking van de superstroom omdat het Fermi niveau in de junctie opgeschoven is, weg van het neutraliteitspunt als gevolg van de eindige gemiddelde doping geïnduceerd voor de elektronpoelen. Onderdrukking van de superstroom wordt in dit geval gevonden voor korte-dracht potentialen als gevolg van intervallei verstrooiing.

Bibliography

- [1] K. S. Novoselov, A. K. Geim, S. V. Morozov, D. Jiang, Y. Zhang, S. V. Dubonos, I. V. Grigorieva, and A. A. Firsov, “Electric Field Effect in Atomically Thin Carbon Films,” *Science*, vol. 306, pp. 666–669, Oct. 2004. PMID: 15499015.
- [2] P. R. Wallace, “The Band Theory of Graphite,” *Phys. Rev.*, vol. 71, pp. 622–634, May 1947.
- [3] G. W. Semenoff, “Condensed-Matter Simulation of a Three-Dimensional Anomaly,” *Phys. Rev. Lett.*, vol. 53, pp. 2449–2452, Dec. 1984.
- [4] B. C. Brodie, “On the Atomic Weight of Graphite,” *Phil. Trans. R. Soc. Lond.*, vol. 149, pp. 249–259, Jan. 1859.
- [5] H. P. Boehm, A. Clauss, G. O. Fischer, and U. Hofmann, “Das Adsorptionsverhalten sehr dünner Kohlenstoff-Folien,” *Z. anorg. allg. Chem.*, vol. 316, pp. 119–127, July 1962.
- [6] A. J. Van Bommel, J. E. Crombeen, and A. Van Tooren, “LEED and Auger electron observations of the SiC(0001) surface,” *Surface Science*, vol. 48, pp. 463–472, Mar. 1975.
- [7] J. T. Grant and T. W. Haas, “A study of Ru(0001) and Rh(111) surfaces using LEED and Auger electron spectroscopy,” *Surface Science*, vol. 21, pp. 76–85, June 1970.
- [8] K. S. Novoselov, A. K. Geim, S. V. Morozov, D. Jiang, M. I. Katsnelson, I. V. Grigorieva, S. V. Dubonos, and A. A. Firsov, “Two-dimensional gas of massless Dirac fermions in graphene,” *Nature*, vol. 438, pp. 197–200, Nov. 2005.
- [9] A. H. Castro Neto, F. Guinea, N. M. R. Peres, K. S. Novoselov, and A. K. Geim, “The electronic properties of graphene,” *Rev. Mod. Phys.*, vol. 81, pp. 109–162, Jan. 2009.

-
- [10] S. Das Sarma, S. Adam, E. H. Hwang, and E. Rossi, “Electronic transport in two-dimensional graphene,” *Rev. Mod. Phys.*, vol. 83, pp. 407–470, May 2011.
- [11] A. F. Young and P. Kim, “Quantum interference and Klein tunnelling in graphene heterojunctions,” *Nat. Phys.*, vol. 5, pp. 222–226, Mar. 2009.
- [12] Y. Zhang, Y.-W. Tan, H. L. Stormer, and P. Kim, “Experimental observation of the quantum Hall effect and Berry’s phase in graphene,” *Nature*, vol. 438, pp. 201–204, Nov. 2005.
- [13] K. S. Novoselov, E. McCann, S. V. Morozov, V. I. Fal’ko, M. I. Katsnelson, U. Zeitler, D. Jiang, F. Schedin, and A. K. Geim, “Unconventional quantum Hall effect and Berry’s phase of 2π in bilayer graphene,” *Nat. Phys.*, vol. 2, pp. 177–180, Mar. 2006.
- [14] S. V. Morozov, K. S. Novoselov, M. I. Katsnelson, F. Schedin, L. A. Ponomarenko, D. Jiang, and A. K. Geim, “Strong Suppression of Weak Localization in Graphene,” *Phys. Rev. Lett.*, vol. 97, p. 016801, July 2006.
- [15] N. Levy, S. A. Burke, K. L. Meaker, M. Panlasigui, A. Zettl, F. Guinea, A. H. C. Neto, and M. F. Crommie, “Strain-Induced Pseudo-Magnetic Fields Greater Than 300 Tesla in Graphene Nanobubbles,” *Science*, vol. 329, pp. 544–547, July 2010. PMID: 20671183.
- [16] J. B. Oostinga, H. B. Heersche, X. Liu, A. F. Morpurgo, and L. M. K. Vandersypen, “Gate-induced insulating state in bilayer graphene devices,” *Nat Mater*, vol. 7, pp. 151–157, Dec. 2007.
- [17] A. K. Geim, “Nobel Lecture: Random walk to graphene,” *Rev. Mod. Phys.*, vol. 83, pp. 851–862, Aug. 2011.
- [18] Z. K. Tang, L. Zhang, N. Wang, X. X. Zhang, G. H. Wen, G. D. Li, J. N. Wang, C. T. Chan, and P. Sheng, “Superconductivity in 4 Angstrom Single-Walled Carbon Nanotubes,” *Science*, vol. 292, pp. 2462–2465, June 2001. PMID: 11431560.
- [19] M. Kociak, A. Y. Kasumov, S. Guéron, B. Reulet, I. I. Khodos, Y. B. Gorbatov, V. T. Volkov, L. Vaccarini, and H. Bouchiat, “Superconductivity in Ropes of Single-Walled Carbon Nanotubes,” *Phys. Rev. Lett.*, vol. 86, pp. 2416–2419, Mar. 2001.
- [20] N. B. Hannay, T. H. Geballe, B. T. Matthias, K. Andres, P. Schmidt, and D. MacNair, “Superconductivity in Graphitic Compounds,” *Phys. Rev. Lett.*, vol. 14, pp. 225–226, Feb. 1965.

- [21] J. Nagamatsu, N. Nakagawa, T. Muranaka, Y. Zenitani, and J. Akimitsu, "Superconductivity at 39 K in magnesium diboride," *Nature*, vol. 410, pp. 63–64, Mar. 2001.
- [22] T. E. Weller, M. Ellerby, S. S. Saxena, R. P. Smith, and N. T. Skipper, "Superconductivity in the intercalated graphite compounds C_6Yb and C_6Ca ," *Nat. Phys.*, vol. 1, pp. 39–41, Oct. 2005.
- [23] G. Lamura, M. Aurino, G. Cifariello, E. Di Gennaro, A. Andreone, N. Emery, C. Hérold, J.-F. Marêché, and P. Lagrange, "Experimental Evidence of s-Wave Superconductivity in Bulk CaC_6 ," *Phys. Rev. Lett.*, vol. 96, p. 107008, Mar. 2006.
- [24] E. A. Ekimov, V. A. Sidorov, E. D. Bauer, N. N. Mel'nik, N. J. Curro, J. D. Thompson, and S. M. Stishov, "Superconductivity in diamond," *Nature*, vol. 428, pp. 542–545, Apr. 2004.
- [25] O. Gunnarsson, "Superconductivity in fullerenes," *Rev. Mod. Phys.*, vol. 69, pp. 575–606, Apr. 1997.
- [26] J. S. Kim, R. K. Kremer, L. Boeri, and F. S. Razavi, "Specific Heat of the Ca-Intercalated Graphite Superconductor CaC_6 ," *Phys. Rev. Lett.*, vol. 96, p. 217002, June 2006.
- [27] D. G. Hinks, D. Rosenmann, H. Claus, M. S. Bailey, and J. D. Jorgensen, "Large Ca isotope effect in the CaC_6 superconductor," *Phys. Rev. B*, vol. 75, p. 014509, Jan. 2007.
- [28] T. Valla, J. Camacho, Z.-H. Pan, A. V. Fedorov, A. C. Walters, C. A. Howard, and M. Ellerby, "Anisotropic Electron-Phonon Coupling and Dynamical Nesting on the Graphene Sheets in Superconducting CaC_6 using Angle-Resolved Photoemission Spectroscopy," *Phys. Rev. Lett.*, vol. 102, p. 107007, Mar. 2009.
- [29] H. J. Choi, D. Roundy, H. Sun, M. L. Cohen, and S. G. Louie, "The origin of the anomalous superconducting properties of MgB_2 ," *Nature*, vol. 418, pp. 758–760, Aug. 2002.
- [30] G. Profeta, M. Calandra, and F. Mauri, "Phonon-mediated superconductivity in graphene by lithium deposition," *Nat. Phys.*, vol. 8, pp. 131–134, Feb. 2012.
- [31] G. Csányi, P. B. Littlewood, A. H. Nevidomskyy, C. J. Pickard, and B. D. Simons, "The role of the interlayer state in the electronic structure of

- superconducting graphite intercalated compounds,” *Nat. Phys.*, vol. 1, pp. 42–45, Oct. 2005.
- [32] A. V. Fedorov, N. I. Verbitskiy, D. Haberer, C. Struzzi, L. Petaccia, D. Usachov, O. Y. Vilkov, D. V. Vyalikh, J. Fink, M. Knupfer, B. Büchner, and A. Grüneis, “Observation of a universal donor-dependent vibrational mode in graphene,” *Nat Commun*, vol. 5, Feb. 2014.
- [33] A. M. Black-Schaffer and S. Doniach, “Resonating valence bonds and mean-field d-wave superconductivity in graphite,” *Phys. Rev. B*, vol. 75, p. 134512, Apr. 2007.
- [34] R. R. da Silva, J. H. S. Torres, and Y. Kopelevich, “Indication of Superconductivity at 35 K in Graphite-Sulfur Composites,” *Phys. Rev. Lett.*, vol. 87, p. 147001, Sept. 2001.
- [35] S. Moehlecke, Y. Kopelevich, and M. B. Maple, “Interaction between superconducting and ferromagnetic order parameters in graphite-sulfur composites,” *Phys. Rev. B*, vol. 69, p. 134519, Apr. 2004.
- [36] A. Ballestar, J. Barzola-Quiquia, T. Scheike, and P. Esquinazi, “Josephson-coupled superconducting regions embedded at the interfaces of highly oriented pyrolytic graphite,” *New J. Phys.*, vol. 15, p. 023024, Feb. 2013.
- [37] B. Uchoa and A. H. Castro Neto, “Superconducting States of Pure and Doped Graphene,” *Phys. Rev. Lett.*, vol. 98, p. 146801, Apr. 2007.
- [38] N. B. Kopnin and E. B. Sonin, “BCS Superconductivity of Dirac Electrons in Graphene Layers,” *Phys. Rev. Lett.*, vol. 100, p. 246808, June 2008.
- [39] C. Honerkamp, “Density Waves and Cooper Pairing on the Honeycomb Lattice,” *Phys. Rev. Lett.*, vol. 100, p. 146404, Apr. 2008.
- [40] R. Nandkishore, R. Thomale, and A. V. Chubukov, “Superconductivity from weak repulsion in hexagonal lattice systems,” *Phys. Rev. B*, vol. 89, p. 144501, Apr. 2014.
- [41] J. González, “Kohn-Luttinger superconductivity in graphene,” *Phys. Rev. B*, vol. 78, p. 205431, Nov. 2008.
- [42] S. Pathak, V. B. Shenoy, and G. Baskaran, “Possible high-temperature superconducting state with a d+id pairing symmetry in doped graphene,” *Phys. Rev. B*, vol. 81, p. 085431, Feb. 2010.

- [43] R. Nandkishore, L. S. Levitov, and A. V. Chubukov, “Chiral superconductivity from repulsive interactions in doped graphene,” *Nat. Phys.*, vol. 8, pp. 158–163, Feb. 2012.
- [44] W.-S. Wang, Y.-Y. Xiang, Q.-H. Wang, F. Wang, F. Yang, and D.-H. Lee, “Functional renormalization group and variational Monte Carlo studies of the electronic instabilities in graphene near 1/4 doping,” *Phys. Rev. B*, vol. 85, p. 035414, Jan. 2012.
- [45] W. Wu, M. M. Scherer, C. Honerkamp, and K. Le Hur, “Correlated Dirac particles and superconductivity on the honeycomb lattice,” *Phys. Rev. B*, vol. 87, p. 094521, Mar. 2013.
- [46] A. M. Black-Schaffer and C. Honerkamp, “Chiral d -wave superconductivity in doped graphene,” *ArXiv14060101 Cond-Mat*, May 2014. arXiv: 1406.0101.
- [47] A. M. Black-Schaffer, “Edge Properties and Majorana Fermions in the Proposed Chiral d -Wave Superconducting State of Doped Graphene,” *Phys. Rev. Lett.*, vol. 109, p. 197001, Nov. 2012.
- [48] P. Esquinazi, “Invited review: Graphite and its hidden superconductivity,” *Pap. Phys.*, vol. 5, Dec. 2013.
- [49] P. Esquinazi, N. García, J. Barzola-Quiquia, P. Rödiger, K. Schindler, J.-L. Yao, and M. Ziese, “Indications for intrinsic superconductivity in highly oriented pyrolytic graphite,” *Phys. Rev. B*, vol. 78, p. 134516, Oct. 2008.
- [50] S. Dusari, J. Barzola-Quiquia, and P. Esquinazi, “Superconducting Behavior of Interfaces in Graphite: Transport Measurements of Microconstrictions,” *J Supercond Nov Magn*, vol. 24, pp. 401–405, Jan. 2011.
- [51] T. Scheike, P. Esquinazi, A. Setzer, and W. Böhlmann, “Granular superconductivity at room temperature in bulk highly oriented pyrolytic graphite samples,” *Carbon*, vol. 59, pp. 140–149, Aug. 2013.
- [52] T. Scheike, W. Böhlmann, P. Esquinazi, J. Barzola-Quiquia, A. Ballestar, and A. Setzer, “Can Doping Graphite Trigger Room Temperature Superconductivity? Evidence for Granular High-Temperature Superconductivity in Water-Treated Graphite Powder,” *Adv. Mater.*, vol. 24, pp. 5826–5831, Nov. 2012.

- [53] A. Ballestar, P. Esquinazi, J. Barzola-Quiquia, S. Dusari, F. Bern, R. R. da Silva, and Y. Kopelevich, "Possible superconductivity in multi-layer-graphene by application of a gate voltage," *Carbon*, vol. 72, pp. 312–320, June 2014.
- [54] Y. Kopelevich, P. Esquinazi, J. H. S. Torres, and S. Moehlecke, "Ferromagnetic- and Superconducting-Like Behavior of Graphite," *J. Low Temp. Phys.*, vol. 119, no. 5, pp. 691–702, 2000.
- [55] Y. Kopelevich, P. Esquinazi, J. H. S. Torres, R. R. d. Silva, and H. Kempa, "Graphite as a Highly Correlated Electron Liquid," in *Advances in Solid State Physics* (B. Kramer, ed.), no. 43 in *Advances in Solid State Physics*, pp. 207–222, Springer Berlin Heidelberg, Jan. 2003.
- [56] A. Y. Kasumov, R. Deblock, M. Kociak, B. Reulet, H. Bouchiat, I. I. Khodosh, Y. B. Gorbatov, V. T. Volkov, C. Journet, and M. Burghard, "Supercurrents Through Single-Walled Carbon Nanotubes," *Science*, vol. 284, pp. 1508–1511, May 1999. PMID: 10348734.
- [57] A. Andreev, "The Thermal Conductivity of the Intermediate State in Superconductors," *Sov. Phys. JETP*, vol. 19, no. 5, pp. 1228–1231, 1964.
- [58] H. B. Heersche, P. Jarillo-Herrero, J. B. Oostinga, L. M. K. Vandersypen, and A. F. Morpurgo, "Bipolar supercurrent in graphene," *Nature*, vol. 446, pp. 56–59, Mar. 2007.
- [59] M. Titov and C. W. J. Beenakker, "Josephson effect in ballistic graphene," *Phys Rev B*, vol. 74, p. 041401, July 2006.
- [60] C. W. J. Beenakker, "Specular Andreev Reflection in Graphene," *Phys. Rev. Lett.*, vol. 97, no. 6, p. 067007, 2006.
- [61] C. W. J. Beenakker, "Colloquium: Andreev reflection and Klein tunneling in graphene," *Rev. Mod. Phys.*, vol. 80, pp. 1337–1354, Oct. 2008.
- [62] F. Miao, S. Wijeratne, Y. Zhang, U. C. Coskun, W. Bao, and C. N. Lau, "Phase-Coherent Transport in Graphene Quantum Billiards," *Science*, vol. 317, pp. 1530–1533, Sept. 2007. PMID: 17872440.
- [63] X. Du, I. Skachko, and E. Y. Andrei, "Josephson current and multiple Andreev reflections in graphene SNS junctions," *Phys. Rev. B*, vol. 77, p. 184507, May 2008.

- [64] C. Ojeda-Aristizabal, M. Ferrier, S. Guéron, and H. Bouchiat, “Tuning the proximity effect in a superconductor-graphene-superconductor junction,” *Phys. Rev. B*, vol. 79, p. 165436, Apr. 2009.
- [65] D. Jeong, J.-H. Choi, G.-H. Lee, S. Jo, Y.-J. Doh, and H.-J. Lee, “Observation of supercurrent in PbIn-graphene-PbIn Josephson junction,” *Phys. Rev. B*, vol. 83, p. 094503, Mar. 2011.
- [66] I. V. Borzenets, U. C. Coskun, S. J. Jones, and G. Finkelstein, “Phase Diffusion in Graphene-Based Josephson Junctions,” *Phys. Rev. Lett.*, vol. 107, p. 137005, Sept. 2011.
- [67] K. Komatsu, C. Li, S. Autier-Laurent, H. Bouchiat, and S. Guéron, “Superconducting proximity effect in long superconductor/graphene/superconductor junctions: From specular Andreev reflection at zero field to the quantum Hall regime,” *Phys. Rev. B*, vol. 86, p. 115412, Sept. 2012.
- [68] N. Mizuno, B. Nielsen, and X. Du, “Ballistic-like supercurrent in suspended graphene Josephson weak links,” *Nat. Commun.*, vol. 4, Nov. 2013.
- [69] J.-H. Choi, G.-H. Lee, S. Park, D. Jeong, J.-O. Lee, H.-S. Sim, Y.-J. Doh, and H.-J. Lee, “Complete gate control of supercurrent in graphene p–n junctions,” *Nat. Commun.*, vol. 4, Sept. 2013.
- [70] F. Deon, S. Šopić, and A. F. Morpurgo, “Tuning the Influence of Microscopic Decoherence on the Superconducting Proximity Effect in a Graphene Andreev Interferometer,” *Phys. Rev. Lett.*, vol. 112, p. 126803, Mar. 2014.
- [71] N. Walet, *Advanced Quantum Mechanics II*. Manchester University, 2012.
- [72] R. Saito, G. Dresselhaus, and M. S. Dresselhaus, *Physical Properties of Carbon Nanotubes*. Imperial College Press, Jan. 1998.
- [73] J. W. McClure, “Diamagnetism of Graphite,” *Phys. Rev.*, vol. 104, pp. 666–671, Nov. 1956.
- [74] N. B. Brandt, S. M. Chudinov, and Y. G. Ponomarev, *Semimetals: 1. Graphite and its Compounds*. Elsevier, Dec. 2012.
- [75] M. S. Dresselhaus and G. Dresselhaus, “Intercalation compounds of graphite,” *Adv. Phys.*, vol. 51, pp. 1–186, Jan. 2002.

- [76] J. L. Mañes, F. Guinea, and M. A. H. Vozmediano, “Existence and topological stability of Fermi points in multilayered graphene,” *Phys. Rev. B*, vol. 75, p. 155424, Apr. 2007.
- [77] E. McCann and V. I. Fal’ko, “Landau-Level Degeneracy and Quantum Hall Effect in a Graphite Bilayer,” *Phys. Rev. Lett.*, vol. 96, p. 086805, Mar. 2006.
- [78] E. McCann, D. S. L. Abergel, and V. I. Fal’ko, “Electrons in bilayer graphene,” *Solid State Communications*, vol. 143, pp. 110–115, July 2007.
- [79] G. M. Rutter, S. Jung, N. N. Klimov, D. B. Newell, N. B. Zhitenev, and J. A. Stroscio, “Microscopic polarization in bilayer graphene,” *Nat. Phys.*, vol. 7, pp. 649–655, Aug. 2011.
- [80] E. McCann, “Asymmetry gap in the electronic band structure of bilayer graphene,” *Phys. Rev. B*, vol. 74, p. 161403, Oct. 2006.
- [81] E. V. Castro, K. S. Novoselov, S. V. Morozov, N. M. R. Peres, J. M. B. L. dos Santos, J. Nilsson, F. Guinea, A. K. Geim, and A. H. C. Neto, “Biased Bilayer Graphene: Semiconductor with a Gap Tunable by the Electric Field Effect,” *Phys. Rev. Lett.*, vol. 99, p. 216802, Nov. 2007.
- [82] E. V. Castro, K. S. Novoselov, S. V. Morozov, N. M. R. Peres, J. M. B. L. d. Santos, J. Nilsson, F. Guinea, A. K. Geim, and A. H. C. Neto, “Electronic properties of a biased graphene bilayer,” *J. Phys.: Condens. Matter*, vol. 22, p. 175503, May 2010.
- [83] B. Partoens and F. M. Peeters, “From graphene to graphite: Electronic structure around the K point,” *Phys. Rev. B*, vol. 74, p. 075404, Aug. 2006.
- [84] H. Gasparoux, “Modification des propriétés magnétiques du graphite par création de sequences rhomboédriques,” *Carbon*, vol. 5, pp. 441–451, Nov. 1967.
- [85] E. Rollings, G. H. Gweon, S. Y. Zhou, B. S. Mun, J. L. McChesney, B. S. Hussain, A. V. Fedorov, P. N. First, W. A. de Heer, and A. Lanzara, “Synthesis and characterization of atomically thin graphite films on a silicon carbide substrate,” *Journal of Physics and Chemistry of Solids*, vol. 67, pp. 2172–2177, Sept. 2006.
- [86] M. Koshino and E. McCann, “Parity and valley degeneracy in multilayer graphene,” *Phys. Rev. B*, vol. 81, p. 115315, Mar. 2010.

-
- [87] I. A. Luk'yanchuk and Y. Kopelevich, "Phase Analysis of Quantum Oscillations in Graphite," *Phys. Rev. Lett.*, vol. 93, p. 166402, Oct. 2004.
- [88] S. Y. Zhou, G.-H. Gweon, J. Graf, A. V. Fedorov, C. D. Spataru, R. D. Diehl, Y. Kopelevich, D.-H. Lee, S. G. Louie, and A. Lanzara, "First direct observation of Dirac fermions in graphite," *Nat. Phys.*, vol. 2, pp. 595–599, Sept. 2006.
- [89] F. Guinea, A. H. Castro Neto, and N. M. R. Peres, "Electronic states and Landau levels in graphene stacks," *Phys. Rev. B*, vol. 73, p. 245426, June 2006.
- [90] H. K. Onnes, "Further experiments with liquid helium," *Leiden Comm.*, vol. 120b, 112b, 124c, Apr. 1911.
- [91] J. Bardeen, L. N. Cooper, and J. R. Schrieffer, "Theory of Superconductivity," *Phys. Rev.*, vol. 108, pp. 1175–1204, Dec. 1957.
- [92] L. N. Cooper, "Bound Electron Pairs in a Degenerate Fermi Gas," *Phys. Rev.*, vol. 104, pp. 1189–1190, Nov. 1956.
- [93] A. B. Pippard, "An Experimental and Theoretical Study of the Relation between Magnetic Field and Current in a Superconductor," *Proc. R. Soc. Lond. A*, vol. 216, pp. 547–568, Feb. 1953.
- [94] H. Fröhlich, "Theory of the Superconducting State. I. The Ground State at the Absolute Zero of Temperature," *Phys. Rev.*, vol. 79, pp. 845–856, Sept. 1950.
- [95] E. Maxwell, "Isotope Effect in the Superconductivity of Mercury," *Phys. Rev.*, vol. 78, pp. 477–477, May 1950.
- [96] P. Coleman, *Introduction to Many Body Physics*. Cambridge: Cambridge University Press, May 2012.
- [97] Y. Nambu, "Quasi-Particles and Gauge Invariance in the Theory of Superconductivity," *Phys. Rev.*, vol. 117, pp. 648–663, Feb. 1960.
- [98] N. N. Bogoljubov, "On a new method in the theory of superconductivity," *Nuovo Cim*, vol. 7, pp. 794–805, Mar. 1958.
- [99] J. G. Valatin, "Comments on the theory of superconductivity," *Nuovo Cim*, vol. 7, pp. 843–857, Mar. 1958.

-
- [100] M. Tinkham, *Introduction to Superconductivity*. Mineola, N.Y.: Dover Publications, Second edition ed., June 2004.
- [101] C. Lanczos, *An iteration method for the solution of the eigenvalue problem of linear differential and integral operators*. National Bureau of Standards, 1950.
- [102] G. Litak, P. Miller, and B. L. Györfy, “A recursion method for solving the Bogoliubov equations for inhomogeneous superconductors,” *Physica C: Superconductivity*, vol. 251, pp. 263–273, Sept. 1995.
- [103] A. M. Martin and J. F. Annett, “Self-consistent interface properties of d- and s-wave superconductors,” *Phys. Rev. B*, vol. 57, pp. 8709–8716, Apr. 1998.
- [104] A. Weiße, G. Wellein, A. Alvermann, and H. Fehske, “The kernel polynomial method,” *Rev Mod Phys*, vol. 78, pp. 275–306, Mar. 2006.
- [105] H. Fehske, R. Schneider, and A. Weiße, *Computational Many-Particle Physics*. Springer Science & Business Media, Jan. 2008.
- [106] R. Silver and H. Roder, “Densities of states of mega-dimensional Hamiltonian matrices,” *Int. J. Mod. Phys. C*, vol. 05, pp. 735–753, Aug. 1994.
- [107] L.-W. Wang and A. Zunger, “Solving Schrödinger’s equation around a desired energy: Application to silicon quantum dots,” *J. Chem. Phys.*, vol. 100, pp. 2394–2397, Feb. 1994.
- [108] L.-W. Wang, “Calculating the density of states and optical-absorption spectra of large quantum systems by the plane-wave moments method,” *Phys. Rev. B*, vol. 49, pp. 10154–10158, Apr. 1994.
- [109] A. Weisse, “Chebyshev expansion approach to the AC conductivity of the Anderson model,” *Eur. Phys. J. B*, vol. 40, pp. 125–128, Aug. 2004.
- [110] H. Röder, R. N. Silver, D. A. Drabold, and J. J. Dong, “Kernel polynomial method for a nonorthogonal electronic-structure calculation of amorphous diamond,” *Phys. Rev. B*, vol. 55, pp. 15382–15385, June 1997.
- [111] L. Covaci, F. M. Peeters, and M. Berciu, “Efficient Numerical Approach to Inhomogeneous Superconductivity: The Chebyshev-Bogoliubov–de Gennes Method,” *Phys. Rev. Lett.*, vol. 105, p. 167006, Oct. 2010.
- [112] L. P. Gor’kov, “Theory of superconducting alloys in a strong magnetic field near the critical temperature,” *Sov. Phys. JETP*, vol. 10, p. 998, 1960.

- [113] V. A. Mandelshtam and H. S. Taylor, "Spectral projection approach to the quantum scattering calculations," *J. Chem. Phys.*, vol. 102, pp. 7390–7399, May 1995.
- [114] V. A. Mandelshtam and H. S. Taylor, "A simple recursion polynomial expansion of the Green's function with absorbing boundary conditions. Application to the reactive scattering," *J. Chem. Phys.*, vol. 103, pp. 2903–2907, Aug. 1995.
- [115] D. E. Manolopoulos, "Derivation and reflection properties of a transmission-free absorbing potential," *J. Chem. Phys.*, vol. 117, pp. 9552–9559, Dec. 2002.
- [116] T. Gonzalez-Lezana, E. J. Rackham, and D. E. Manolopoulos, "Quantum reactive scattering with a transmission-free absorbing potential," *J. Chem. Phys.*, vol. 120, pp. 2247–2254, Feb. 2004.
- [117] J. A. Driscoll and K. Varga, "Calculation of self-energy matrices using complex absorbing potentials in electron transport calculations," *Phys. Rev. B*, vol. 78, p. 245118, Dec. 2008.
- [118] D. Neuhasuer and M. Baer, "The time-dependent Schrödinger equation: Application of absorbing boundary conditions," *J. Chem. Phys.*, vol. 90, pp. 4351–4355, Apr. 1989.
- [119] R. Kosloff and D. Kosloff, "Absorbing boundaries for wave propagation problems," *Journal of Computational Physics*, vol. 63, pp. 363–376, Apr. 1986.
- [120] N. Bell and M. Garland, "Implementing Sparse Matrix-vector Multiplication on Throughput-oriented Processors," in *Proceedings of the Conference on High Performance Computing Networking, Storage and Analysis, SC '09*, (New York, NY, USA), pp. 18:1–18:11, ACM, 2009.
- [121] A. M. Black-Schaffer and S. Doniach, "Self-consistent solution for proximity effect and Josephson current in ballistic graphene SNS Josephson junctions," *Phys Rev B*, vol. 78, p. 024504, July 2008.
- [122] A. Kanda, T. Sato, H. Goto, H. Tomori, S. Takana, Y. Ootuka, and K. Tsukagoshi, "Dependence of proximity-induced supercurrent on junction length in multilayer-graphene Josephson junctions," *Phys. C*, vol. 470, pp. 1477–1480, Nov. 2010.

-
- [123] H. Tomori, A. Kanda, H. Goto, S. Takana, Y. Ootuka, and K. Tsukagoshi, “Fabrication of ultrashort graphene Josephson junctions,” *Phys. C*, vol. 470, pp. 1492–1495, Nov. 2010.
- [124] I. Hagymási, A. Kormányos, and J. Cserti, “Josephson current in ballistic superconductor-graphene systems,” *Phys. Rev. B*, vol. 82, p. 134516, Oct. 2010.
- [125] M. Alidoust and J. Linder, “Tunable supercurrent at the charge neutrality point via strained graphene junctions,” *Phys Rev B*, vol. 84, p. 035407, July 2011.
- [126] K. Halterman, O. T. Valls, and M. Alidoust, “Characteristic energies, transition temperatures, and switching effects in clean $S\bar{N}\bar{S}$ graphene nanostructures,” *Phys Rev B*, vol. 84, no. 6, p. 064509, 2011.
- [127] A. M. Black-Schaffer and J. Linder, “Strongly anharmonic current-phase relation in ballistic graphene Josephson junctions,” *Phys. Rev. B*, vol. 82, p. 184522, Nov. 2010.
- [128] L. Covaci and F. M. Peeters, “Superconducting proximity effect in graphene under inhomogeneous strain,” *Phys Rev B*, vol. 84, p. 241401, Dec. 2011.
- [129] I. Snyman and C. W. J. Beenakker, “Ballistic transmission through a graphene bilayer,” *Phys Rev B*, vol. 75, p. 045322, Jan. 2007.
- [130] L. Covaci and F. Marsiglio, “Proximity effect and Josephson current in clean strong/weak/strong superconducting trilayers,” *Phys. Rev. B*, vol. 73, p. 014503, Jan. 2006.
- [131] Y. Kopelevich, R. da Silva, J. Torres, S. Moehlecke, and M. Maple, “High-temperature local superconductivity in graphite and graphite–sulfur composites,” *Physica C: Superconductivity*, vol. 408–410, pp. 77–78, Aug. 2004.
- [132] J. González, F. Guinea, and M. A. H. Vozmediano, “Electron-electron interactions in graphene sheets,” *Phys. Rev. B*, vol. 63, p. 134421, Mar. 2001.
- [133] B. Roy and I. F. Herbut, “Unconventional superconductivity on honeycomb lattice: Theory of Kekule order parameter,” *Phys. Rev. B*, vol. 82, p. 035429, July 2010.

- [134] N. B. Kopnin, T. T. Heikkilä, and G. E. Volovik, “High-temperature surface superconductivity in topological flat-band systems,” *Phys. Rev. B*, vol. 83, p. 220503, June 2011.
- [135] G. Larkins and Y. Vlasov, “Indications of superconductivity in doped highly oriented pyrolytic graphite,” *Supercond. Sci. Technol.*, vol. 24, p. 092001, Sept. 2011.
- [136] C. H. Lui, Z. Li, Z. Chen, P. V. Klimov, L. E. Brus, and T. F. Heinz, “Imaging Stacking Order in Few-Layer Graphene,” *Nano Lett.*, vol. 11, pp. 164–169, Jan. 2011.
- [137] J. Ping and M. S. Fuhrer, “Layer Number and Stacking Sequence Imaging of Few-Layer Graphene by Transmission Electron Microscopy,” *Nano Lett.*, vol. 12, pp. 4635–4641, Sept. 2012.
- [138] M. Koshino, “Interlayer screening effect in graphene multilayers with ABA and ABC stacking,” *Phys. Rev. B*, vol. 81, p. 125304, Mar. 2010.
- [139] N. B. Kopnin and T. T. Heikkilä, “Surface superconductivity in rhombohedral graphite,” *arXiv:1210.7075*, Oct. 2012.
- [140] A. Shailos, W. Nativel, A. Kasumov, C. Collet, M. Ferrier, S. Guéron, R. Deblock, and H. Bouchiat, “Proximity effect and multiple Andreev reflections in few-layer graphene,” *EPL*, vol. 79, p. 57008, Sept. 2007.
- [141] T. Sato, A. Kanda, T. Moriki, H. Goto, S. Tanaka, Y. Ootuka, H. Miyazaki, S. Odaka, K. Tsukagoshi, and Y. Aoyagi, “A different type of reentrant behavior in superconductor/thin graphite film/superconductor Josephson junctions,” *Physica C*, vol. 468, pp. 797–800, Apr. 2008.
- [142] T. Sato, T. Moriki, S. Tanaka, A. Kanda, H. Goto, H. Miyazaki, S. Odaka, Y. Ootuka, K. Tsukagoshi, and Y. Aoyagi, “Gate-controlled superconducting proximity effect in ultrathin graphite films,” *Physica E*, vol. 40, pp. 1495–1497, Mar. 2008.
- [143] M. Hayashi, H. Yoshioka, and A. Kanda, “Superconducting proximity effect in graphene nanostructures,” *J. Phys.: Conf. Ser.*, vol. 248, p. 012002, Nov. 2010.
- [144] Y. Takane, “Tunneling Density of States in Multilayer Graphene Deposited on a Superconductor,” *J. Phys. Soc. Jpn.*, vol. 79, no. 12, p. 124706, 2010.

-
- [145] M. Hayashi, H. Yoshioka, and A. Kanda, “Theoretical study of superconducting proximity effect in single and multi-layered graphene,” *Physica C: Superconductivity*, vol. 470, Supplement 1, pp. S846–S847, Dec. 2010.
- [146] M. V. Hosseini and M. Zareyan, “Unconventional superconducting states of interlayer pairing in bilayer and trilayer graphene,” *Phys. Rev. B*, vol. 86, p. 214503, Dec. 2012.
- [147] W. A. Muñoz, L. Covaci, and F. M. Peeters, “Tight-binding description of intrinsic superconducting correlations in multilayer graphene,” *Phys. Rev. B*, vol. 87, p. 134509, Apr. 2013.
- [148] W. A. Muñoz, L. Covaci, and F. M. Peeters, “Tight-binding study of bilayer graphene Josephson junctions,” *Phys. Rev. B*, vol. 86, p. 184505, Nov. 2012.
- [149] R. Nandkishore, J. Maciejko, D. A. Huse, and S. L. Sondhi, “Superconductivity of disordered Dirac fermions,” *Phys. Rev. B*, vol. 87, p. 174511, May 2013.
- [150] S.-g. Cheng, H. Zhang, and Q.-f. Sun, “Effect of electron-hole inhomogeneity on specular Andreev reflection and Andreev retroreflection in a graphene-superconductor hybrid system,” *Phys. Rev. B*, vol. 83, p. 235403, June 2011.
- [151] P. Burset, W. Herrera, and A. Levy Yeyati, “Proximity-induced interface bound states in superconductor-graphene junctions,” *Phys. Rev. B*, vol. 80, p. 041402, July 2009.
- [152] E. R. Mucciolo and C. H. Lewenkopf, “Disorder and electronic transport in graphene,” *J. Phys.: Condens. Matter*, vol. 22, p. 273201, July 2010.
- [153] N. M. R. Peres, F. Guinea, and A. H. Castro Neto, “Electronic properties of disordered two-dimensional carbon,” *Phys. Rev. B*, vol. 73, p. 125411, Mar. 2006.
- [154] A. F. Morpurgo and F. Guinea, “Intervalley Scattering, Long-Range Disorder, and Effective Time-Reversal Symmetry Breaking in Graphene,” *Phys. Rev. Lett.*, vol. 97, p. 196804, Nov. 2006.
- [155] T. Ando, “Screening Effect and Impurity Scattering in Monolayer Graphene,” *J. Phys. Soc. Jpn.*, vol. 75, p. 074716, July 2006.

-
- [156] J.-H. Chen, C. Jang, S. Adam, M. S. Fuhrer, E. D. Williams, and M. Ishigami, “Charged-impurity scattering in graphene,” *Nat. Phys.*, vol. 4, pp. 377–381, May 2008.
- [157] V. M. Pereira, F. Guinea, J. M. B. Lopes dos Santos, N. M. R. Peres, and A. H. Castro Neto, “Disorder Induced Localized States in Graphene,” *Phys. Rev. Lett.*, vol. 96, p. 036801, Jan. 2006.
- [158] V. M. Pereira, J. M. B. Lopes dos Santos, and A. H. Castro Neto, “Modeling disorder in graphene,” *Phys. Rev. B*, vol. 77, p. 115109, Mar. 2008.
- [159] C. Park, H. Yang, A. J. Mayne, G. Dujardin, S. Seo, Y. Kuk, J. Ihm, and G. Kim, “Formation of unconventional standing waves at graphene edges by valley mixing and pseudospin rotation,” *PNAS*, vol. 108, pp. 18622–18625, Nov. 2011. PMID: 22049340.
- [160] F. de Juan, A. Cortijo, and M. A. H. Vozmediano, “Charge inhomogeneities due to smooth ripples in graphene sheets,” *Phys. Rev. B*, vol. 76, p. 165409, Oct. 2007.
- [161] F. Guinea, M. I. Katsnelson, and A. K. Geim, “Energy gaps and a zero-field quantum Hall effect in graphene by strain engineering,” *Nat. Phys.*, vol. 6, pp. 30–33, Sept. 2009.
- [162] V. M. Pereira and A. H. Castro Neto, “Strain Engineering of Graphene’s Electronic Structure,” *Phys. Rev. Lett.*, vol. 103, p. 046801, July 2009.
- [163] F. Guinea, A. K. Geim, M. I. Katsnelson, and K. S. Novoselov, “Generating quantizing pseudomagnetic fields by bending graphene ribbons,” *Phys. Rev. B*, vol. 81, p. 035408, Jan. 2010.
- [164] D. Moldovan, M. Ramezani Masir, and F. M. Peeters, “Electronic states in a graphene flake strained by a Gaussian bump,” *Phys. Rev. B*, vol. 88, p. 035446, July 2013.
- [165] A. R. Akhmerov and C. W. J. Beenakker, “Pseudodiffusive conduction at the Dirac point of a normal-superconductor junction in graphene,” *Phys. Rev. B*, vol. 75, p. 045426, Jan. 2007.
- [166] T. Iitaka and T. Ebisuzaki, “Random phase vector for calculating the trace of a large matrix,” *Phys. Rev. E*, vol. 69, p. 057701, May 2004.
- [167] A. Cresti, F. Ortmann, T. Louvet, D. Van Tuan, and S. Roche, “Broken Symmetries, Zero-Energy Modes, and Quantum Transport in Disordered

- Graphene: From Supermetallic to Insulating Regimes,” *Phys. Rev. Lett.*, vol. 110, p. 196601, May 2013.
- [168] G. M. M. Wakker, R. P. Tiwari, and M. Blaauboer, “Localization and circulating currents in curved graphene devices,” *Phys. Rev. B*, vol. 84, p. 195427, Nov. 2011.
- [169] N. N. Klimov, S. Jung, S. Zhu, T. Li, C. A. Wright, S. D. Solares, D. B. Newell, N. B. Zhitenev, and J. A. Stroscio, “Electromechanical Properties of Graphene Drumheads,” *Science*, vol. 336, pp. 1557–1561, June 2012. PMID: 22723417.
- [170] M. Neek-Amal, L. Covaci, and F. M. Peeters, “Nanoengineered nonuniform strain in graphene using nanopillars,” *Phys. Rev. B*, vol. 86, p. 041405, July 2012.
- [171] A. Rycerz, J. Tworzydło, and C. W. J. Beenakker, “Anomalously large conductance fluctuations in weakly disordered graphene,” *EPL*, vol. 79, p. 57003, Sept. 2007.
- [172] C. H. Lewenkopf, E. R. Mucciolo, and A. H. Castro Neto, “Numerical studies of conductivity and Fano factor in disordered graphene,” *Phys. Rev. B*, vol. 77, p. 081410, Feb. 2008.
- [173] M. I. Katsnelson, K. S. Novoselov, and A. K. Geim, “Chiral tunnelling and the Klein paradox in graphene,” *Nat. Phys.*, vol. 2, pp. 620–625, Sept. 2006.
- [174] E. Suárez Morell, J. D. Correa, P. Vargas, M. Pacheco, and Z. Barticevic, “Flat bands in slightly twisted bilayer graphene: Tight-binding calculations,” *Phys. Rev. B*, vol. 82, p. 121407, Sept. 2010.

Curriculum Vitae

William Armando Muñoz

Born on September 30, 1985 in Santiago de Cali (Colombia)

Contact

Condensed Matter Theory Group
Department of Physics
Universiteit Antwerpen
Groenenborgerlaan 171 / U209
BE-2020 Antwerpen
email 1: wallaz85@gmail.com
email 2: WilliamArmando.Munoz@uantwerpen.be



Education

2010 - 2014: Ph.D. in Physics, Universiteit Antwerpen, Belgium.
2008 - 2010: M.Sc. in Physics, Universidade Estadual de Campinas, Brazil.
2002 - 2008: B.Sc. in Physics, Universidad del Valle, Colombia.

Languages

	Listening	Speaking	Reading	Writing
English	good	fair	good	fair
Portuguese	good	good	good	fair
Spanish	Native	Native	Native	Native

List of publications

- W. A. Muñoz, L. Covaci and F. M. Peeters *Disordered graphene Josephson junctions*, submitted to Phys. Rev. B (2014).
- W. A. Muñoz, L. Covaci and F. M. Peeters *Superconducting current and proximity effect in ABA and ABC multilayer graphene Josephson junctions*, Phys. Rev. B **88**, 214502 (2013).
- W. A. Muñoz, L. Covaci and F. M. Peeters, *Tight-binding description of intrinsic superconducting correlations in multilayer graphene*, Phys. Rev. B **87**, 134509 (2013).
- W. A. Muñoz, L. Covaci and F. M. Peeters, *Tight-binding study of bilayer graphene Josephson junctions*, Phys. Rev. B **86**, 184505 (2012).

Main participations in events

- “*Disordered graphene Josephson junction*”. (Poster presentation)
W. A. Muñoz, L. Covaci and F. M. Peeters
General Scientific Meeting of the Belgian Physical Society. 28 May 2014, Leuven, Belgium.
- “*Intrinsic superconducting correlations and proximity effect in multilayer graphene*”. (Poster presentation)
W. A. Muñoz, L. Covaci and F. M. Peeters
Graphene Brazil. 22-25 September 2013, Búzios, RJ, Brazil.
- “*Proximity effect and Josephson current in double-layer SNS graphene Josephson junction*”. (Poster presentation)
W. A. Muñoz, L. Covaci and F. M. Peeters
Graphene Week. 4-8 June 2012, Delft, Netherlands.
- Capri Spring School on Transport in Nanostructures: “Superconducting hybrid nanostructures”. 15-22 April 2012, Capri, Italy.
- “*Theoretical study of bilayer graphene Josephson junctions*”. (Poster presentation)
W. A. Muñoz, L. Covaci and F. M. Peeters
Workshop on Quantum Phenomena in Graphene, Other Low-dimensional Materials, and Optical Lattices. 26 July - 7 August, Erice, Italy.

- “*Broken symmetry states in biased bilayer graphene in a quantum Hall regime*”. (Poster presentation)
W. A. Muñoz, A .L . C. Pereira and Peter A. Schulz
30th ICPS, International Conference on the Physics of Semiconductors.
July 2010, COEX, Seoul, South Korea.